이학박사 학위논문

Controlling functional properties of ferroelectric thin film by interface engineering

계면 공학에 의한 강유전체 박막의 기능 제어

2017 년 8 월

서울대학교 대학원

물리천문학부

신 영 재

Controlling functional properties of ferroelectric thin film by interface engineering

Yeong Jae Shin

Supervised by

Professor Tae Won Noh

A Dissertation submitted to the Faculty of Seoul National University in Partial Fulfillment of the Requirements for the Degree of Doctor of Philosophy

August 2017

Department of Physics and Astronomy

Graduate School

Seoul National University

Abstract

Ferroelectric (FE) materials are defined as the materials that possess a spontaneous polarization, which can be switched by an external electric field. Due to the switchable spontaneous polarization, FE materials have attracted significant interests for potential applications in multifunctional electronic devices. The examples include nonvolatile FE random access memories, FE field-effect transistors, and FE tunnel junctions. In addition, the structural distortion and generation of electric field are accompanied by FE polarization switching. This enable the electric control of various physical properties, such as magnetism and superconductivity, which can be used for next-generation multi-functional devices. For such reasons, flurry of research on FEs has been performed in condensed matter physics as well as in material sciences.

With recent trends on miniaturizing oxide-based devices, understandings of interface effects on FE properties become important. When the thickness of FE layer is reduced down to few unit cells (u.c.), the interfacial effects, which are negligible in thick films or in bulk form, significantly affect the various functional properties of FE heterostructures. For examples, the type and strength of chemical bonding at metal/FE interface was reported to be important in determining amount and stability of FE polarization of $BaTiO_3$ and $PbTiO_3$ thin films. The large electrostatic energy caused by polar discontinuity at insulator/FE interface causes unusual vortex- or flux-type FE domain configuration. In addition, interface structure, such as topography and atomic stacking sequence, also can affect the

FE polarization switching properties of ultrathin FE layer. In the thesis, the novel experimental results on the effects of interfacial structures on functional properties in epitaxial FE thin films are presented.

The polarization-electric field hysteresis (P – E hysteresis) loops is one of the remarkable features of FE capacitor devices. In epitaxial film, the P – E hysteresis loops shows the considerable dependence on frequency (f) of external *ac* field, which is caused by the microscopic FE domain wall motions. Under the external electric field, FE domain wall motion can be regarded as the growth of elastic objects in disordered medium, which exhibit strong nonlinear velocity (v) – E behavior. We were able to show that, by choosing proper electrode, we can significantly reduce the amount of disorder states at the ferroelectric $BiFeO_3$ (BFO) interface. As a result, we can realize f-independent P – E hysteresis loops in high quality epitaxial BFO thin film.

We also report the effect of background oxygen pressure (P_{O2}) on interface atomic structure of $SrRuO_3$/$BaTiO_3$/$SrRuO_3$ (SRO/BTO/SRO) heterostructure made by pulsed laser deposition (PLD). For realizing ultrathin FE device with few nanometer thick thicknesses, atomic-scale control of interface/surface structure and realization of flat surface with uniform termination are highly required. However, a lack of understandings on the surface formation mechanism in PLD has limited a deliberate control of surface/interface atomic stacking sequences. Here, we report that selective control of SrO-TiO_2 or BaO-RuO_2 termination sequence at top SRO/BTO interface via changing P_{O2}. We found that, under high P_{O2} (150 mTorr), heterogeneous interface termination with both SrO-TiO_2 and BaO-RuO_2 was formed. On the other hand, a uniform SrO-TiO_2 termination

sequence at the SRO/BTO interface can be achieved by lowering the P_{O2} to 5 mTorr, regardless of the total background gas pressure, growth mode, or growth rate. Our results indicate that the thermodynamic stability of the BTO surface at the low-energy kinetics stage of PLD can play an important role in surface/interface termination formation.

The SRO/BTO/SRO capacitor with heterogeneous interface termination sequences and uniform SrO-TiO_2 termination sequence shows the distinct FE properties. By using piezoelectric force microscopy (PFM), we investigated local FE polarization properties. In ultrathin limit of BTO layer, SRO/BTO/SRO heterostructure with heterogeneous interface termination sequence exhibits the significant local variation of FE polarization switching. In particular, more than half of measured area exhibits the pinned FE polarization state, caused by existence of BaO-RuO_2 interface termination sequence. On the other hand, SRO/BTO/SRO capacitor with symmetric and uniform interfacial termination, whole measured region exhibit the clear FE polarization switching even with the 3.5 unit cells (~1.2 nm) of BTO thickness.

We believe that our intensive researches in this thesis make important steps forward comprehensive understanding on deterministic role of interface structure in determining FE properties of ultrathin film.

Keywords: ferroelectric thin film, interface engineering, oxide heterostructure, pulsed laser deposition

Student number: 2011-20407

Contents

List of Figures

BFO/LSMO and (e) BFO/SRO. (f) Plot of minimum nucleation field (E_N) as a function of f. The dashed lines denote the average E_N values for each film.

Figure 3.6. The same data as Figure 3.5c, with KAI model fitting results using $n = 2$. In contrast to the results with $n = 1$ in Figure 3.5c, the fitting results do not accurately describe the data. This indicates that the domain wall motion in the BFO films is closer to 1D-like motion than typical 2D motion.

Figure 3.7. Surface morphology and schematics of the energy landscape in BFO thin films. AFM topography images of (a) BFO/LSMO and (b) BFO/SRO films. Line profiles of (c) BFO/LSMO and (d) BFO/SRO surfaces, taken along the dashed lines in (a) and (b). Clear step-bunching is observed for both BFO films. Schematic diagram of pinning energy landscape ((*x*)) in (e) BFO/LSMO and (f) BFO/SRO films. The red circles denote *positions* at which nucleation occurs. The arrows represent domain wall motion, depending on applied field E and the pinning energy barrier.

Figure 3.8. Temperature (*T*)-dependent hysteretic dynamics. log-log E_C-f plot for (a) BFO/LSMO and (b) BFO/SRO film at various temperatures. (c) Plot of β values with respect to f. The β values of BFO/LSMO at low f (20-200 Hz) and high f (500-2000 Hz) are represented by red circles and red squares respectively. The left-side of the (red) dashed line indicates the low-temperature creep-free regime of BFO/LSMO. The β values for BFO/SRO are represented as black triangles. (d) Phase diagram of hysteretic domain wall dynamics under *ac*-driven field. The solid red lines E_N and blue E_{cr} show the dynamic crossover between no nuclei, creep, and viscous flow regimes. The regimes where creep or viscous flow motion govern domain wall dynamics are shaded red and blue, respectively. The green lines $E_1(t)$ and $E_2(t)$ represent the first $1/4f$ of applied *ac* field at two different temperatures. The horizontal dashed line denotes the temperature T_P, related to the typical pinning energy E_P. Phase diagrams derived from (f) BFO/LSMO data and (e) BFO/SRO data. Red circles indicate E_N and blue solid squares and open squares

SRO/BTO/SRO heterostructure with a BTO layer grown at P_{O2} = 150 mTorr (5 mTorr). (b) [(e)] Magnified HAADF images of the pre-scanned area marked by the dashed box in (a) [(d)]. The HAADF intensity profiles along the solid boxes marked in (b) [(e)] are also shown. (c) [(f)] Schematic illustration of the BTO surface after the growth at P_{O2} = 150 mTorr (5 mTorr). After BTO growth at P_{O2} = 150 mTorr, the film surface (i.e., SRO/BTO interface) shows a heterogeneous termination sequence. In contrast, the as-grown BTO at P_{O2} = 5 mTorr film surface shows a uniform SrO-TiO_2 termination sequence.

Figure 4.4. Interfacial structure of SRO/BTO/SRO heterostructures with BTO grown under pure oxygen atmospheres. (a) [(d)] High-angle annular dark field (HAADF) images of the SRO/BTO/SRO heterostructure with a BTO layer grown at P_{O2} = 150 mTorr (5 mTorr). (b) [(e)] Magnified HAADF images of the pre-scanned area marked by the dashed box in (a) [(d)]. The HAADF intensity profiles along the solid boxes marked in (b) [(e)] are also shown. (c) [(f)] Schematic illustration of the BTO surface after the growth at P_{O2} = 150 mTorr (5 mTorr). After BTO growth at P_{O2} = 150 mTorr, the film surface (i.e., SRO/BTO interface) shows a heterogeneous termination sequence. In contrast, the as-grown BTO at P_{O2} = 5 mTorr film surface shows a uniform SrO-TiO_2 termination sequence.

Figure 4.5. Characterization of the chemical stoichiometry of BTO films. (a) The cation Ti/Ba ratio of BTO films grown at different background atmospheres measured by energy-dispersive spectroscopy (EDS). The error bars indicate the standard deviations of Ti/Ba ratio measured from 20 locations randomly selected from one BTO sample. (b) HAADF images of the SRO/BTO/SRO heterostructure, in which the 2.5-u.c.-thick BTO layer was grown at P_{O2} = 5 mTorr. (c) Electron energy-loss spectroscopy (EELS) at Ti-L and O-K edges measured from BTO layer and STO(001) substrate. The electron spot position is marked by the open circles and solid arrows in (b).

Figure 4.6. P_{O2}-dependent surface energy differences between TiO_2-terminated and BaO-terminated BTO ($\Delta\Omega = \Omega^{TiO2} - \Omega^{BaO}$). We set $\Delta\mu_{Ba} = -5.2$ eV and $T = 1000$ K. The

dashed lines indicate the offset of $\Delta\Omega$ induced by the thermal energy at 1000 K (86 meV). The inset schematic diagram describes the possible energy landscapes of BTO surface structures (i.e., TiO_2 and BaO terminations), which evolve with P_{O2}. The arrows indicate the trend of stabilizing the specific surface structure.

Figure 4.7. (a) Schematic diagrams of the cross-section of the PZT capacitor showing the time-dependent domain switching process for the different fatigued states. The (b) predicted and (c) measured PFM (top-view) phase and amplitude images after the completion of domain switching for each states. See detailed explanations in the text. Adapted from Yang *et al*. [26].

Figure 5.1. Schematic of the possible atomic stacking of the $SrRuO_3/BaTiO_3/SrRuO_3$ (SRO/BTO/SRO) heterostructure with a) symmetric SrO-TiO_2 interfaces, which result in a BTO layer thickness (t_{BTO}) of 3.5 unit cells (u.c.), and with b) BaO-RuO_2 and SrO-TiO_2 interfaces at the top and bottom of the BTO layer, respectively, which result in t_{BTO} = 3 u.c.. Note that the asymmetric case (b) occurs under the commonly assumed *unit-cell by unit-cell* growth mode.

Figure 5.2. AFM topography images of 5 × 5 μm^2 square-shaped SRO/BTO/SRO ferroelectric capacitor with a) P_{O2} = 150 mTorr and b) P_{O2} = 5 mTorr. The black dots schematically show the locations at which the PFM hysteresis loops were measured.

Figure 5.3. The amplitude and phase from piezoresponse force microscopy (PFM) hysteresis loops collected in different locations reveal piezoresponse in both polarization directions (left) and highly pinned piezoresponse along the downward polarization direction (right). The color map at the center of 1d displays the ratio of maximum PFM amplitude response (A_{+max}/A_{-max}) at positive bias (A_{+max}) to that at negative bias (A_{-max}). The

black dots marked by (i) and (ii) indicate the points where the left and right plots were measured.

Figure 5.4. The amplitude and phase from piezoresponse force microscopy (PFM) hysteresis loops collected in different locations reveal piezoresponse in both polarization directions (left) and highly pinned piezoresponse along the downward polarization direction (right). The color map at the center of 1d displays the ratio of maximum PFM amplitude response (A_{+max}/A_{-max}) at positive bias (A_{+max}) to that at negative bias (A_{-max}). The black dots marked by (i) and (ii) indicate the points where the left and right plots were measured.

Figure 5.5. The *ac* voltage (V_{ac})-dependent change of a) the off-field hysteresis loop and b) on-field loop, which shows an abrupt loop collapse at a V_{ac} equal to the coercive voltage (e.g., ~ 4 V).

Figure 5.6. a) STEM image of a 3.5 u.c. BTO layer with P_{O2} = 5 mTorr, sandwiched by SRO electrodes. b) Spatially averaged section of 5.5a by template matching analysis (TeMA). The small red crosses indicate the peak positions of each atom. c) The closed circle indicates B-site cation displacement from the center position of the A-site cation cage ($\delta_{B\text{-cation}}$), obtained from the TeMA average peak positions of atoms for each row of 5.5a. Error bars indicate the standard deviation of different columns. d) Enlarged image of the highlighted red box in 5.5b. The yellow box indicates the Ba-cage and dashed lines indicate the cage center position. The difference between the Ti peak and the center position indicates a relative displacement of Ti in the downward direction.

List of Tables

Chapter 1
Introduction

1.1 Displacive ferroelectric materials

The electrical properties of solids can be categorized into three classes; conductors, semiconductors and nonconductors. Among the nonconductors (or insulators), materials which can exhibits the electric polarization is called dielectrics. In most case, dielectric materials is electrically natural and only exhibit electric polarization (P) under the application of electric field. However, in some dielectrics, their crystal structure change from centrosymmetric structure to non-centrosymmetric structure below critical Curie temperature (T_C). In such cases, the dielectric materials have a nonzero P even without external electric field. The nonzero P is called spontaneous polarization of the material. And among the dielectrics with spontaneous polarization, the materials which can reverse direction of spontaneous polarization by applying external electric field are called ferroelectric (FE) materials [1]. The existence of spontaneous polarization is not a sufficient condition for ferroelectrics, but is the most important characteristic.

The FE materials are often characterized as either displacive type or order-disorder type. For the displacive type FE materials, centrosymmetry of the crystal structure is broken below a critical Curie temperature (T_C) by slight atomic displacement of cations and anions

(Figure 1.1). With broken centrosymmetry, free energy profile change its shape from parabolic one to double-well shaped. The each minima of double-well shaped energy profile corresponds to the spontaneous polarization with different directions (or polarities). By applying external electric field, each *P* state can be switched to other state, giving rise to the *P* – electric field (*E*) hysteresis loops. The most commonly used ferroelectric materials, such as $PbTiO_3$ and $BaTiO_3$, are categorized as the displacive ferroelectric materials.

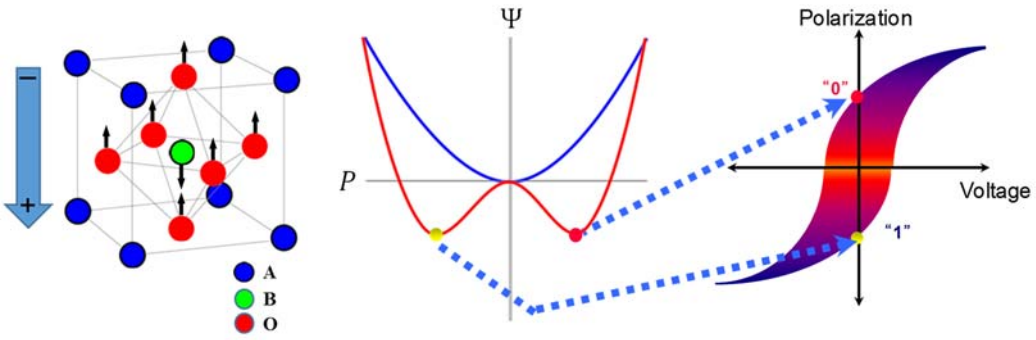

Figure 1.1. Schematic description of ferroelectric (FE) properties of perovskite ABO_3 crystals.

1.2 Surface/interface effects in ferroelectric thin film

1.2.1 Ferroelectric domain dynamics

The different polarities in FE materials usually has almost equivalent energy so that, in principle, all of polarities could have similar probability of appearing when the transition from paraelectric phase to ferroelectric phase occurs. Thus, FE materials usually consist of

small regions with different polarities. The region is called “FE domain” and boundary between two FE domains is called “FE domain wall” [2].

The switching dynamics of P driven by external E is one of the most important issues in FE materials. The P switching dynamics has been recognized one of the deterministic factor in FE-based electronic devices, such as nonvolatile FE random access memories, FE field-effect transistors, and so on [3–5]. In most FE materials, P switching occurs via nucleation and subsequent growth of microscopic FE domains (Figure 1.2). The nucleation and growth of FE domains are highly related to defect states inside FE materials and at interface.

The first step of FE domain switching process is nucleation of FE domain with opposite P. In ideal defect-free materials, nucleation of opposite P domain homogeneously occurs via thermally activated process. However, the energy barrier for the nucleation (U_N) is much higher than experimentally observed value. Under the typical coercive field (E_C) of most FE materials (~ 100 kV/cm), U_N is expected to be higher than 10^3 k_BT [6]. Thus, in actual case, the nucleation of opposite FE domains is mediated by the defects at inhomogeneous locations [7–11]. The existence of defects effectively lower the U_N so that nucleation of opposite FE domain can occur even at room temperature.

After nucleation, FE domain rapidly growth in a needle-like shape along the direction of E (forward growth). After the forward growth, the FE domains extend its volume in lateral directions (sideway growth). During the forward and sideway growth of FE domains, the quenched defects could act as pinning sites, giving rise to hindering the propagation of FE domain walls. Thus, shape and motion of propagating FE domain wall strongly depends

on the nature of the quenched defects [12].

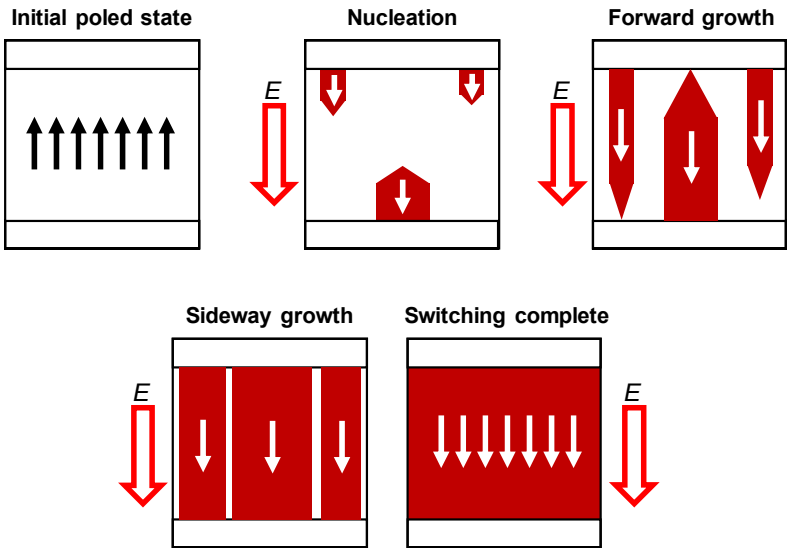

Figure 1.2. Schematic of defect-mediated FE domain switching under external *E* field. The white (red) regions with black (white) arrow indicate the FE domain that have *P* along upward (downward) direction.

Because of the strong effect on FE domain nucleation and growth, quenched defect plays an important role in FE *P* switching dynamics [10,11,13,14]. In the most FE materials (in particular in film form), there exist a broad range of defects, such as point defects (vacancies of cations and anions) and extended defects (dislocations, grain boundaries, and defect dipoles). The defects in FE materials act as a disorder for nucleation and pinning of FE domain motions. As a result, FE domain wall motion can be regarded as moving elastic objects in disordered medium, which is one of vastly used physical concepts in various systems. The nonlinear defect-mediated FE domain wall dynamics under *dc E* was

intensively investigated by Jo *et al* [15]. They clearly demonstrated dependence of domain wall velocity (v) on strength of E and temperature, which is consistent with classical concept of surface growth. In addition, FE domain wall dynamics under *ac* E was also investigated by Yang *et al* [16].

1.2.2 Depolarizing field and critical thickness of FE thin film

In case of FE thin film, the thickness of the film is important parameter for FE polarization stability. With decreasing thickness, the value of P decreases significantly and disappear below certain thickness [17–20]. The minimum thickness for FE polarization is called critical thickness of FE film. The existence of FE critical thickness mainly originate from effect of depolarizing field.

For simple explanation on FE critical thickness and depolarizing field, consider a FE capacitor with short-circuited electrodes. Suppose that the FE layer is a perfect insulator and the electrodes are common metal. The FE spontaneous polarizations (P_S) inside the FE film induce the bound charges at FE/metal interfaces. To compensate the interface bound charge, a certain amount of charge Q_e in induced at electrodes. If the electrodes in ideal perfect metal, Q_e is induced only at the interface. In such a case, interface bound charge is perfectly canceled out and no electric field is generated inside FE film. However, in real case, Q_e in electrodes present within a finite screening length λ from the interface, and do not completely cancel the bound charge. The incomplete compensation of bound charges cause an electric field E_f inside the FE film whose direction is opposite to the direction of P_S. The E_f is called depolarizing field (Figure 1.3 (a)).

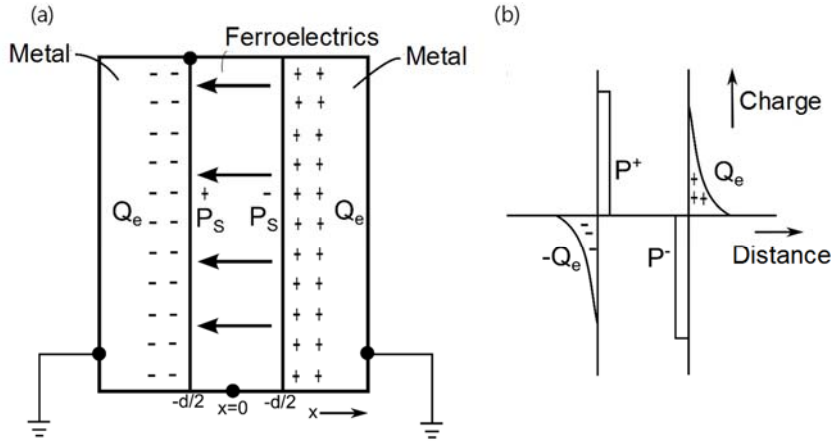

Figure 1.3. (a) Schematic of the short-circuited capacitor device with ferroelectric insulating barrier. (b) The charge distribution inside ferroelectric capacitor.

A qualitative understanding on the correlation between depolarizing field and thickness of FE film can be achieved by solving simple electrostatic problem. The FE capacitor in Figure 1.3 (a) can be considered a simple one-dimensional model capacitor if the size of electrode is much larger than the thickness of the film *d*. In order to simplify the problem, suppose the charge distribution $\rho_e(x)$ inside the electrodes follow the function,

$$\rho(x) = \frac{Q_e}{\lambda} e^{-\frac{x}{\lambda}} \tag{1.1}$$

According to the Poisson relationship, the electric displacement *D* inside the capacitor is,

$$\frac{dD}{dx} = \rho(x) \tag{1.2a}$$

$$D = \varepsilon_e E_e + P \tag{1.2b}$$

where ε_e is the dielectric permittivity of electrodes and E_e is the electric field inside the electrodes. The boundary conditions for E_e are,

$$E_e(x) \to 0, as \;\; x \to \infty \tag{1.3}$$

$$E_e(x) \to \; -\frac{Q_e}{\varepsilon_e}, as \;\; x \to \frac{d}{2} - 0 \tag{1.4}$$

From Equations 1.1 – 1.4, E_e is,

$$E_e(x) \to \; -\frac{Q_e}{\varepsilon_e} e^{-\frac{x}{\lambda}} \tag{1.5}$$

Now, if we impose the continuity condition for *D* at FE/metal interface, we can obtain,

$$\varepsilon_{\mathrm{f}} E_{\mathrm{f}} - P = \; -\frac{Q_e}{\varepsilon_e} \tag{1.6}$$

where ε_{e} and E_f are the dielectric permittivity and electric field inside FE film. On the other hand, if no external power supply is connected to the capacitor, short circuit condition imply that there should be no voltage drop across the electrodes.

$$\int_0^{d/2} E_{\mathrm{f}} \; dx + \; \int_{d/2}^{\infty} E_{\mathrm{f}} \; dx = 0 \tag{1.7}$$

From Equations 1.5 and 1.7, we can derive formula,

$$E_{\mathrm{f}} \frac{d}{2} + \frac{\lambda}{\varepsilon_e} Q_e = 0 \tag{1.8}$$

By solving the Equations 1.6 and 1.8, we can finally obtain E_{f}.

$$E_{\mathrm{f}} = \frac{2P}{2\varepsilon_{\mathrm{f}} + \frac{\varepsilon_e}{\lambda} d} \tag{1.9}$$

As can be seen from the above relation, the size of the depolarizing field E_{f} inside the FE film becomes larger as the thin film becomes thinner. If the thickness of the thin film continuously decrease and E_{f} becomes larger than the coercive field of the thin film, the spontaneous polarization of the FE film cannot be stabilized and the thin film loses ferroelectricity. Equation 1.9 is a calculation result of an ideal case where we do not consider the change of the interface state of the thin film or the band bending of the electrode, and the case of using the semiconductor electrode. However, even when these parameters are taken into consideration, the tendency of increasing E_{f} with decreasing

film thickness does not change. Therefore, it is very important to understand the depolarizing field and its compensation mechanism for application of ultrathin FE materials.

1.2.3 Surface/interface effects on FE domain dynamics and FE polarization stability

The surface/interface structure of epitaxial FE thin film strongly affect the pinning dynamics of FE domain walls. The rough surface morphology is an indication of imperfect layer-by-layer growth and, thus, increased dislocation density. The structural defects generate locally induced inhomogeneous E inside film, that make nucleation occurred easily [8–10] but hinders subsequent domain wall propagation [15,21–23]. Moreover, in thin film, surface roughness itself can produce inhomogeneous E by heterogenieties in electrostatic boundary conditions at surface [24].

In ultrathin limit, stability of FE polarization strongly depends on atomic structure at surface/interface. Although it is widely believed that free electron charge at metal/ferroelectrics most efficiently minimize depolarizing field energy, in some case, screening from conducting electrode appears to be less effective [25,26]. A typical example is the ferroelectric BTO film sandwiched by SRO electrodes. Deposition of SRO electrodes results in severe relaxation to zero net polarization due to the incomplete screening of depolarizing field or reduced interfacial capacitance [25,26]. And in such cases, interface structure seems to play important role in determining limitation of ferroelectric stability [27,28]. In particular, formation of interface electric dipole help or disturb the compensation of depolarizing field, affecting the stability of FE polarization [29].

1.3 Outline of this thesis

The focus of this thesis is interface control of FE properties of ultrathin film. In **Chapter 2**, experimental tools to fabricate the FE film and investigate their properties are introduced. In particular, we provide detailed explanations on pulsed laser deposition (PLD) technique for oxide film fabrication and piezoelectric force microscopy (PFM) for investigating FE polarization switching. **Chapter 3** deals with the effect of surface/interface morphology on the *ac* dynamics of FE domain wall motion. We reveal that, by choosing proper interface structure, undesired non-linear *creep* dynamics and resulting strong dependence of $P - E$ hysteresis loops on measuring frequency can be significantly suppressed. The observed suppression of *creep* dynamics is closely related to energy landscape of FE domain wall, which comes from the defect states at interface. In **Chapter 4**, we demonstrate the selective control of interface termination sequence of $SrRuO_3/BaTiO_3/SrRuO_3$ heterostructure grown by pulsed laser deposition. By synergetic theoretical and experimental works, we reveal that surface/interface structuring of $BaTiO_3$ is highly dependent on thermodynamic energy of different surface structure. As a result, we can achieve *in-situ* control of interface termination sequence without depositing additional ABO_3 or other binary oxide layers. In **Chapter 5**, we investigate the effect of different termination sequence at $SrRuO_3/BaTiO_3$ interface on FE polarization switching properties of $BaTiO_3$ thin film. By PFM measurement, we show that the existence of $BaO\text{-}RuO_2$ interface termination sequence give rise to pinning of FE polarization along one direction, while reliable FE polarization switching is preserved with $SrO\text{-}TiO_2$ termination sequence. This work provide impact on the design of FE-related nanoelectronics devices, such as the ferroelectric tunnel junctions.

References

[1] M. E. Lines, A. M. Glass, G. Burns, *Phys. Today* **31**, 56, (1978).

[2] E. K. H. Salje, O. Aktas, X. Ding, *Topological Structures in Ferroic Materials* (Springer International Publishing, Cham, 2016).

[3] J. F. Scott, *Ferroelectric Memories* (Springer Berlin Heidelberg, Berlin, Heidelberg, 2000).

[4] M. Dawber, K. M. Rabe, J. F. Scott, *Rev. Mod. Phys.* **77**, 1083, (2005).

[5] S. Mathews, *Science* **276**, 238, (1997).

[6] R. Landauer, *J. Appl. Phys.* **28**, 227, (1957).

[7] A. K. Tagantsev, I. Stolichnov, N. Setter, J. S. Cross, M. Tsukada, *Phys. Rev. B* **66**, 214109, (2002).

[8] G. Gerra, A. K. Tagantsev, N. Setter, *Phys. Rev. Lett.* **94**, 107602, (2005).

[9] D. J. Kim et al., *Appl. Phys. Lett.* **91**, 132903, (2007).

[10] S. Jesse et al., *Nat. Mater.* **7**, 209, (2008).

[11] S. M. Yang, J.-G. Yoon, T. W. Noh, *Curr. Appl. Phys.* **11**, 1111, (2011).

[12] P. Gao et al., *Nat Commun* **2**, 591, (2011).

[13] J. F. Scott, C. A. Paz de Araujo, *Science* **246**, 1400, (1989).

[14] S. V. Kalinin et al., *Adv. Mater.* **22**, 314, (2010).

[15] J. Y. Jo et al., *Phys. Rev. Lett.* **102**, 45701, (2009).

[16] S. M. Yang et al., *Phys. Rev. B* **82**, 174125, (2010).

[17] C. Lichtensteiger, J.-M. Triscone, J. Junquera, P. Ghosez, *Phys. Rev. Lett.* **94**, 47603, (2005).

[18] Y. S. Kim et al., *Appl. Phys. Lett.* **86**, 102907, (2005).

[19] V. Nagarajan et al., *Appl. Phys. Lett.* **84**, 5225, (2004).

[20] S. Ducharme et al., *Nature* **391**, 874, (1998).

[21] T. Tybell, P. Paruch, T. Giamarchi, J. M. Triscone, *Phys. Rev. Lett.* **89**, 97601, (2002).

[22] S. M. Yang et al., *Appl. Phys. Lett.* **92**, 252901, (2008).

[23] P. Paruch, T. Giamarchi, J.-M. Triscone, *Phys. Rev. Lett.* **94**, 197601, (2005).

[24] A. Rajeev, N. Nathaniel, J. S. David, *Nanotechnology* **20**, 445709, (2009).

[25] D. Kim et al., *Phys. Rev. Lett.* **95**, 237602, (2005).

[26] V. Nagarajan et al., *J. Appl. Phys.* **100**, 1, (2006).

[27] M. Stengel, D. Vanderbilt, N. A. Spaldin, *Nat. Mater.* **8**, 392, (2009).

[28] C. G. Duan, R. F. Sabirianov, W. N. Mei, S. S. Jaswal, E. Y. Tsymbal, *Nano Lett.* **6**, 483, (2006).

[29] L. Xie et al., *Adv. Mater.* **1701475**, 1701475, (2017).

[30] C. T. Nelson et al., *Science* **334**, 968, (2011).

[31] D. Lee et al., *Adv. Mater.* **26**, 5005, (2014).

Chapter 2
Experimental details

2.1 Pulsed laser deposition

After discovery of high-temperature superconductors in late 1986, the puled laser deposition (PLD) was re-invented and has become one of most widely used film fabrication techniques. The PLD technique has a benefit for both speed of process and quality of resulting film. The high energy of focused laser effectively deliver the stoichiometry of target materials to the substrate. The high super-saturation density of target materials near the substrate surface gives rise to relatively fast growth of films, high nucleation density, and thus, smooth surfaces. In addition, combined with *in-situ* monitoring of growth by reflection high-energy electron diffraction (RHEED), the layer-by-layer growth enable an atomic scale control of oxide heterostructures.

In this chapter, the PLD system equipped with RHEED will be described. In particular, we give detailed descriptions on four stage of PLD process.

2.1.1 Basic principle of pulsed laser deposition

PLD is a physical deposition technique, carried out in a vacuum system [1,2]. As shown in Figure 2.1, PLD utilize a pulsed laser which is focused onto a target material to be deposited.

With sufficiently high-energy, the focused laser ablate a small amount of target materials and create a plasma plume that is in highly forward-directed to the substrate. The ablated plasma plume provide the material flux and super-saturation for film growth. The usage of high-energy laser makes remarkable features of PLD that is attractive for film growth, in particular, for complex oxide film synthesis. The high-energy of focused laser efficiently transfer stoichiometry of target material to growing film and makes the plum species in highly excited states. The excitation of materials give rise to increased hypothermal reaction between the plume species and background gas. In the case of oxide film growth, background oxygen gas is usually used for enhancing oxygen stoichiometry of the film. In addition, the ablation of target materials by pulsed laser is compatible with wide range of background gas pressure from ultrahigh vacuum (UHV) to approximately 1 Torr. The complex film with multilayer structure can be easily deposited by both single, stoichiometric target and multiple target. And high super-saturation density of ablated materials induce the dense nucleation of growing films. For such reasons, all the oxide heterostructure in this paper was fabricated by the PLD method.

The PLD process can be roughly divided into four stages: 1) Focused high-energy laser pulse (0.1 – 10 J/cm^2) impinges on ablation target materials, inducing a laser-ablated plasma plume. The spatial distribution of ablated atomic, diatomic, molecular, and ionic species in the plume follow a $\cos^n(\theta)$ where n can vary from 4-30. The detailed studies on complex interaction between laser and target surface can be found in Ref. [1]. 2) The generated plasma plume from target transverses into atmosphere. The plasma plume species can have kinetic energy up to several hundred eV so that the procedure in the stage is mainly governed by the high-energetic plasma dynamics [3]. The expansion of ablated plume takes few tens of

microseconds [4]. 3) The transferred plasma plume species bombard the substrate surface. The deposition of target materials causes the high-supersaturation near the substrate surface as well as the re-sputtering of grown film. 4) The supersaturated materials generate the nucleation of film cluster by re-condensation. After the nucleation, diffusion of adatom into the cluster and disassociation from cluster occur. At this stage, the kinetic energy of species is reduced down approximately to an eV due to interaction with background gas. The procedure of the stage, therefore, is mainly governed by low-energy kinetics.

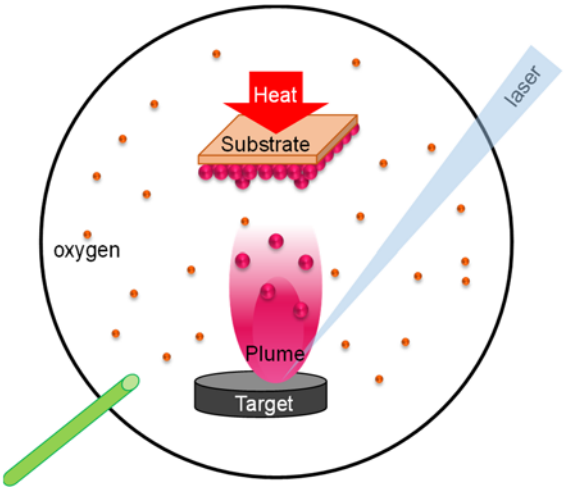

Figure 2.1. Schematic of pulsed laser deposition system.

2.1.2 PLD with reflection high-energy electron diffraction

The reflection high-energy electron diffraction (RHEED) is the method for monitoring surface structure and growth procedure of film [5]. In RHEED system, a high-energy electron beam (10 – 50 keV) arrives at a surface under a small grazing incident angle (0.1-5°). With such a high energy, the electrons can penetrate any material for several hundreds of nanometers.

However, due to the small grazing incident angle, the electrons only can interact with the few topmost layer of film surface (approximately 1 – 2 nm). After being diffracted by film surface, the electrons is collected into photo-luminescent detector screen at opposite side of chamber. The diffraction patterns of electrons on screen provide information of crystal structure and morphology of film surface.

The main difference between RHEED and other surface sensitive techniques, such as X-ray diffraction, scanning prove microscopy (SPM), and scanning tunneling microscopy (STM), is comparability with UHV environment of PLD. Because of small grazing incident angle, the electron diffraction pattern is do not disturbed by ablated plasma plume that is perpendicular to the film surface. The size of electron gun and screen is relatively smaller than that of other surface sensitive techniques so that RHEED can be easily attached to PLD systems. Moreover, the main reason why RHEED is popular is the observation of intensity oscillations of the specular spot during deposition. The surface diffraction of electron has basically same principle with X-ray diffraction. The difference comes from the variation in number of scattering site at growing film surface.. During the deposition of one atomic layer, the intensity decrease due to reduced number of diffraction centers. As a result, real-time intensity profile of RHEED specular spot exhibits the clear oscillation where each maximum correspond to growth of monolayer. Therefore, with help of RHEED, we can control the film growth in a unit-cell scale.

2.2 Piezoresponse force microscopy

2.2.1 Switching spectroscopy-piezoresponse force microscopy

Piezoresponse force microscopy is the mechanically detection of FE polarization state based on atomic force microscopy (AFM) [6]. All FE materials exhibit piezoelectric effect so that application of external electric field can induce the changes in mechanical strains. In FE materials, the effective piezoelectric coefficient tensor d_{im} has relation,

$$d_{\mathrm{im}} = \kappa_{\mathrm{ij}} Q_{\mathrm{mjk}} P_{\mathrm{sk}} \tag{2.1}$$

where, κ_{ij} is dielectric coefficients, Q_{mjk} is the polarization-related electrostrictive coefficients, and P_{sk} is the FE polarization tensor. Please note that, in the particular case of the tetragonal symmetry (e.g. $BaTiO_3$), "3" is the polar axis. As a result of linear relation between piezoelectric coefficient and polarization, one can detect direction of FE polarization state by measuring expansion or suppression of film volume. In PFM setup, the volume change s is detected by the deflection (D_{ac}) of cantilever tip that contact to FE film surface (Figure 2.2a). During the PFM measurement, the dc bias, $V_{dc,}$ with wave form in Figure 2.2b could be applied to sample via a conductive tip. The height of the each V_{dc} step varies with time so that we can measure FE polarization state at each V_{dc}. This method is called switching spectroscopy-PFM (SS-PFM).

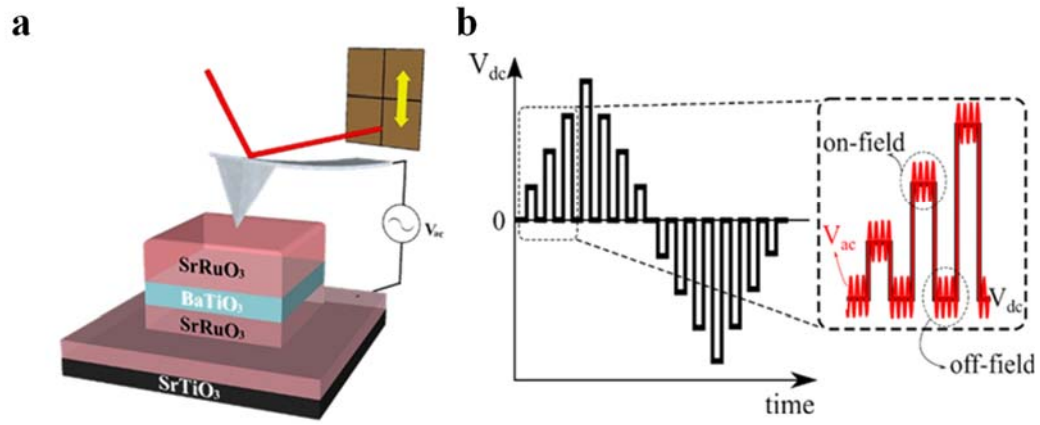

Figure 2.2. a) Schematic description of the piezoelectric force microscopy (PFM) hysteresis loop measurement on a SRO/BTO/SRO capacitor. b) Schematic of the electrical pulse sequence for the PFM hysteresis measurement.

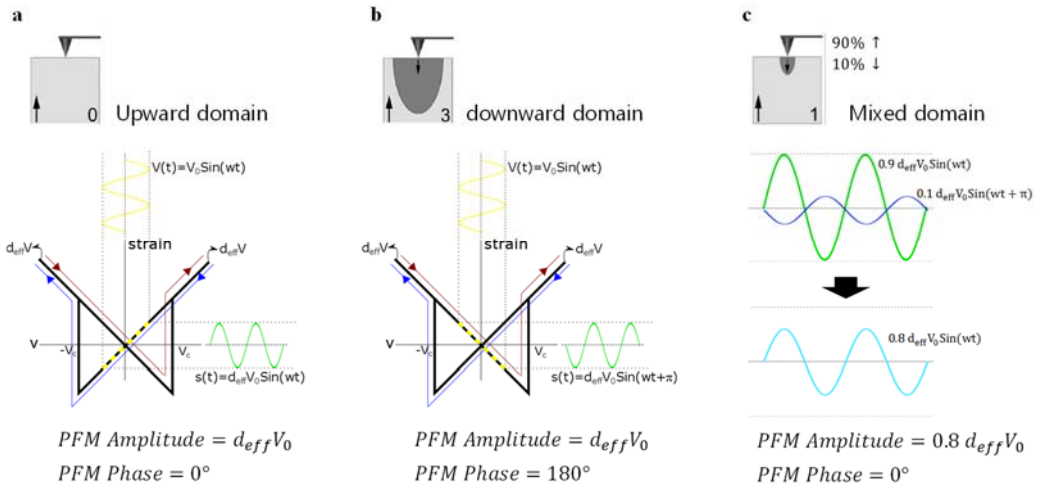

Figure 2.3. Schematic description of detecting polarization state by lock-in technique when a) FE polarization is pointing upward, b) FE polarization is pointing downward, and c) film has mixed upward and downward polarities.

Because the small piezoelectric coefficient (at most few tens of pm/V) and resulting small volume change, the FE polarization state only can be measured by application of *ac* bias, V(*t*) = $V_0\sin(\omega t)$, combined with lock-in technique. Here, the amplitude of V_0 should be smaller than the coercive voltage (V_C) of FE materials (detailed explanation on effect of choosing proper V_0 will be in Section 2.2.3.). Because strain and external bias have linear coupling, strain-bias curve should have butter fly-shape as depicted in Figure 2.3a and 2.3b. With the strain-bias curve, application of $V_{ac}(t)$ give rise to the variation of film strain $s(t)$ that also follows sinusoidal wave form. The lock-in technique measures parallel component ($C_{\parallel}$) and perpendicular component ($C_{\perp}$) of first harmonics of $s(t)$ by following formula.

$$\lim_{T\to\infty} \frac{1}{T}\int_{t-T}^{t} s(t)\, Sin(\omega t)dt = C_{\parallel} \tag{2.2 a}$$

$$\lim_{T\to\infty} \frac{1}{T}\int_{t-T}^{t} s(t)\, Cos(\omega t)dt = C_{\perp} \tag{2.2 b}$$

Then PFM amplitude and PFM phase are defined by

$$PFM\ Amplitude = \sqrt{C_{\parallel}^2 + C_{\perp}^2} \tag{2.3 a}$$

$$PFM\ Phase = Tan^{-1}\left(\frac{C_{\parallel}}{C_{\perp}}\right) \tag{2.3 b}$$

When the direction of polarization is along the direction of V_{ac} (Figure 2.3a), $V_{ac}(t)$ and $s(t)$ should be in-phase (PFM phase = 0°) and PFM amplitude exhibit its maximum value ($d_{eff}V_0$). If the direction of FE polarization is opposite to that of V_{ac} (Figure 2.3b), $V_{ac}(t)$ and $s(t)$ should be out-of-phase (PFM phase = 180°) but PFM amplitude still have maximum value ($d_{eff}V_0$). If the FE film underneath the tip has mixed FE domain along vertical direction (Figure 2.3c), resulting net $s(t)$ is just summation of strain variation at each FE domain region. As a result,

PFM phase has same direction with that of FE domain with major portion, but PFM amplitude exhibit reduced value. If we repeated the measurement during FE domain switching, we can obtain typical PFM amplitude and phase hysteresis loops as depicted in Figure 2.4a-2.4c. The d_{eff} can be deduced by measuring normalized PFM response (PFM/V_{ac}), which is defined as (PFM amplitude)×cos[(PFM phase)] (Figure 2.4c).

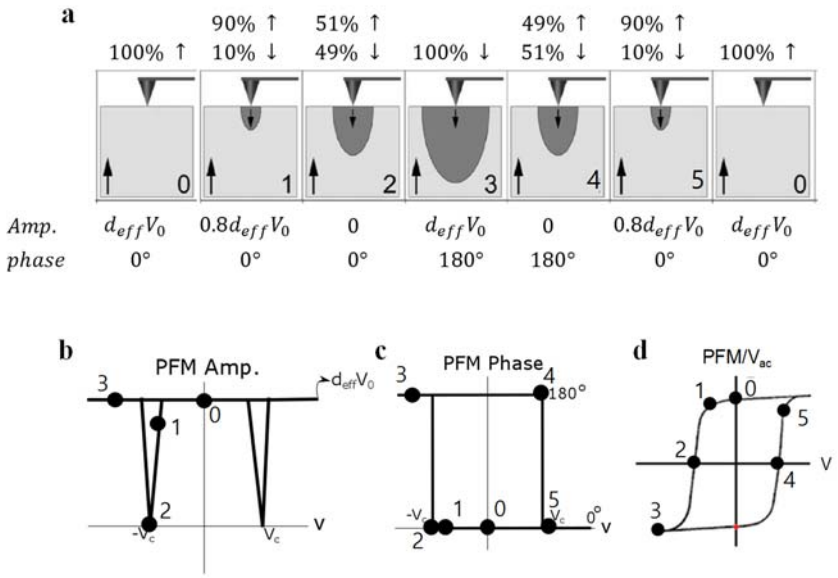

Figure 2.4. a) Sketch of FE polarization states with varying V_{dc}. b) Schematic description of PFM amplitude hysteresis loops. c) Schematic descriptions of PFM phase hysteresis loops. d) Schematic description of PFM/V_{ac} hysteresis loops.

2.2.2 Surface electrostatic effect on SS-PFM

The electrostatic force at FE film surface can be observed during SS-PFM measurement. When we perform SS-PFM, we can obtain two different curves at the same time: 1) SS-PFM

curve measured during application of V_{dc}, 2) SS-PFM curve measured at duration of each V_{dc} step (inset of Figure 2.2b). The former curve is called On-field SS-PFM curve and the letter is called Off-field SS-PFM curve. As depicted in Figure 2.5a and 2.5b, *s*(*t*) curves with and without V_{dc} are identical. However, On- and Off-field SS-PFM curve show clear difference as shown in Figure 2.5c. The difference comes from the electrostatic force at surface. Assuming the surface capacitance C_{surf}, the surface electrostatic force F_{surf} and induced cantilever deflection D_{es} can be derived as,

$$F_{\mathrm{surf}} = \frac{1}{2}\frac{dC_{\mathrm{surf}}}{dx}V^2 \tag{2.4a}$$

$$D_{\mathrm{es}} = \frac{1}{2}k^{-1}\frac{dC_{\mathrm{surf}}}{dx}V^2 \tag{2.4b}$$

where, *x* is coordinate along vertical direction, *V* is an external bias, and *k* is a spring constant of cantilever. During On-field curve measurement, we applied $V = V_{\mathrm{dc}} + V_0\sin(\omega t)$. Thus, D_{es} is

$$D_{es} = \frac{1}{2}k^{-1}\frac{dC_{\mathrm{surf}}}{dx}\left(V_{\mathrm{dc}}^2 + V_0^2\sin(\omega t)^2 + V_0V_{\mathrm{dc}}\sin(\omega t)\right) \tag{2.5}$$

Because lock-in technique only detect the sin(ω*t*) term, the surface electrostatic force affect On-field PFM curve by $\frac{1}{2}k^{-1}\frac{dC_{\mathrm{surf}}}{dx}V_0V_{\mathrm{dc}}$. Please note that the surface electrostatic force give rise to linear term with respect to V_{dc} as observed in Figure 2.5c.

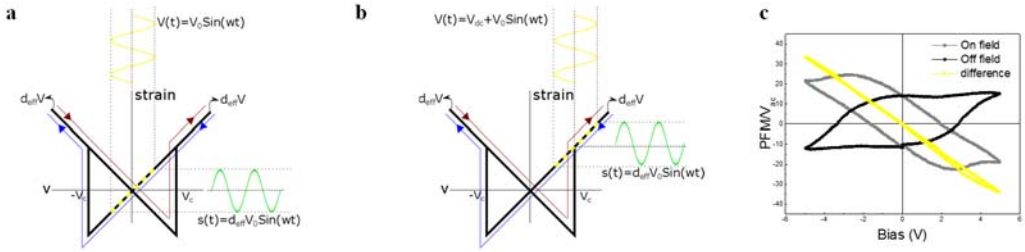

Figure 2.5. Schematic description of a) off-field and b) on-field PFM measurement. c) On-field (gray) and Off-field (black) PFM hysteresis loops of 12-unit cells-thick $BaTiO_3$ film. The yellow curve shows the difference between On- and Off-field hysteresis loops.

2.2.3 V_{ac} dependence of SS-PFM hysteresis loops

The proper choice of V_{ac} amplitude (V_0) is important for SS-PFM measurement. In particular, SS-PFM hysteresis loops show abrupt change near $V_0 = V_C$. As depicted in Figure 2.6a, when $V_0 > V_C$, the polarity of FE polarization keep being switched during measurement. As a result, $s(t)$ does not have sinusoidal form. Instead, $s(t)$ become,

$$s(t) = \begin{cases} d_{eff}V_0\, Sin(\omega t), & if\ 2n\pi + \omega\tau < \omega t < (2n+1)\pi + \omega\tau \\ d_{\mathrm{eff}}V_0\, Sin(\omega t + \pi), & if\ (2n+1)\pi + \omega\tau < \omega t < (2n+3)\pi + \omega\tau \end{cases}$$

where, $\omega\tau = Sin^{-1}\left(\frac{V_c}{V_0}\right)$ and n is an integer number. Please note that with $V_0 > V_C$, period of $s(t)$ is changed from $\frac{2\pi}{\omega}$ to $\frac{\pi}{\omega}$. As a result, both $C_{\parallel}$ and $C_{\perp}$ converges to 0 (Figure 2.6c and 2.6d, respectively). In such a case, PFM amplitude become zero and PFM phase cannot be defined. Figure 2.7 shows the SS-PFM hysteresis loops of FE $BaTiO_3$ film with varying V_0. Both Off- and On-field hysteresis loops show abrupt collapse near $V_C = 3$ V. The V_{ac}-dependent SS-PFM hysteresis loops can also be used for probing existence of ferroelectricity. The PFM hysteresis loops that originate from other effect do not exhibit such abrupt collapse near V_C,

due to absent of real polarization switching. This will be discussed again in Chapter 5

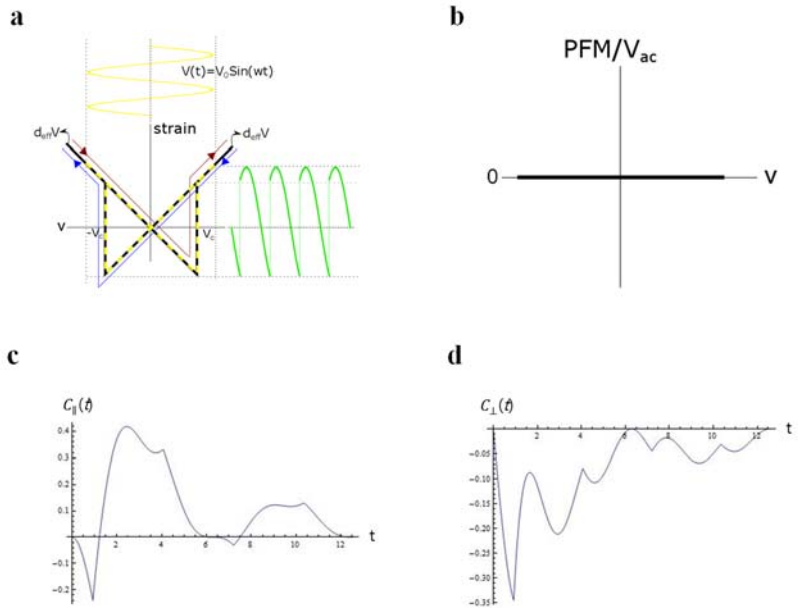

Figure 2.6. a) Schematic description of SS-PFM measurement with $V_0 > V_C$. b) Schematic of PFM/V_{ac} hysteresis curve with $V_0 > V_C$. Plot of c) parallel component ($C_{\parallel}$) and d) perpendicular component ($C_{\perp}$) of lock-in signal with respect to time, *t*, measured with $V_0 > V_C$.

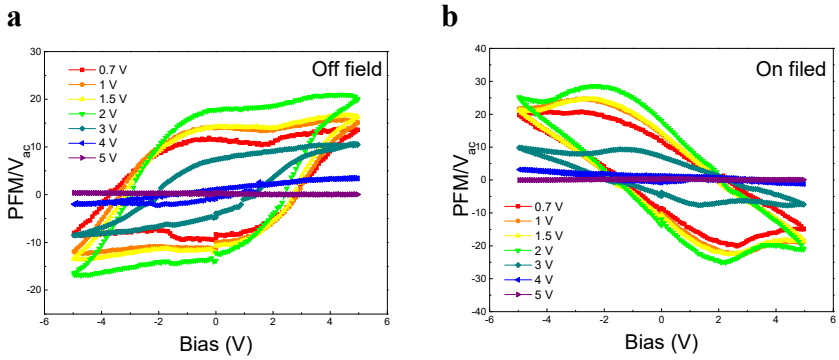

Figure 2.7. a) Off-field and b) On-field PFM hysteresis loops with varying V_o.

References

[1] G. K. Hubler, D. B. Chrisey, (1994).

[2] Robert Eason, *Pulsed Laser Deposition of Thin Films* (John Wiley & Sons, Inc., Hoboken, NJ, USA, 2006).

[3] S. A. Chambers, *Adv. Mater.* **22**, 219, (2010).

[4] J. Z. Tischler et al., *Phys. Rev. Lett.* **96**, 226104, (2006).

[5] A. Ichimiya, P. I. Cohen, *Reflection High-Energy Electron Diffraction* (Cambridge University Press, Cambridge, 2004).

[6] S. Jesse, A. P. Baddorf, S. V. Kalinin, *Appl. Phys. Lett.* **88**, 21, (2006).

Chapter 3
Surface/interface morphology effect on *ac* creep dynamics of ferroelectric domain walls

Switching dynamics of ferroelectric materials are governed by the response of domain walls to applied electric field. In epitaxial ferroelectric films, thermally-activated 'creep' motion plays a significant role in domain wall dynamics, and accordingly, detailed understanding of the system's switching properties requires that this creep motion be taken into account. Despite this importance, few studies have investigated creep motion in ferroelectric films under *ac*-driven force. Here, we explore *ac* hysteretic dynamics in epitaxial $BiFeO_3$ thin films, through ferroelectric hysteresis measurements, and stroboscopic piezoresponse force microscopy. We reveal that identically-fabricated $BiFeO_3$ films on $SrRuO_3$ or $La_{0.67}Sr_{0.33}MnO_3$ bottom electrodes exhibit markedly different switching behaviour, with $BiFeO_3$/$SrRuO_3$ presenting essentially creep-free dynamics. This unprecedented result arises from the distinctive spatial inhomogeneities of the internal fields, these being influenced by the bottom electrode's surface morphology. Our findings further highlight the importance of controlling interface and defect characteristics, to engineer ferroelectric devices with optimised performance.

3.1 Introduction: *ac* dynamics of FE domain wall

Ferroic materials, such as ferromagnets and ferroelectrics, are used in numerous emerging technological applications, including energy harvesting [1,2], actuators [3,4], tuneable microwave devices [5,6], and non-volatile memories [7–11]. To optimise the operation speed

of such devices, understanding the frequency-dependent response of the active material is crucial. Under *ac* field, ferroic materials typically show hysteretic behaviour that is strongly influenced by changes in the drive frequency f. Even though this hysteretic behaviour has been studied for more than 100 years [12,13]; the underlying frequency-dependent dynamics remain far from being fully understood.

Hysteresis observed in ferroic materials is due to the motion of domain walls, the boundary between physical regions, *i.e.* domains, with distinct ordering parameters. With disorder, domain wall dynamics can be described by pinning-dominated motion of elastic objects driven by an external force. This concept has become a standard framework for describing a wide variety of physical systems, including vortices in type-II superconductors [14], dislocation lines in crystals [15], charge density waves in solids [16], stripe phases, and domain walls in ferromagnets [17–19] and ferroelectrics [20,21].

Domain wall motion under constant *dc* force can be conceptually separated into three dynamic regimes [21–23], illustrated schematically in Figure 3.1. At zero temperature, the domain walls are pinned by disorder and do not move under a small driving force, E. (For ferroelectric domain walls, E corresponds to external electric field.) Above a critical driving force E_{C0}, a *depinning* transition occurs. After this transition, the objects have an average velocity v that is linearly proportional to E; this is the *flow* regime. At finite temperature, thermal effects 'smear out' the depinning transition, and a finite velocity is expected for non-zero field. In this case, the movement of the objects in the low field regime is usually described by thermally-activated motion, known as *creep*. Despite significant research on creep-dominated dynamics [16–21], this regime of domain wall behaviour is not well understood,

particularly in the case of *ac* driven field.

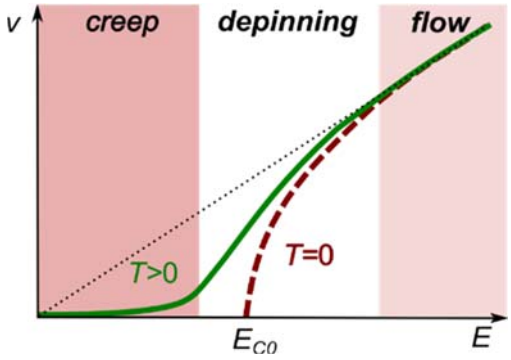

Figure 3.1. Theoretically-predicted domain wall velocity (v) for a pinning dominated system under dc electric field. The three dynamic regimes (creep, depinning, flow) are indicated by different colors. E_{C0} represents a dynamic threshold field at zero temperature.

In this Chapter, we explore *ac*-driven hysteretic dynamics of epitaxial thin films of ferroelectric $BiFeO_3$ (BFO) grown on $SrTiO_3$ (STO) substrates. The BFO layers were deposited in identical growth conditions (as described in Methods), but with different bottom electrodes, $La_{0.67}Sr_{0.33}MnO_3$ (LSMO) and $SrRuO_3$ (SRO), and identical top Pt electrodes. Despite the identical preparation conditions, we show here that the *ac*-driven dynamics of the two systems are significantly different. In particular, we find that the SRO bottom electrode gives rise to previously unobserved creep-free hysteretic dynamics, which is the result of a reduced state of disorder. Our findings suggest that judicious choice of bottom electrode can significantly alter domain wall dynamics, and we propose a conceptual framework explaining our observations.

3.2 Experiments

3.2.1 Sample preparations

Epitaxial BFO thin films used in this chapter were deposited by pulsed laser deposition using a KrF excimer laser (λ=248nm) on bottom electrodes of epitaxial LSMO or SRO, prepared on STO substrates with a 4° miscut toward the [100] direction. The BFO thickness, measured by scanning electron microscopy (SEM) on the sample edge, was 280 nm on LSMO and 232 nm on SRO. Further details on the structural and physical properties are published in Ref.[24,25]. Capacitor structures $75 \times 75 - 175 \times 175$ μm^2 in size were fabricated by depositing 40 nm thick Pt by *dc* magnetron sputtering and patterning using conventional photolithography.

3.2.2 Electrical measurements

Polarization-electric field (P-E) hysteresis loops and switching currents were measured using a AixACCT TF Analyzer 2000, employing a triangular electric field waveform over the frequency range 50-2000 Hz. E_C was extracted from the loops according to average of the values of E where $P = 0$ obtained at positive and negative fields. An imprint of 5-15 kV/cm was observed. This imprint has been removed so as to clearly compare the frequency-dependent characteristics of the two systems. Since the imprint is considerably smaller than E_C, this small correction does not impact the experimental findings or outcome of this study. Temperature dependent P-E hysteresis loops were measured using a low-temperature cryostat using liquid helium.

3.2.3 Stroboscopic piezoresponse force microscopy

Stroboscopic piezoelectric force microscopy (PFM) was performed using a Park Systems XE-100 scanning probe microscope with commercially-available non-conductive silicon tips (NSC36/AIBS, Mikromasch); images were obtained by applying a harmonically oscillating electric field ($f = 17.1$ kHz) using a separate needle probe in contact with the top electrode [26–28]. The converse piezoelectric response was detected using a lock-in amplifier (SR830, Stanford Research Systems), yielding amplitude and phase signals. For domain growth measurements, square pulses with amplitude given by $1.1E_C$ (at 2 kHz) from a function generator (FG300 Yokohama) were applied to the sample's lower electrode while the tip was grounded. The pulse width was 100 μs for BFO/LSMO and 20 μs for BFO/SRO, so chosen to be adapted to the different domain wall velocities of the two systems. Before PFM measurements, the BFO film was fully poled in one direction, then the opposite voltage was applied as a series of rectangular pulses with constant amplitude. Between the pulses, PFM imaging was performed (Figure 3.2). The total applied time t_{tot} is defined as the sum of the time during which E is applied. We confirmed the validity of our stroboscopic PFM measurements using variable pulse widths, following the procedure described in Ref. [28]. We found that the switched domain state was preserved before and after PFM image acquisition without evidence of polarisation relaxation or back-switching, confirming that the obtained PFM images are true representations of the domain wall configuration after applying a constant electric field of duration t_{tot}.

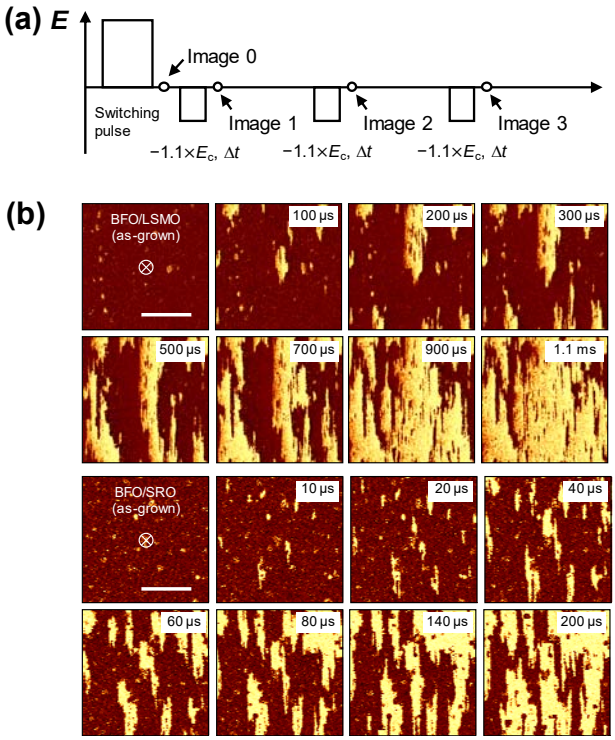

Figure 3.2. (a) Schematic of applied E pulses. Before measurement, a strong switching pulse is applied for ~1 ms to create a mono-domain state. The sequence of E pulses are applied in a certain time interval Δt. The amplitude of the pulses is chosen to be $1.1E_C$ at 2000 Hz. The Δt are 100 μs and 20 μs for BFO/LSMO and BFO/SRO, respectively. Between each E pulse, PFM image scans are performed. (b) The obtained PFM images by the sequence described in (a). Bright and dark regions represent domains with upward and downward polarization, respectively. Scale bars, 10 μm. All PFM phase images were obtained at the same location of each film.

3.3 Results

3.3.1 Frequency-dependent $P-E$ hysteresis loops

First we consider room-temperature polarisation-electric field (P-E) hysteresis loops. P-E loops measured on Pt/BFO/LSMO capacitors (Figure 3.3a) are strongly frequency dependent: higher frequencies induce a decrease in the slope dP/dE, and an increase in the coercive field E_C. A log-log plot of E_C versus frequency (Figure 3.4 a) shows that it scales as a power law with $E_C \propto f^{\beta}$ (Refs. [29–36]). These data, when normalised, are consistent with previously-reported data for other epitaxial ferroelectric films [30,31] (Figure 3.4 b). The two distinct scaling regions observed in this system likely originate from a dynamic crossover between creep and viscous flow regimes [31,36].

In strong contrast, room-temperature P-E hysteresis loops measured on Pt/BFO/SRO capacitors (Figure 3.3b) are virtually frequency independent, and the corresponding plot of E_C- f (Figure 3.4a and 3.4b, red triangles) shows a single scaling regime with small β. We stress here that these data are fundamentally different from those of typical ferroelectric films, such as epitaxial $Pb(Zr_{1-x},Ti_x)O_3$ (PZT), whose E_C- f data [30,31] are also shown in Figure 3.4 b. This suggests that the domain wall motion in our two systems is governed by markedly different *ac*-driven hysteretic dynamics.

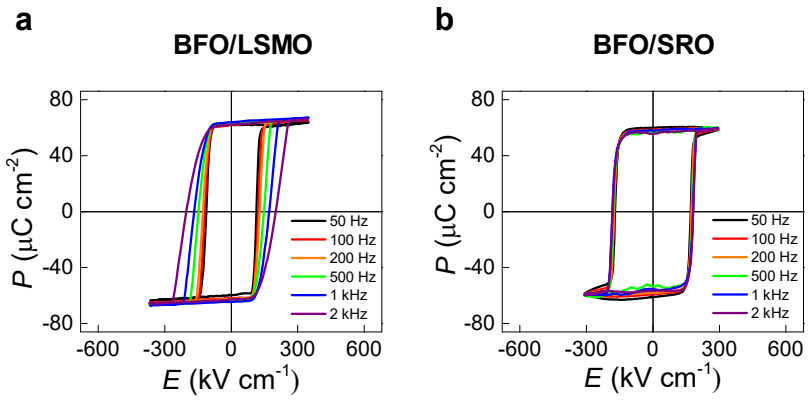

Figure 3.3. (a) Room-temperature polarization-electric field (P-E) hysteresis loops of BFO/LSMO film. (b) Room-temperature P-E hysteresis loops of BFO/SRO film.

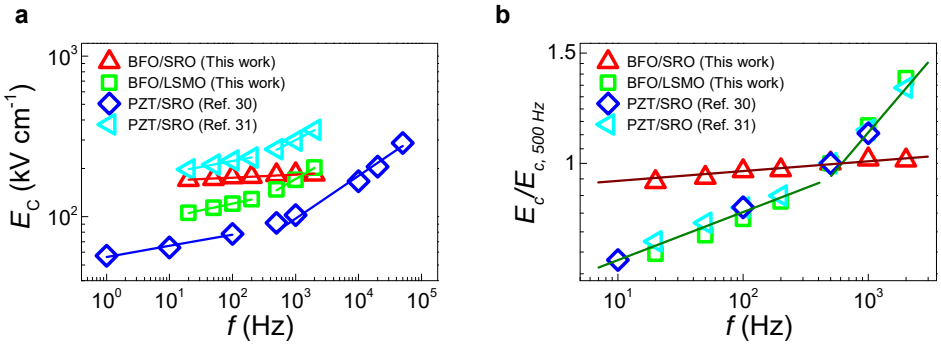

Figure 3.4. (a) log-log E_C-f plot of our BFO films with comparison to previously-reported data for PZT films. The solid lines are fitting results using $E_C \propto f^{\beta}$. (b) Normalized E_C-f plot of BFO and PFM films according to the value of E_C at $f = 500$ Hz for clarity.

3.3.2 Domain wall propagation and nucleation

The next step is to examine how the domain walls propagate under applied electric field. We employ stroboscopic piezoresponse force microscopy (PFM) [26–28], a versatile technique that allows direct visualisation of time-dependent polarisation changes (see Chapter 3.2.3.). Overlaid out-of-plane PFM phase images for the BFO/LSMO and BFO/SRO films are presented in Figure 3.5a and 3.5b where the colours indicate the domain configuration after the application of switching pulses of a particular accumulated time t_{tot}. Comparison of these images, keeping in mind the different time increments in each case, shows that for BFO/SRO, after a shorter accumulated time, a larger area is switched. This implies a higher domain wall velocity in BFO/SRO.

Quantitative information on the domain wall dynamics is obtained using the Kolmogorov-Avrami-Ishibashi (KAI) model [37]:

$$\Delta p = 1 - \exp(-(t/t_0)^n);$$

where Δp is the volume fraction of switched polarisation, t_0 the characteristic switching time, and n the geometric dimension of the domains. The experimental Δp for our BFO films, estimated from analysis of the PFM images, is plotted against t_{tot} in Figure 3.5c. A monotonic increase in Δp is observed, and its growth is much more rapid for the BFO/SRO film. Fitting these data to the KAI model (solid lines in Figure 3.5c) with $n = 1$, consistent with the observed 1D-like domain propagation (see the Figure 3.6), yields t_0 values for BFO/LSMO and BFO/SRO of 1164 ± 1 μs and 252 ± 1 μs, respectively. Since domain wall velocity v is inversely proportional to t_0 (Ref. [37]), we conclude that the domain walls in BFO/SRO propagate about five times faster than in BFO/LSMO.

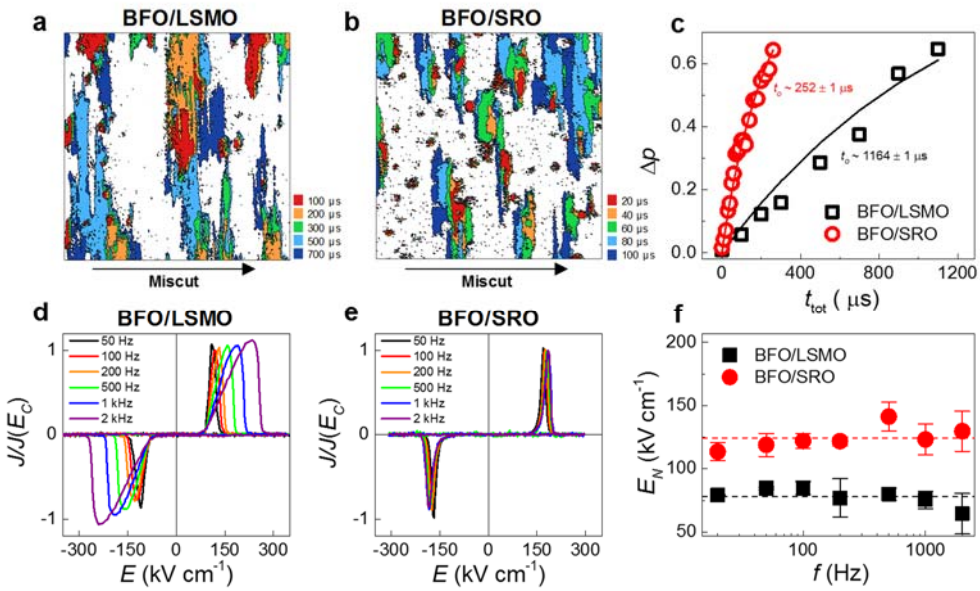

Figure 3.5. Domain nucleation and propagation characteristics. Overlaid out-of-plane phase images (25 μm^2) of switched domains for (a) BFO/LSMO and (b) BFO/SRO films, measured by stroboscopic PFM. Areas of different colours represent switched domain regions at particular accumulated pulse time t_{tot}. (c) Volume fraction of switched polarization (Δp) plotted as a function of t_{tot}. The solid lines show results of the KAI model fitting with $n = 1$. The characteristic switching time t_0 is smaller for BFO/SRO, indicating faster domain wall propagation. Normalized switching current curves of (d) BFO/LSMO and (e) BFO/SRO. (f) Plot of minimum nucleation field (E_N) as a function of f. The dashed lines denote the average E_N values for each film.

More careful inspection of the overlaid PFM images reveals details of the nucleation process. For the BFO/LSMO film (Figure 3.5a), domain nuclei of opposite polarisation appear over a wide t_{tot} range, and, more specifically, nuclei start to appear at $t_{\mathrm{tot}} < 100$ μs but newly-nucleated domains continue to appear even at $t_{\mathrm{tot}} = 700$ μs. In epitaxial PZT films, Kim *et al*. showed that the number of nuclei is linearly proportional to $\log(t_{\mathrm{tot}})$, suggesting a broad distribution of activation energies for nucleation [27]. This picture is consistent with our present observation in the BFO/LSMO system.

For the BFO/SRO film (Figure 3.5b), on the other hand, the nucleation of all domains takes place within 20 μs, and subsequent domain switching systematically occurs in regions adjacent to already-switched domains. The new formation of domains does not occur after the initial surge of nucleation at ~20 μs; that is, all further domain switching takes place via sideways growth. This suggests that the nucleation process for the BFO/SRO system can be defined by a narrower distribution of activation energies.

A quantitative comparison of the nucleation energies in the two systems is obtained through analysis of the time-dependent switching current density (J) during polarisation reversal (see Chapter 3.2.2.). J-E hysteresis curves (in which J is normalised to its value at the coercive field) for both samples at various frequencies are presented in Figure 3.5d and 3.5e. For BFO/LSMO, increasing frequency causes the J-E curves to broaden significantly, consistent with i) the nucleation process taking place over a rather wide t_{tot} range, and ii) lower domain wall velocity. In contrast, for BFO/SRO, the J-E curves remain very sharp and show negligible frequency dependence (Figure 3.5e), coherent with the reasoning that nucleation occurs in a narrow time window and that switching is completed more quickly via

faster domain wall propagation. From the J-E curves, we extracted the *minimum* electric field value (E_N) at which domains start to nucleate, taking it to be the value of E when J reaches 1% of $J(E_C)$. The E_N values for BFO/LSMO and BFO/SRO (Fig. 2f, solid black squares and red circles, respectively) indicate that the first few nuclei of opposite polarisation appear at around the same value of field, regardless of frequency. Importantly, the E_N value for BFO/LSMO is smaller by a factor of about 1.6 than that for BFO/SRO, suggesting, perhaps surprisingly, that the nucleation process commences at *lower* E in BFO/LSMO.

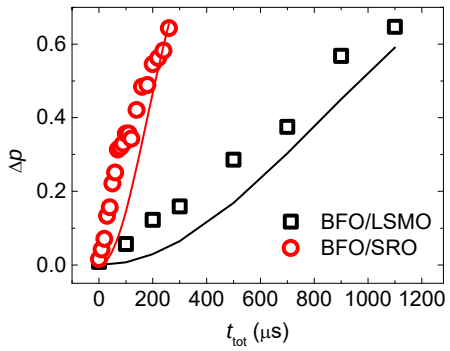

Figure 3.6. The same data as Figure 3.5c, with KAI model fitting results using $n = 2$. In contrast to the results with $n = 1$ in Figure 3.5c, the fitting results do not accurately describe the data. This indicates that the domain wall motion in the BFO films is closer to 1D-like motion than typical 2D motion.

3.3.3 Surface morphologies

Since, in ferroelectric thin films, nucleation occurs predominantly at the surface and/or interface [27,38,39] of the film, the surface topography of the BFO layer for the two cases can give us hints as to why the nucleation processes differ. Atomic force microscopy (AFM) topography images (Figure 3.7a and 3.7b) reveal that they have markedly different surface morphologies: BFO/SRO, with root-mean-square (*rms*) roughness ~1.50 nm, has a much flatter surface than BFO/LSMO (*rms* roughness ~3.86 nm). The distinction is seen more clearly in corresponding line scans (Figure 3.7c and 3.7d) which indicate that the height variation of the BFO/SRO film is considerably smaller than that for the BFO/LMSO film. Since domain wall pinning is more likely to occur for the film with larger surface roughness [40,41], these topography images suggest that the BFO/LSMO film has a *higher density* of *stronger* pinning sites.

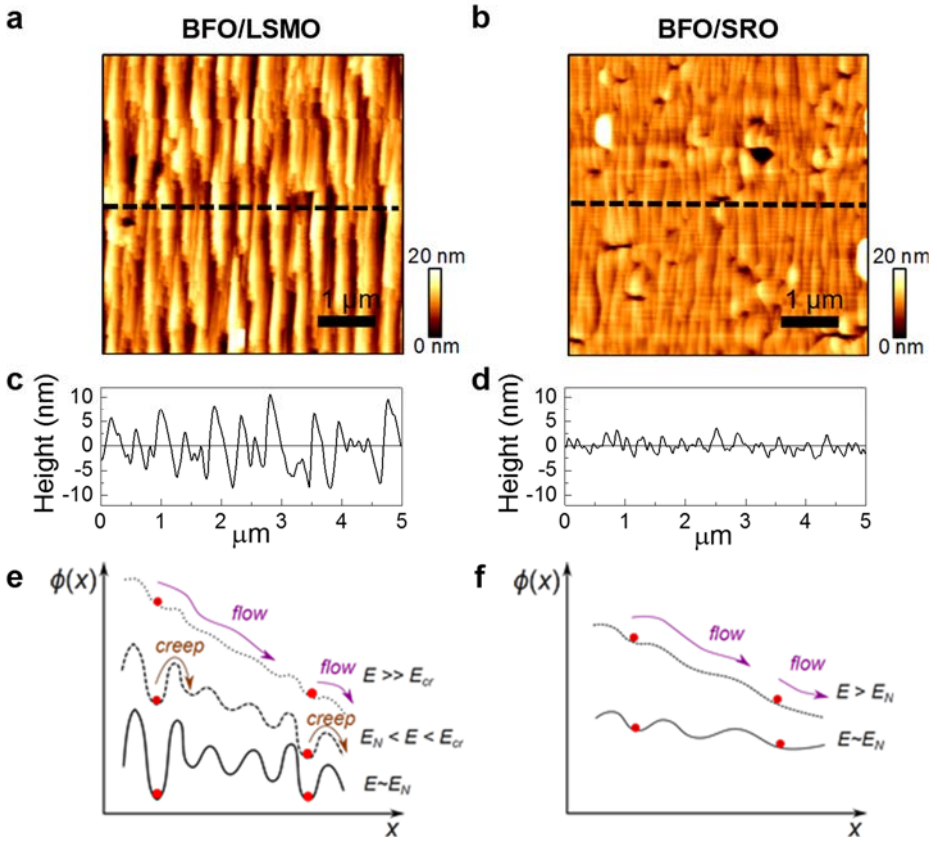

Figure 3.7. Surface morphology and schematics of the energy landscape in BFO thin films. AFM topography images of (a) BFO/LSMO and (b) BFO/SRO films. Line profiles of (c) BFO/LSMO and (d) BFO/SRO surfaces, taken along the dashed lines in (a) and (b). Clear step-bunching is observed for both BFO films. Schematic diagram of pinning energy landscape ($\phi(x)$) in (e) BFO/LSMO and (f) BFO/SRO films. The red circles denote *positions* at which nucleation occurs. The arrows represent domain wall motion, depending on applied field E and the pinning energy barrier.

3.3.4 Temperature-dependent hysteretic dynamics

To further understand the effects of domain wall pinning, we now turn to the influence of temperature on the switching dynamics. We measured P-E hysteresis loops for the two systems over a wide temperature range. Decreasing the temperature to below 100 K suppresses the two-scaling behaviour exhibited by the BFO/LSMO film, as evidenced by E_C- f curves (Figure 3.8a). The β values at high (500–2000 Hz) and low (20–200 Hz) frequency scaling regimes (Figure 3.8c, red squares and circles respectively) merge, and the corresponding β value is rather small. Since the two-scaling behaviour is a hallmark for the existence of the dynamic crossover between creep and viscous flow regimes[31,36], the merging of the exponent β at low temperature signifies an essential change in domain wall dynamics; namely, the suppression of the creep regime.

The E_C - f plot for the BFO/SRO film (Figure 3.8b), derived from hysteresis measurements carried out at various temperatures, does not exhibit a change in scaling behaviour. Rather, β is invariant down to low temperature, indicating that the BFO/SRO system does not exhibit a dynamic crossover, even at room temperature. Importantly, at low temperature the β values for the BFO/LSMO film are comparable to those for the BFO/SRO film, implying that the dynamics of the two systems are similar in this temperature window.

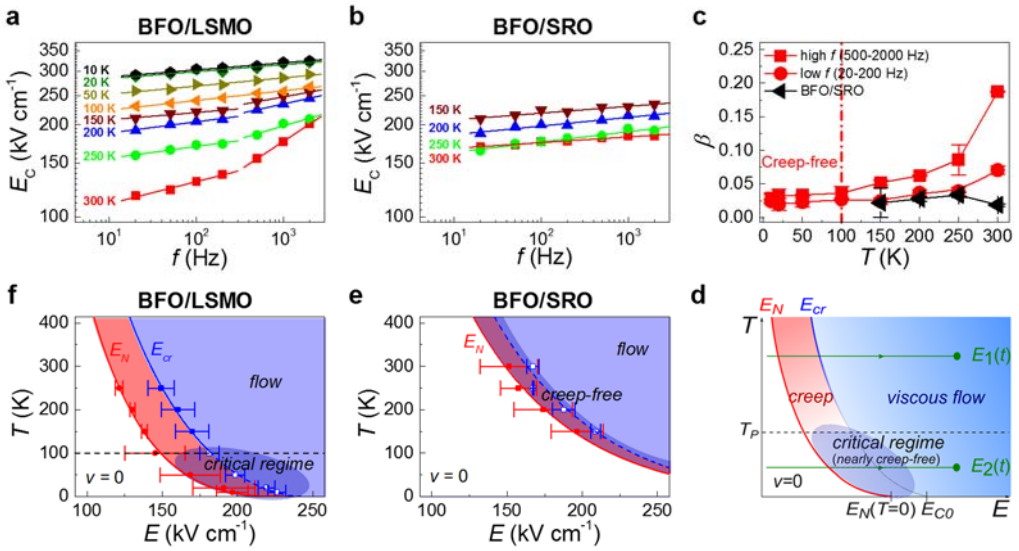

Figure 3.8. Temperature (T)-dependent hysteretic dynamics. log-log E_C-f plot for (a) BFO/LSMO and (b) BFO/SRO film at various temperatures. (c) Plot of β values with respect to f. The β values of BFO/LSMO at low f (20-200 Hz) and high f (500-2000 Hz) are represented by red circles and red squares respectively. The left-side of the (red) dashed line indicates the low-temperature creep-free regime of BFO/LSMO. The β values for BFO/SRO are represented as black triangles. (d) Phase diagram of hysteretic domain wall dynamics under *ac*-driven field. The solid red lines E_N and blue E_{cr} show the dynamic crossover between no nuclei, creep, and viscous flow regimes. The regimes where creep or viscous flow motion govern domain wall dynamics are shaded red and blue, respectively. The green lines $E_1(t)$ and $E_2(t)$ represent the first $1/4f$ of applied *ac* field at two different temperatures. The horizontal dashed line denotes the temperature T_P, related to the typical pinning energy E_P. Phase diagrams derived from (f) BFO/LSMO data and (e) BFO/SRO data. Red circles indicate E_N and blue solid squares and open squares present E_{cr} and the critical regime, respectively. Lines are guides to the eye.

3.4 Discussions

3.4.1 Discussion on hysteretic phase diagram of *ac*-dynamics

For ferromagnetic materials, Nattermann *et al.* developed a theory on *ac* hysteretic domain wall propagation dynamics [42]. Using this general framework of pinning-dominated dynamics in a ferroic system, we have extended this theory to explain our present observations. The theory considers that a domain wall exists for any external field, and it predicts a *relaxation* regime of $v = 0$ for values of applied field lower than that needed to enter the creep regime. In this relaxation regime, a domain wall cannot overcome the depinning energy from a pinning site before the external *ac* field changes its polarity. However, for fully-saturated P-E hysteresis loop measurements, all domains are switched to one mono-domain at the maximum value of field. For a reversed domain to nucleate, it must first overcome the activation energy barrier. Since, in epitaxial films, the activation barrier is generally higher than the depinning barrier [43], the dynamics of a freshly-nucleated domain are described by the creep regime. For this reason, we replace the relaxation regime of Natterman's theory by a regime labelled '*no nuclei*'. In this case, the existence of the *v*=0 regime below E_{N} is due to the fact that there is no domain wall in the system.

We now consider the typical pinning energy of a domain wall, E_{P}, and we define a temperature $T_{\mathrm{P}} = E_{\mathrm{P}}/k_{\mathrm{B}}$, which can be thought of as a 'pinning temperature'. For temperatures above this threshold, *i.e.* $T > T_{\mathrm{P}}$, thermally-induced hopping (creep) is possible and the hysteretic behaviour of the system exhibits a dynamic crossover at E_{cr}, separating the creep and viscous flow regimes. In this temperature window, a domain wall first undergoes

motion in the creep regime, after which, upon increasing E, it can enter the flow regime. It is important to remember that this boundary is not an abrupt transition but a crossover (as in Figure 3.1), whereby a gradual change occurs over a rather broad *E* range around the transition threshold.

For $T \ll T_{\mathrm{P}}$, that is, when the thermal energy is lower than the typical pinning energy, the critical depinning regime plays a role in the hysteretic dynamics. In this temperature window, the domain propagation is strongly pinned by disorder until the drive field reaches a dynamic threshold E_{C0}. At $E \approx E_{\mathrm{C0}}$, the domain undergoes a pinning-depinning transition and begins to propagate (Figure 3.1, red dashed line) with velocity $v \propto (E - E_{C0})^{\theta}$, where the critical exponent θ is determined by pinning forces and the fractal nature of the system. Since, in this case, v is not governed by thermally-activated hopping, creep motion is suppressed, and E_{cr} has no meaning. In other words, immediately after a given domain wall nucleates, it passes directly into the flow regime without experiencing creep motion.

As described in Figure 3.8d, an *ac* measurement is performed along the horizontal lines (*e.g.* $E_1(t)$). The measurement frequency defines how quickly the *ac* field moves on this line. Depending on frequency, the absolute time the field stays in each regime is different (see Figure 3.9), explaining the origin of the different β values in the f-E_{C} plot. The frequency value where β changes indicates that half of the polarisation is switched at the boundary of creep and flow regimes. Therefore, at the crossover frequency, $E_{\mathrm{C}} = E_{\mathrm{cr}}$.

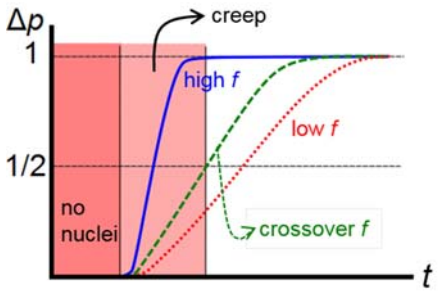

Figure 3.9. The schematic describing how f can give different β vales in log(f)-log(E_C) plot.

3.4.2 Hysteretic phase diagram of BFO films

It is important to emphasise the temperature T_P which defines the upper boundary of the 'critical regime.' Above this temperature, the thermal energy is high enough to allow hopping and as a result the 'creep' regime separates the 'no nuclei' and 'viscous flow' regimes. The value of field required to transition from creep to flow dynamics is the dynamic crossover field E_{cr}. For temperatures below T_P, the 'critical regime' corresponds to behaviour such that the thermal energy is not sufficient to allow creep motion, and therefore upon increasing field, domain wall dynamics pass directly from 'no nucleation' to 'flow.' In this region creep motion is suppressed, and since the dynamic crossover does not exist, E_{cr} cannot be defined.

Using this phase diagram for *ac* hysteretic dynamics, we explain the temperature-dependent E_{C} values exhibited by the BFO/LSMO system (Figure 3.8a). During *ac* hysteresis loop measurement, the amplitude of the electric field is varied periodically between $\pm E_{\max}$, where $E_{\max} > E_{\mathrm{C}}$. During the first quarter of one period, *i.e.* $t \leq \frac{1}{4f}$, $E(t)$ increases from zero to $E_{\max}$.

For $T > 100$ K, the *ac* measurement can be considered as following the path defined by $E_1(t)$, passing through the dynamic crossover at E_{cr}. At low frequency, polarisation reversal is completed well before the flow regime is reached. At high frequency, however, $E_1(t)$ passes through the creep regime so quickly that switching is not completed until after the flow regime has been entered. This interpretation is consistent with the different high- and low-frequency β values in Figure 3.8a.

In contrast, for $T < 100$ K, the *ac* measurement can be described by the path $E_2(t)$. Since this path does not pass through the crossover E_{cr}, domain walls propagate, regardless of the drive frequency, without experiencing creep motion. As a consequence of this suppression of the creep regime, the distinct high- and low-frequency β values merge (Figure 3.8c). The low-temperature value of β, *i.e.* 0.03 ± 0.002, is the result of creep-free domain dynamics in the critical regime. Since, at present, the understanding of β is based solely on phenomenological studies, more theoretical research on *ac* hysteresis dynamics is important to shed further light on these processes.

To strengthen our predictions, we constructed phase diagrams describing the hysteretic dynamics of our BFO films (Figure 3.8e and 3.8f) from the experimental data, based on the analysis described in Ref. [31]. At room temperature, we define E_N as the E value where the switching current reaches 1% of $J(E_C)$. At low temperature, due to the higher noise level of the switching current, we instead used the P-E hysteresis loops (Figure 3.10), defining E_N as the crossing point of the average lines of P-E hysteresis before and after switching. The E_{cr} values were taken as the E_C value at the frequency at which dynamic crossover occurs; that is, the frequency at which the slope of the E_C- f graph changes.

In Figure 3.8e and 3.8f, red symbols denote experimentally-determined values of E_N, while blue symbols represent values of E_{cr}. *Solid* blue symbols correspond to E_{cr} values in the temperature window where the dynamic crossover exists (*i.e.* the behaviour involves the creep regime), while *open* blue symbols denote hypothetical E_{cr} values in the temperature window where the dynamic crossover does not exist; that is, the creep-free regime. For BFO/LSMO (Figure 3.8f), the creep, flow, and critical regimes are all observed in the phase diagram, consistent with the aforementioned hypotheses. For the BFO/SRO system (Figure 3.8e), however, the values of hypothetical E_{cr} are comparable (within experimental uncertainty) to the values of E_N, implying that the creep regime is supressed, for all considered temperatures. It is important to remember that the mechanism for creep suppression in the two systems is different: for BFO/LSMO at low temperature it is due to the elimination of thermally-activated hopping, while for BFO/SRO it is related to the reduced state of disorder.

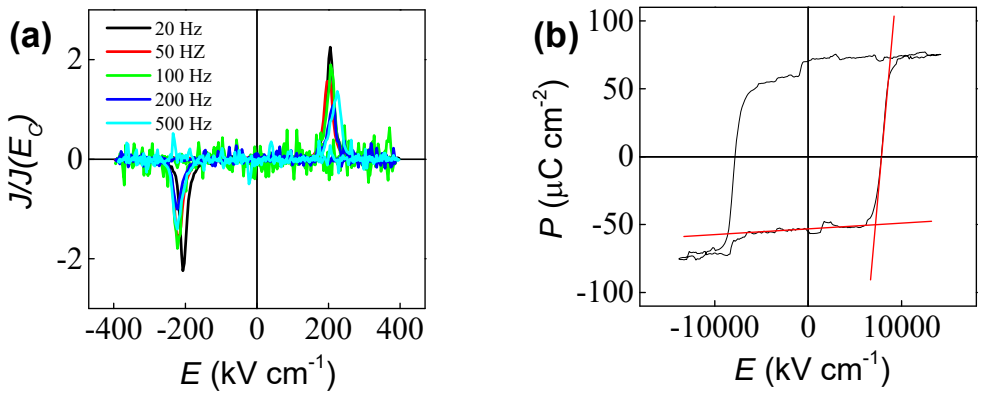

Figure 3.10. (a) The switching current for BFO/LSMO at 20 K. (b) *P*-*E* hysteresis loop of BFO/LSMO at 20 K using 500 Hz of *ac* field.

3.4.3 Origin of different creep dynamics of BFO films

With this detailed understanding of the domain dynamics of the two systems, we now provide an intuitive explanation, at the microscopic level, for our observation of nearly creep-free behaviour. The variation in morphology observed for the SRO and LSMO bottom electrodes (Figure 3.11) is much less pronounced than the BFO surface morphology differences (Figure 3.7a and 3.7b). This observation can be understood in terms of the growth process. Typically, the growth of SRO occurs in the step-flow mode [44], yielding a uniform and atomically-flat SRO surface. LSMO, on the other hand, typically grows in a layer-by-layer mode [45] whereby the atoms are deposited at random positions on the surface. Despite the relatively small difference in surface morphology of the different bottom electrodes, for LSMO the widely-distributed atoms may act as seeds for the subsequent BFO growth, giving rise to an increased dislocation density and surface roughness (Figure 3.7a) of the resulting BFO layer. In ferroelectric thin films, nucleation usually occurs either at the interface or at the surface [27,38,39]; therefore a rougher top surface causes domain nucleation to occur at lower values of applied field, and the corresponding nucleation activation energies will be described by a wider distribution.

The surface roughness may also strongly affect the domain pinning dynamics in our BFO films. A possible origin of domain wall pinning in ferroelectric films is the locally-induced internal electric field. When the BFO film is grown, a structural change (*e.g.* strain relaxation) occurs along the step-terrace edge, generating a locally-induced internal field [24], which can be described by the pinning potential energy landscape $\phi(x)$. Domain wall pinning sites, located at local minima of $\phi(x)$, hinder domain wall motion. Due to the rougher surface

morphology, $\phi(x)$ for BFO/LSMO has a much larger variation and many pinning sites with large energy barriers (solid line in Figure 3.7e). Just after its nucleation, a domain wall is held by a pinning site and its motion is described by thermally-activated creep (dashed line in Figure 3.7e). At higher applied field, flow motion appears (dotted line in Figure 3.7e). In contrast, for the BFO/SRO film, $\phi(x)$ has fewer pinning sites with a smaller variation in their strength (solid line in Figure 3.7f). Consequently, the domain wall experiences flow motion immediately after nucleation, allowing it to have a high propagation velocity (dashed line in Figure 3.7f).

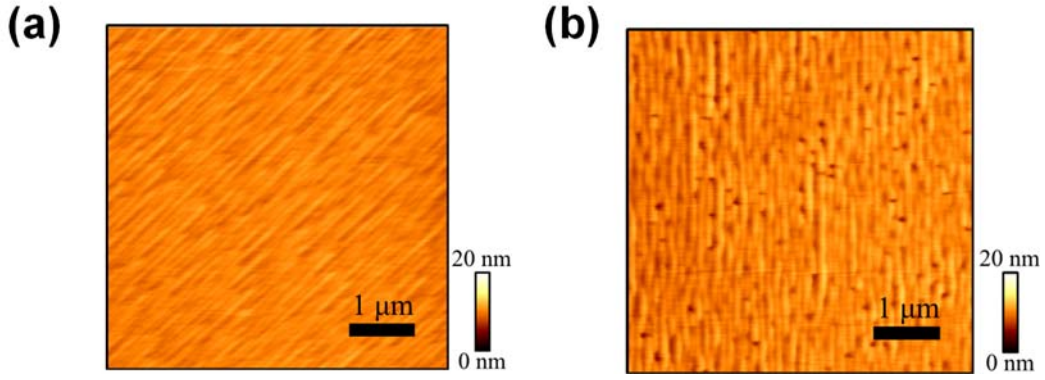

Figure 3.11. The surface morphologies of (a) LSMO and (b) SRO The RMS roughness of (a) and (b) are 0.571 nm, 1.014 nm, respectively.

3.5 Conclusions

Our finding of an almost creep-free regime at room temperature is rather surprising, since most existing reports on epitaxial ferroelectric domain wall dynamics demonstrate the existence of this regime. Our work clearly shows that by carefully controlling the state of disorder, in this case through the properties of the bottom electrode, we can engineer ferroelectric devices with

substantially improved performance. These results are general and this technique can easily be extended to other systems that are governed by the same physical laws, *e.g*. ferromagnetic systems. In addition to fundamental interest of ferroelectric and ferromagnetic switching dynamics, our results present a clear approach for improving device architectures where switching speed is crucial and frequency dependence of the switching process must be avoided; for instance in high-speed actuators or memory devices.

In summary, we have presented a strategy for obtaining creep-free *ac* hysteresis dynamics in epitaxial ferroelectric thin film devices. Through detailed temperature-dependent hysteresis and scanning-probe microscopy-based ferroelectric switching measurements, we revealed that BFO films grown on SRO bottom electrodes exhibit switching dynamics that are markedly different from those displayed by BFO grown on LSMO bottom electrodes. In particular, in the BFO/SRO system, the typically-observed frequency dependence of P-E hysteresis is suppressed, and we find that domain wall propagation velocity is much higher. We attribute this intriguing behaviour to the markedly different morphology of the SRO and LSMO layers, which in turn influences the internal fields and energy landscape in the ferroelectric BFO layer. This work is a clear demonstration that domain dynamics in ferroic systems can be controlled by tuning the nature of disorder.

References

[1] J. H. Jung et al., *ACS Nano* **5**, 10041, (2011).

[2] N. E. Dutoit, B. L. Wardle, S.-G. Kim, *Integr. Ferroelectr.* **71**, 121, (2005).

[3] P. D. Mitcheson, T. C. Green, E. M. Yeatman, A. S. Holmes, *J. Microelectromechanical Syst.* **13**, 429, (2004).

[4] C. Chang, V. H. Tran, J. Wang, Y.-K. Fuh, L. Lin, *Nano Lett.* **10**, 726, (2010).

[5] A. K. Tagantsev, V. O. Sherman, K. F. Astafiev, J. Venkatesh, N. Setter, *J. Electroceramics* **11**, 5, (2003).

[6] C.-H. Lee et al., *Nature* **502**, 532, (2013).

[7] J. F. Scott, C. A. Paz de Araujo, *Science* **246**, 1400, (1989).

[8] R. Guo et al., *Nat Commun* **4**, 1990, (2013).

[9] M. Alexe, C. Harnagea, D. Hesse, U. Gösele, *Appl. Phys. Lett.* **75**, 1793, (1999).

[10] S. S. P. Parkin, M. Hayashi, L. Thomas, *Science* **320**, 190, (2008).

[11] V. Garcia, M. Bibes, *Nat. Commun.* **5**, 4289, (2014).

[12] C. P. Steinmetz, *Am. Inst. Electr. Eng. Trans.* **IX**, 1, (1892).

[13] W. Gerlach, P. Lertes, *Phys. Zeitschrift* **22**, 568, (1921).

[14] G. Blatter, M. V Feigel'man, V. B. Geshkenbein, A. I. Larkin, V. M. Vinokur, *Rev. Mod. Phys.* **66**, 1125, (1994).

[15] L. B. Ioffe, V. M. Vinokur, *J. Phys. C Solid State Phys.* **20**, 6149, (1987).

[16] E. Pinsolle, N. Kirova, V. L. Jacques, A. A. Sinchenko, D. Le Bolloc'h, *Phys. Rev. Lett.* **109**, 256402, (2012).

[17] S. Lemerle et al., *Phys. Rev. Lett.* **80**, 849, (1998).

[18] J. Gorchon et al., *Phys. Rev. Lett.* **113**, 27205, (2014).

[19] K.-J. Kim et al., *Nature* **458**, 740, (2009).

[20] T. Tybell, P. Paruch, T. Giamarchi, J. M. Triscone, *Phys. Rev. Lett.* **89**, 97601, (2002).

[21] J. Y. Jo et al., *Phys. Rev. Lett.* **102**, 45701, (2009).

[22] P. Chauve, T. Giamarchi, P. Le Doussal, *Phys. Rev. B* **62**, 6241, (2000).

[23] W. Kleemann, *Annu. Rev. Mater. Res.* **37**, 415, (2007).

[24] D. Lee et al., *Adv. Mater.* **26**, 5005, (2014).

[25] B. C. Jeon et al., *Adv. Mater.* **25**, 5643, (2013).

[26] A. Gruverman et al., *Appl. Phys. Lett.* **87**, 82902, (2005).

[27] D. J. Kim et al., *Appl. Phys. Lett.* **91**, 132903, (2007).

[28] S. M. Yang et al., *Appl. Phys. Lett.* **92**, 252901, (2008).

[29] Y. Ishibashi, H. Orihara, *Integr. Ferroelectr.* **9**, 57, (1995).

[30] Y. W. So, D. J. Kim, T. W. Noh, J.-G. Yoon, T. K. Song, *Appl. Phys. Lett.* **86**, 92905, (2005).

[31] S. M. Yang et al., *Phys. Rev. B* **82**, 174125, (2010).

[32] L. Wei, C. Zhijun, A. Orlando, *J. Phys. D. Appl. Phys.* **44**, 105404, (2011).

[33] J. F. Scott, *Integr. Ferroelectr.* **12**, 71, (1996).

[34] T.-Z. Liu et al., *Integr. Ferroelectr.* **85**, 31, (2006).

[35] O. Lohse, M. Grossmann, U. Boettger, D. Bolten, R. Waser, *J. Appl. Phys.* **89**, 2332, (2001).

[36] W. J. Hu et al., *Sci. Rep.* **4**, 4772, (2014).

[37] Y. Ishibashi, Y. Takagi, *J. Phys. Soc. Japan* **31**, 506, (1971).

[38] C. T. Nelson et al., *Science* **334**, 968, (2011).

[39] P. Gao et al., *Nat Commun* **2**, 591, (2011).

[40] J. Baek, K. Jong-Hun, S. Shin, J. W. Hong, Z. G. Khim, *Jpn. J. Appl. Phys.* **45**, 2365, (2006).

[41] A. Rajeev, N. Nathaniel, J. S. David, *Nanotechnology* **20**, 445709, (2009).

[42] T. Nattermann, V. Pokrovsky, V. M. Vinokur, *Phys. Rev. Lett.* **87**, 197005, (2001).

[43] J. W. H. S. M Yang H. N. Lee, T. K. Song and Jong-Gul Yoon, *J. Korean Phys. Soc.* **55**, 820, (2009).

[44] W. Hong et al., *Phys. Rev. Lett.* **95**, 95501, (2005).

[45] H. Guo et al., *J. Appl. Phys.* **113**, 234301, (2013).

Chapter 4
Oxygen Partial Pressure during Pulsed Laser Deposition: Deterministic Role on Thermodynamic Stability of Atomic Termination Sequence at $SrRuO_3/BaTiO_3$ Interface

With recent trends on miniaturizing oxide-based devices, the need for atomic-scale control of surface/interface structures by pulsed laser deposition (PLD) has increased. In particular, realizing uniform atomic termination at the surface/interface is highly desirable. However, a lack of understanding on the surface formation mechanism in PLD has limited a deliberate control of surface/interface atomic stacking sequences. Here, taking the prototypical $SrRuO_3/BaTiO_3/SrRuO_3$ (SRO/BTO/SRO) heterostructure as a model system, we investigated the formation of different interfacial termination sequences (BaO-RuO_2 or TiO_2-SrO) with oxygen partial pressure (P_{O2}) during PLD. We found that a uniform SrO-TiO_2 termination sequence at the SRO/BTO interface can be achieved by lowering the P_{O2} to 5 mTorr, regardless of the total background gas pressure (P_{total}), growth mode, or growth rate. Our results indicate that the thermodynamic stability of the BTO surface at the low-energy kinetics stage of PLD can play an important role in surface/interface termination formation. This work paves the way for realizing termination engineering in functional oxide heterostructures.

4.1 Introduction

Perovskite oxide-based heterostructures have been investigated extensively for decades due to the intriguing physical properties and great potential in device application [1–5]. When

reducing the film thickness down to the nanometer scale, the detailed atomic arrangements at surfaces and heterointerfaces become crucial in exploring emergent phenomena and determining various functionalities, including electric transport, magnetism, and ferroelectricity [6–11]. For instance, recent studies on $SrRuO_3/BaTiO_3/SrRuO_3$ (SRO/BTO/SRO) ferroelectric capacitors showed that the atomically sharp and symmetric SRO/BTO interfaces can stabilize the ferroelectricity of BTO down to the theoretical thickness limit [12]. To obtain such atomically sharp interfaces and uniform termination sequences in ABO_3 perovskite-based heterostructures, it is necessary to understand and control the stacking sequence of atomic layers at the half unit-cell level (e.g., AO or BO_2 layer) [9,13,14].

Pulsed laser deposition (PLD) has been considered as one of the most powerful growth techniques for realizing high-quality oxide heterostructures. Owing to high-energy laser ablation, PLD enables effective conveyance of the target material's stoichiometry to the substrate [15,16]. Combined with reflection high-energy electron diffraction (RHEED), PLD can also be used to monitor layer-by-layer growth and realize unit-cell level control of perovskite oxides [17,18]. However, during PLD growth, the expected stacking sequences according to the layer-by-layer growth mode can be distinct from actual atomic arrangements. For instance, during the growth of SRO on a TiO_2-terminated $SrTiO_3$(001) [STO(001)] substrate, reversal of the surface termination from RuO_2 to SrO occurs within a few unit cells due to the highly volatile nature of RuO_2 [19,20]. To achieve the desired termination sequence, the sequential growth of an additional binary oxide monolayer has been used [6,21–23]. However, this method easily induces surface roughening or stacking faults except for a few

constituents (i.e., SrO). Very recently, studies on the growth of manganite and titanate films have shown that the atomic stacking sequences at surfaces/interfaces are strongly dependent on the growth parameters, specifically the background atmosphere during PLD [12,24]. Although these works strongly imply a potential way to realize in situ control of the surface/interface termination sequence, the underlying mechanisms have yet to be resolved.

To elucidate the role of background atmosphere, we break down the PLD processes broadly into three sequential stages [15,16]. i) The laser pulse is absorbed by the target surface and a plasma plume containing the ablated materials is generated. ii) The plume starts to expand and bombard the substrate with ionic species. The plume dynamics is governed by the ionic species with high kinetic energy up to several hundred eV [25]. iii) Nucleation is triggered by supersaturated materials on the substrate and the film starts to grow with the diffusion of adatoms. The kinetic energy of adatoms on the film surface is on the scale of several eV [16,26]. The background atmosphere can strongly affect stages ii) and iii), which are denoted as high- and low-energy kinetics stages, respectively.

In the high-energy kinetics stage, background gas can affect the film stoichiometry because the detailed scattering of each cation depends strongly on the gas composition and pressure [27–30]. In addition, the background gas can significantly reduce the kinetic energy of ionic species arriving at the substrate by one or two orders of magnitude [26]. Thus, it can affect the density and shape of nucleation sites as well as the growth rate [27,31]. During the low-energy kinetics stage, the adatoms lose their kinetic energies until covalent bonds form. Surface structuring is affected significantly by the energy landscape of the film surface. The

background atmosphere can act as an important thermodynamic parameter to determine the surface energy landscape and thus the ultimate surface structure [32]. Therefore, understanding the role of the growth parameters at each PLD stage is of particular importance in controlling the ultimate surface/interface termination sequence.

In this Chapter, using the SRO/BTO/SRO heterostructure as a model system, we investigated the evolution of an interfacial termination sequence with oxygen partial pressure (P_{O2}) during PLD. The interfacial termination sequence in SRO/BTO/SRO heterostructures is sensitive to the growth atmosphere and is crucial for stabilizing the ferroelectricity of BTO [12,33,34]. To elucidate the mechanism of termination sequence variation with P_{O2}, we monitored the growth of a BTO layer under background atmospheres with different gas compositions. Systematic structural characterizations on the as-grown films were performed; the results showed that the termination sequence at the SRO/BTO interface is determined by P_{O2} only, regardless of total background gas pressure (P_{total}), growth mode, or growth rate. Density functional theory (DFT) calculations and phenomenological modeling indicated that the thermodynamic stability of the BTO surfaces (i.e., BaO- or TiO_2-terminated surface) during the low-energy kinetics stage is highly dependent on P_{O2}. Based on the results, we suggest that the difference in the thermodynamic surface stabilities is the main driving force of the P_{O2}-dependent termination sequence at the SRO/BTO interface.

4.2 Experiments

4.2.1 Sample preparations

All of the $SrRuO_3/BaTiO_3/SrRuO_3$ (SRO/BTO/SRO) heterostructures were fabricated using pulsed laser deposition (PLD) with a KrF excimer laser (248 nm, COMPex pro, Coherent). Prior to deposition, $SrTiO_3$ (001) [STO(001)] substrates with low-angle-miscut (0.05–0.1°) were etched by buffered hydrofluoric acid and annealed at 1100 °C for 1 hour in air. This procedure allows the STO substrates to have an atomically smooth TiO_2-terminated surface with 1-unit cell (u.c.)-high terraces. During the deposition process, the substrate temperature was maintained at 1000 K and the laser fluence was set as 1.5 J/cm^2. The repetition rates of the laser were 3 Hz for SRO and 2 Hz for BTO. The SRO top and bottom electrodes were grown under pure oxygen atmosphere, with a partial pressure (P_{O2}) equal to 100 mTorr. The thickness of the electrodes was fixed at 20 nm for all samples used in the paper. During the entire PLD procedure, the surface of the film was monitored by reflection high-energy electron diffraction (RHEED). After deposition, the heterostructures were cooled at 20°C/min under P_{O2} = 100 mTorr.

4.2.2 AFM and XRD measurements

The surface topographies of SRO/BTO/SRO heterostructures were investigated by atomic force microscopy (AFM, Asylum Cypher) in the non-contact tapping mode with a non-conductive tip (Nano Sensors). To determine the crystal structure of the SRO/BTO/SRO films,

we performed X-ray diffraction (XRD) 2θ-ω scans using a commercial high-resolution X-ray diffractometer (Bruker AXS D8 with a Vantec line-detector) and Huber six-circle diffractometer at Sector 9C of the Pohang light source.

4.2.3 Atomic structure measurements

The structure of the samples was investigated at the atomic scale via scanning transmission electron microscopy (STEM, JEM-ARM200F, JEOL) and coherent Bragg rod analysis (COBRA, Pohang Light Source). During STEM measurements, we obtained multiple cross-sectional high-angle annular dark field (HAADF) images of each sample. Note that all of the images were viewed along the [001] zone axis.

4.2.4 DFT calculations

Density functional theory (DFT) calculations were performed using the Vienna Ab-initio Simulation Package (VASP). We constructed the supercell by stacking 4-u.c. BTO on top of 6-u.c. SRO. The BTO cell contains four TiO_2 layers and three (four) BaO layers for the TiO_2-terminated (BaO-terminated) surface [35,36]. Between the periodic slabs, 20 Å of vacuum was stacked along the [001] direction to prevent artificial interactions. To simplify the calculations, we neglected the ferroelectricity of BTO and considered the TiO_2- and BaO-terminated (1 × 1) bulk-like BTO surface only. The exchange-correlation function of the generalized gradient approximation (GGA) with the on-site U (GGA+U) approach was utilized based on the Perdew–Burke–Ernzerhof (PBE) scheme [37,38]. For mimicking the

magnetic and electronic properties of the itinerant ferromagnetic $SrRuO_3$ metal, an effective U ($U_{eff} = U\text{-}J$) value of 1.0 eV for the d orbital was chosen, which is consistent with other relevant DFT calculations [39]. Projector augmented-wave (PAW) pseudopotentials [40] were used along with a plane-wave basis set, with a kinetic energy cut-off of 400 eV and a 4 × 4 × 1 **k**-point mesh. Using the DFT calculations together with a phenomenological model based on the thermodynamic framework, we can determine the Gibbs free energy of BTO surfaces and their relative stabilities. The important parameters from DFT calculations and detailed methodology of phenomenological modeling will be described in Chapter 4.4.2.

4.3 Results

4.3.1 Basic characterization of SRO/BTO/SRO heterostructures

All of the SRO/BTO/SRO heterostructures studied herein were grown *via* PLD on atomically smooth TiO_2-terminated STO(001) substrates [12,41]. During the deposition process, the substrate temperature was maintained at 1000 K. The SRO top and bottom electrodes were grown under pure oxygen atmosphere with P_{O2} = 100 mTorr. The BTO layers were grown under various background atmospheres. Here, we present the results from three representative cases: 1) a pure oxygen atmosphere with $P_{total} = P_{O2}$ = 5 mTorr, 2) a pure oxygen atmosphere with $P_{total} = P_{O2}$ = 150 mTorr, and 3) an argon and oxygen (O_2/Ar) mixed atmosphere with P_{O2} = 5 mTorr and P_{total} = 150 mTorr.

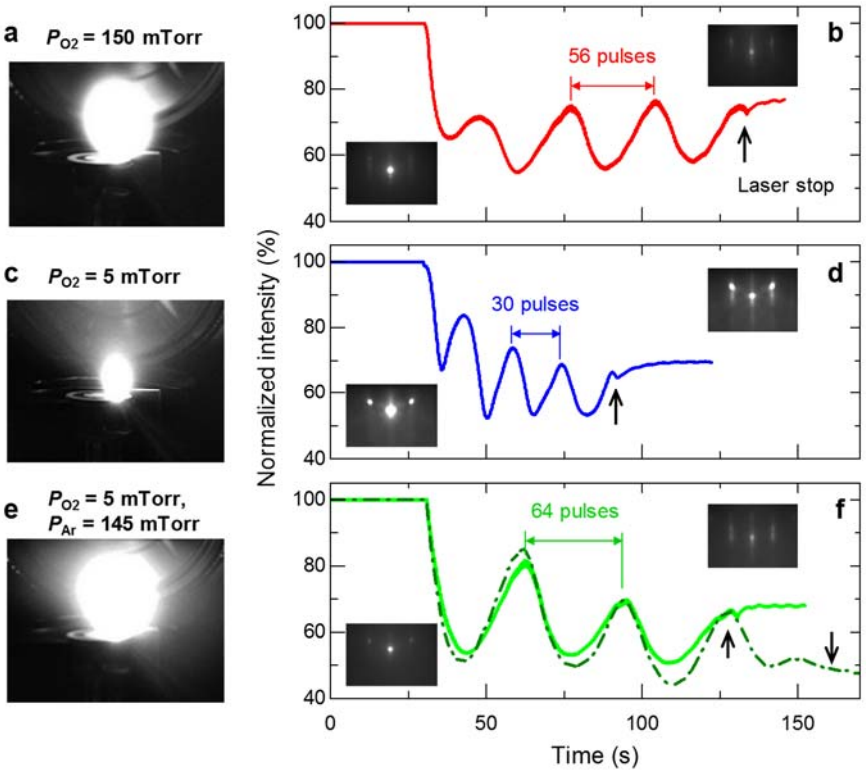

Figure 4.1. In situ monitoring of the growth of $BaTiO_3$ (BTO) layers. (a,c,e) Photographic images of the laser-ablated plume during BTO growth under (a) $P_{total} = P_{O2} = 150$ mTorr, (c) $P_{total} = P_{O2} = 5$ mTorr, and (e) O_2/Ar mixed atmosphere ($P_{total} = 150$ mTorr and $P_{O2} = 5$ mTorr). (b,d,f) Time-dependent reflection high-energy electron diffraction (RHEED) intensity profile of the specular spot during BTO growth under (b) $P_{O2} = 150$ mTorr, (d) $P_{O2} = 5$ mTorr, and (f) O_2/Ar mixed atmosphere. Note that the solid line in (f) indicates the clear layer-by-layer growth up to three oscillations while dashed line shows the intensity decay with further growth. The insets in (b), (d), and (f) indicate the RHEED diffraction patterns before and after BTO growth. The open arrows indicate the timing to stop laser pulses.

Figure 4.1 shows the photographic images of a laser-ablated plume and a time-dependent intensity profile of an RHEED specular spot during BTO growth. For the samples grown at P_{O2} = 150 and 5 mTorr, the intensity profiles clearly exhibit four oscillations, indicating standard layer-by-layer growth (Figure 1b,d, respectively). For the sample grown in an O_2/Ar mixed atmosphere, the layer-by-layer growth persisted up three oscillations of RHEED intensity (solid line in Figure 1f). With further growth, the RHEED intensity decreased significantly (dashed line in Figure 1f). This behavior implies a growth mode transition from layer-by-layer growth to Stranski–Krastinov type (layer-plus-island) growth [42].

The high epitaxial quality of the SRO/BTO/SRO heterostructures was confirmed *via* atomic force microscopy (AFM) and X-ray diffraction (XRD). Figure 4.2a–c shows AFM topographic images of SRO/BTO/SRO heterostructures grown under the three background atmospheres. Please note that to avoid possible step-bunching of SRO layer, we intentionally choose the STO(001) substrates with terraces larger than 300 nm. Even though the larger step-width caused meandering of step-edge by coalescence of 2D islands with advancing steps during SRO grwoths [43], all of the samples exhibited atomically flat surfaces with uniform 1-unit cell (u.c.)-high terraces [19,43,44]. The XRD 2θ-ω scans shown in Figure 4.2d are almost identical. The observed high-intensity SRO(220) peaks and clear Laue fringes signify sharp heterointerfaces. Note that the {00*l*} peaks from the ultrathin BTO layers were too weak to be detected by XRD.

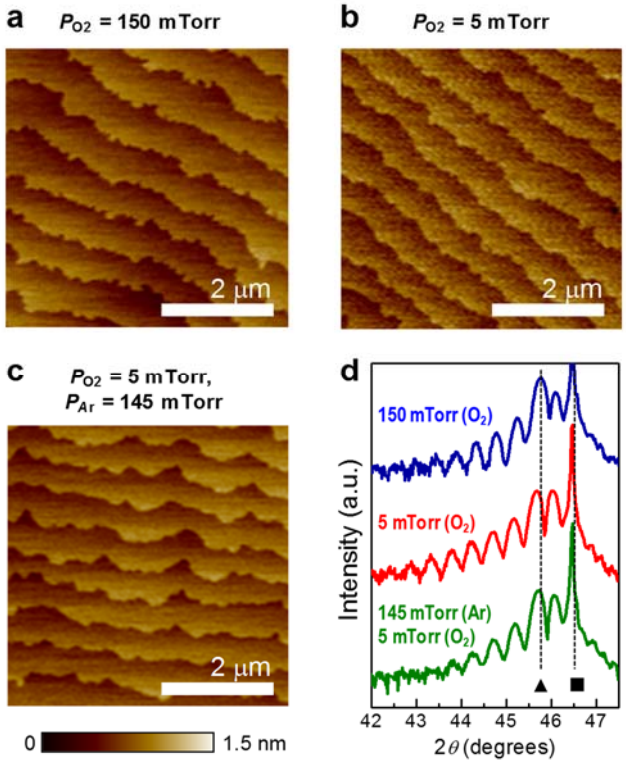

Figure 4.2. Structural characterizations of the $SrRuO_3$ (SRO)/BTO/SRO heterostructures. (a-c) Atomic force microscopy (AFM) images of the SRO/BTO/SRO heterostructures with few-unit cells (u.c.)-thick BTO layer deposited at (a) P_{O2} = 150 mTorr, (b) P_{O2} = 5 mTorr, and (c) O_2/Ar mixed atmosphere. d) X-ray diffraction (XRD) 2θ-ω scans of the SRO/BTO/SRO heterostructures. The peak positions of SRO(220) and $SrTiO_3$(002) [STO(002)] peaks are labeled by solid triangles and squares, respectively.

4.3.2 Atomic structure of SRO/BTO/SRO heterostructures

Despite nearly identical features in macroscopic structural characterizations, scanning transmission electron microscopy (STEM) results revealed distinct interfacial termination sequences in SRO/BTO/SRO heterostructures, depending on the background atmosphere. Figure 3a shows a high-angle annular dark field (HAADF) image measured from the BTO sample grown under P_{O2} = 150 mTorr; the bottom BTO/SRO interface exhibited a uniform TiO_2-SrO termination sequence, while the top SRO/BTO interface showed a rather complicated structure. Figure 4.3b shows the magnified HAADF image and intensity line profiles from a preselected region (marked as a dashed box in Figure 3a); the right side of the image exhibits four TiO_2 layers and three BaO layers, implying BTO thickness of 3.5 u.c.. On the left side of the image, the topmost TiO_2 layer is gradually converted into a RuO_2 layer, reducing BTO thickness to 3 u.c. (Figure 4.3a). This result demonstrates heterogeneous terminations with both SrO-TiO_2 and BaO-RuO_2 sequences at the top SRO/BTO interface, as shown in Figure 3c. In contrast, for the sample grown at P_{O2} = 5 mTorr, the HAADF images (Figure 4.3d,e) showed uniform SrO-TiO_2 termination sequences for both the bottom and the top SRO/BTO interfaces (Figure 4.3f). The uniformity of the termination sequence was confirmed by surface X-ray scattering experiments [12].

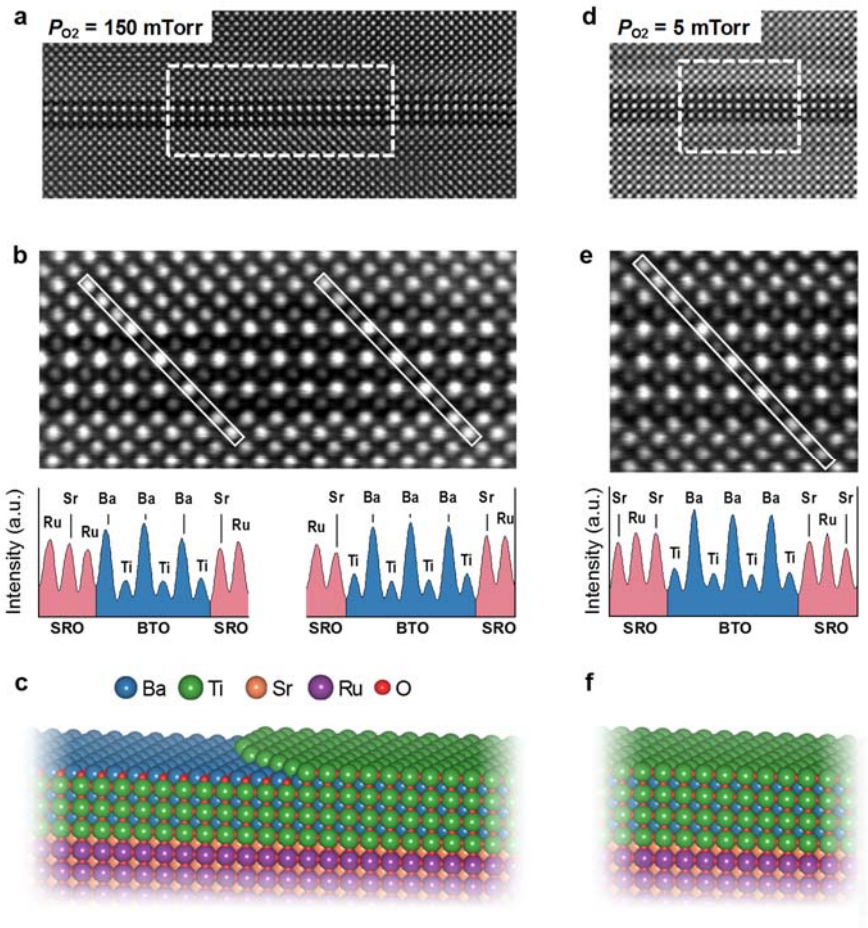

Figure 4.3. Interfacial structure of SRO/BTO/SRO heterostructures with BTO grown under pure oxygen atmospheres. (a) [(d)] High-angle annular dark field (HAADF) images of the SRO/BTO/SRO heterostructure with a BTO layer grown at P_{O2} = 150 mTorr (5 mTorr). (b) [(e)] Magnified HAADF images of the pre-scanned area marked by the dashed box in (a) [(d)]. The HAADF intensity profiles along the solid boxes marked in (b) [(e)] are also shown. (c) [(f)] Schematic illustration of the BTO surface after the growth at P_{O2} = 150 mTorr (5 mTorr). After BTO growth at P_{O2} = 150 mTorr, the film surface (i.e., SRO/BTO interface) shows a heterogeneous termination sequence. In contrast, the as-grown BTO at P_{O2} = 5 mTorr film surface shows a uniform SrO-TiO_2 termination sequence.

To clarify the P_{O2}-dependent interfacial termination sequences further, we grew BTO samples under an O_2/Ar mixed atmosphere and performed STEM measurements (fixed P_{total} = 150 mTorr but lower P_{O2} = 5 mTorr). The BTO sample grown up to three RHEED oscillations showed a uniform TiO_2-SrO termination sequence at both the top and the bottom SRO-BTO interfaces, as shown in Figure 4.4a–c. This symmetric interfacial termination was the same as that of the sample grown in pure P_{O2} = 5 mTorr. For the samples with further BTO growth, as shown in Figure 4.4d–f, islands 1 u.c. in height appeared at the top interface, leading to a local thickness variation of 1 u.c. This spatial structural inhomogeneity was consistent with the decay evident in the RHEED intensity profile shown in Figure 4.1f. Despite these differences in interface structure, both the thinner (2.5 u.c.) and the thicker (3.5 u.c.) regions exhibited a symmetric, uniform TiO_2-SrO termination sequence. The heterogeneous termination structure was absent throughout the entire sample. Accordingly, the STEM results strongly suggest that the interfacial termination sequence is determined by P_{O2} rather than P_{total}.

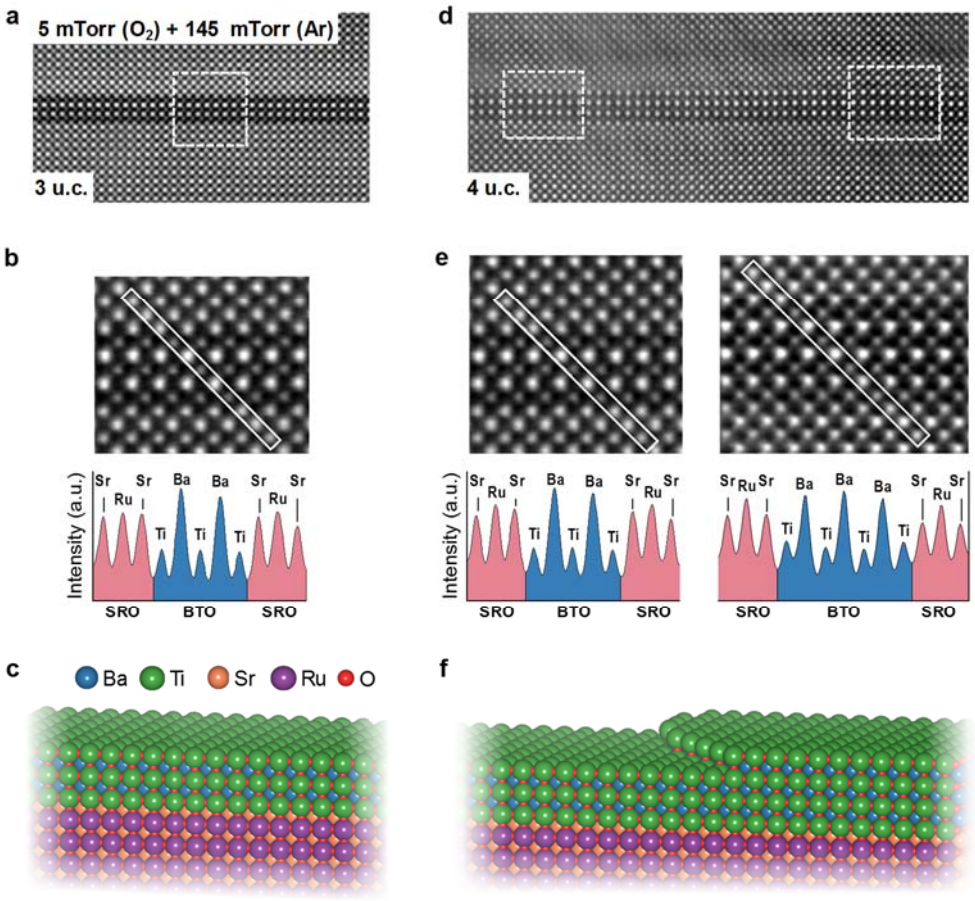

Figure 4.4. Interfacial structure of SRO/BTO/SRO heterostructures with BTO grown under pure oxygen atmospheres. (a) [(d)] High-angle annular dark field (HAADF) images of the SRO/BTO/SRO heterostructure with a BTO layer grown at P_{O2} = 150 mTorr (5 mTorr). (b) [(e)] Magnified HAADF images of the pre-scanned area marked by the dashed box in (a) [(d)]. The HAADF intensity profiles along the solid boxes marked in (b) [(e)] are also shown. (c) [(f)] Schematic illustration of the BTO surface after the growth at P_{O2} = 150 mTorr (5 mTorr). After BTO growth at P_{O2} = 150 mTorr, the film surface (i.e., SRO/BTO interface) shows a heterogeneous termination sequence. In contrast, the as-grown BTO at P_{O2} = 5 mTorr film surface shows a uniform SrO-TiO_2 termination sequence.

4.4 Discussions

4.4.1 Effect of plume dynamics variation on interface atomic structure

The observed interfacial termination sequences at the top SRO/BTO interface were inconsistent with the stacking sequence of BTO with the layer-by-layer growth scheme. The as-grown SRO bottom electrode has a uniformly SrO-terminated surface due to the highly volatile nature of the RuO_2 layer [19]. Accordingly, the unit-cell-by-unit-cell stacked BTO should have a BaO-terminated surface. The resultant top SRO/BTO interface was expected to show a uniform RuO_2-BaO termination sequence, which has never been observed in our samples. In addition, the number of BaO and TiO_2 layers observed in HAADF images were not same with that predicted by intensity profiles of RHEED specular spot. On this basis, we suggest that altering P_{O2} could trigger atomic-scale structural modulations, such as selective decomposition of BaO or TiO_2 layer, on the BTO surface during growth, thus leading to changes in the termination sequence. The atomic-scale structural modulations can be triggered by either plume dynamics variation during the high-energy kinetics stage or changes in surface structuring during the low-energy kinetics stage. In the following part of this paper, we attempt to resolve the effects of varying P_{O2} in terms of these PLD stages.

The changes in plasma plume dynamics with background atmosphere during the high-energy kinetics stage can be clearly manifested by the RHEED results in Figure 1. During the growth of the BTO sample under a pure oxygen atmosphere, the laser-ablated plume with P_{O2} = 150 mTorr (Figure 1a) was larger and brighter than that with P_{O2} = 5 mTorr (Figure 4.1c),

implying a stronger interaction with the background atmosphere [16]. Moreover, because the high-pressure environment slows down the high energetic ions inside the plume, the growth rate in the P_{O2} = 150 mTorr case (Figure 4.1b) was also lower than that in the P_{O2} = 5 mTorr case (Figure 4.1d). To differentiate the effects of P_{O2} from those of P_{total}, we also monitored the growth under an O_2/Ar mixed atmosphere, of which P_{total} = 150 mTorr while P_{O2} = 5 mTorr. As shown in Figure 4.1e,f, both the plume characteristics (Figure 4.1e) and the growth rate (Figure 4.1f) under the O_2/Ar mixed atmosphere were similar to those in the P_{O2} = 150 mTorr case, implying similar plume dynamics. Comparing the RHEED results in the three cases, the plume dynamics were mainly determined by P_{total} rather than P_{O2}. Nevertheless, STEM results demonstrated that the interfacial termination sequence is determined by P_{O2} only. On this basis, we assert that the plume dynamics-related structural changes cannot explain the different termination sequences at the top SRO/BTO interfaces.

We also confirmed that the variation in chemical stoichiometry, which could also be sensitive to plume dynamics, cannot explain the P_{O2}-dependent termination sequences. We investigated the cation stoichiometry of BTO films by STEM-based energy-dispersive spectroscopy (EDS). Figure 4.5a shows a Ti/Ba cation ratio of 20-nm-thick BTO films grown under pure oxygen atmosphere with various P_{O2}, as well as in an O_2/Ar mixed atmosphere. For all of the films, the Ba/Ti ratios were nearly identical within the experimental error. We also investigated the oxygen stoichiometry by selected-area electron energy-loss spectroscopy (EELS).[13,45] Figure 4.5b shows an HAADF image of a SRO/BTO/SRO/STO(001) heterostructure grown at P_{O2} = 5 mTorr. The EELS values at Ti-L and O-K core edges were

measured from preselected areas in the 2.5-u.c. BTO layer and the STO substrate (open circles in Figure 5b). In Figure 4.5c, the EELS curves of BTO at the Ti-L (O-K) core edge exhibited four (three) well-defined peaks. The shapes and positions of these peaks were close to those of the stoichiometric STO substrate.[45] This implies that the oxygen deficiency was minimized, even for our sample grown at lower P_{O2} = 5 mTorr [13,45]. Within the resolution of our experimental set-up, the chemical stoichiometry variation of the BTO layer was negligible and did not contribute to the observed interface structural variations.

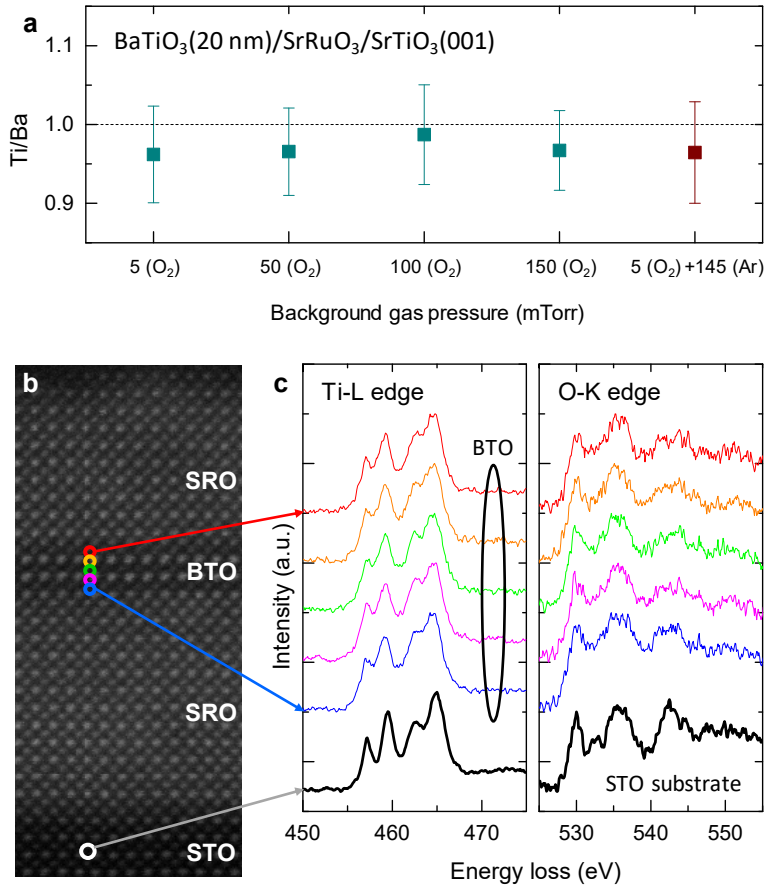

Figure 4.5. Characterization of the chemical stoichiometry of BTO films. (a) The cation Ti/Ba ratio of BTO films grown at different background atmospheres measured by energy-dispersive spectroscopy (EDS). The error bars indicate the standard deviations of Ti/Ba ratio measured from 20 locations randomly selected from one BTO sample. (b) HAADF images of the SRO/BTO/SRO heterostructure, in which the 2.5-u.c.-thick BTO layer was grown at P_{O2} = 5 mTorr. (c) Electron energy-loss spectroscopy (EELS) at Ti-L and O-K edges measured from BTO layer and STO(001) substrate. The electron spot position is marked by the open circles and solid arrows in (b).

4.4.2 Different thermodynamic energies of BaO- and TiO_2-terminated BTO surfaces

Based on the above results and discussions, we suggest that the termination sequence variation at the SRO/BTO top interface occurs during the low-energy kinetics stage. During this stage, the surface structuring is accompanied by the kinetic energy loss of adatoms and the formation of covalent bonds. Depending on the chemical composition and bonding nature, the atomic structure of the film surface can have a complicated phase diagram [35,36]. Initially, the kinetic energy of adatoms is much higher than the energy barriers among different surface structures. Hence, after the adatoms lose kinetic energy, the ultimately formed surface structure should be the one with highest thermodynamic stability. The thermodynamic stability of the BTO surface can be described by the surface Gibbs free energy [35,36]. In the following part, we attempt to determine the Gibbs free energies of possible BTO surface structures via a phenomenological model based on a thermodynamic framework, together with DFT calculations.

The evolution of $BaTiO_3$ (BTO) surface stability can be described in terms of the surface Gibbs free energy for different surface structures and background atmospheres [35,36]. The surface Gibbs free energy of the *i*-th termination of BTO (Ω^i) can be written as

$$\Omega^i = \Delta E^i - n_{\mathrm{Ba}}\mu_{\mathrm{Ba}} - n_{\mathrm{Ti}}\mu_{\mathrm{Ti}} - n_{\mathrm{O}}\mu_{\mathrm{O}} \,, \tag{4.1}$$

where ΔE^i is the relative total energy of the heterostructure surface except for the fixed region that limits atomic relaxation as a bulk-like region per surface area; n_{Ba}, n_{Ti}, and n_{O} denote the numbers of Ba, Ti, and O atoms in the surface per surface area,

respectively; and μ_{Ba}, μ_{Ti}, and μ_{O} are their corresponding chemical potentials, respectively. For convenience, we measured the chemical potentials for each species with respect to their standard states at 0 K, for example, $\Delta\mu_a = \mu_a - E_a^{\mathrm{std}}$. The reference state for oxygen is O_2 gas, such that $E_{\mathrm{O}}^{\mathrm{std}} = E_{\mathrm{O}_2}^{\mathrm{gas}}/2$. The reference states for cations are their respective bulk elemental phases. In addition, we can impose constraints on the chemical potentials of each atom species and the formation energy of bulk BTO, $\Delta G_f(\mathrm{BTO})$:

$$\Delta\mu_{\mathrm{Ba}} + \Delta\mu_{\mathrm{Ti}} + 3\Delta\mu_{\mathrm{O}} = \Delta G_f(\mathrm{BTO}) \quad . \tag{4.2}$$

If we combine Equation 4.1 and 4.2, we can express Ω^i with the chemical potentials of Ba and O as variable:

$$\Omega^i = \phi^i + \Gamma_{\mathrm{Ba}}^i \Delta\mu_{\mathrm{Ba}} + \Gamma_{\mathrm{O}}^i \Delta\mu_{\mathrm{O}} \quad , \tag{4.3}$$

where $\phi^i = \Delta E^i - n_{\mathrm{Ti}} E_{BTO}^{\mathrm{bulk}} + \Gamma_{\mathrm{O}} E_{\mathrm{O}}^{\mathrm{gas}}/2 \; + \Gamma_{\mathrm{Ba}} E_{\mathrm{Ba}}^{\mathrm{bulk}}$, $\Gamma_{\mathrm{Ba}} = -(n_{\mathrm{Ba}} - n_{\mathrm{Ti}})$, and $\Gamma_{\mathrm{O}} = -(n_{\mathrm{O}} - 3n_{\mathrm{Ti}})$. Note that all of these coefficients are intrinsic properties for each termination and independent of chemical environment. With the simple assumption of bulk-like (1 × 1) surface termination, the surface Gibbs free energies of the TiO_2- and BaO-terminated BTO surfaces can be written simply as

$$\Omega^{\mathrm{TiO_2}} = \phi^{\mathrm{TiO_2}} + \Delta\mu_{\mathrm{Ba}} + \Delta\mu_{\mathrm{O}} \quad \text{and} \tag{4.4a}$$

$$\Omega^{\mathrm{BaO}} = \phi^{\mathrm{BaO}} - \Delta\mu_{\mathrm{Ba}} - \Delta\mu_{\mathrm{O}} \quad , \tag{4.4b}$$

respectively. Equation 4.4a and 4.4b demonstrate that decreasing $\Delta\mu_{\mathrm{O}}$ monotonically decreases the surface energy difference $\Omega^{\mathrm{TiO_2}} - \Omega^{\mathrm{BaO}}$, making the TiO_2-terminated BTO surface more stable. For quantitative investigations of the relative BTO surface Gibbs energy,

we summarize the important thermodynamic parameters from our DFT calculations and previous experiments in Table 4.1.

From Equation 4.4a and 4.4b, we now know that the surface energy difference between these two surface structures $\Delta\Omega$ is given by:

$$\Delta\Omega = \Omega^{TiO_2} - \Omega^{BaO} = \phi^{TiO_2} - \phi^{BaO} + 2\Delta\mu_{Ba} + 2\Delta\mu_{O} \quad , \tag{4.5}$$

where the constants ϕ^{TiO_2} and ϕ^{BaO} are determined by the intrinsic structural and electronic properties of TiO_2 and BaO-terminated surfaces. We can obtain $\phi^{TiO_2} - \phi^{BaO}$ = 6.37 eV from DFT calculations (Table 4.1). $\Delta\mu_O$ and $\Delta\mu_{Ba}$ are chemical potentials for each species with respect to their standard states at 0 K. $\Delta\mu_O$ is correlated with P_{O2} according to the ideal gas relationship:

$$\Delta\mu_O(T, P_{O2}) = (E_{O_2}^{gas} + \Delta\mu_{O_2}(T,\ P_{O2}) + k_B T ln(\ P_{O2}/P_0))/2 \quad , \tag{4.6}$$

where $T(T_0)$ is the temperature (enthalpy reference temperature, T_0 = 298.15 K), P_0 is the standard state pressure (760 mTorr), $E_{O_2}^{gas}$ is the total energy of the O_2 molecule, and $\Delta\mu_{O_2}(T,\ P_{O2})$ is the change in the oxygen chemical potential from the temperature-dependent enthalpy and entropy of the O_2 molecule [46]. $\Delta\mu_{Ba}$ is the only unknown parameter in Eqation 4.5. When P_{O2} = 150 mTorr, the BTO surface exhibited mixed TiO_2 and BaO terminations, which indicates that the levels of thermodynamic stability of these two surfaces are similar. On this basis, we estimated $\Delta\mu_{Ba} = -5.2$ eV to satisfy $\Delta\Omega$ = 0 at P_{O2} = 150 mTorr.

From Equation 4.5 and 4.6, we can construct the relationship between P_{O2} and $\Delta\Omega$. Figure 4.6 clearly shows a linear relationship between log(P_{O2}) and $\Delta\Omega$ at T = 1000 K. By

reducing P_{O2}, $\Delta\Omega$ decreased monotonically, which made the TiO_2-terminated surface more stable. When P_{O2} reached 5 mTorr, $\Delta\Omega$ decreased to −280 meV. The magnitude of this value is much larger than the thermal energy at the growth temperature (1000 K, corresponds to approximately 86 meV). Therefore, under a pure oxygen atmosphere of P_{O2} = 5 mTorr, once the TiO_2-terminated BTO surface forms, it can be stabilized uniformly. For the O_2/Ar mixed atmosphere with the same P_{O2}, the additional Ar gas can significantly change the plume dynamics but preserve the surface stability due to its negligible reactivity. As a result, the top SRO/BTO interface, although exhibiting island characteristics, still exhibited a uniform SrO-TiO_2 termination sequence. At higher P_{O2} near 150 mTorr, the magnitude of $\Delta\Omega$ became smaller than the thermal energy, leading to a mixed surface termination. Note that stabilizing a uniform BaO-terminated surface requires a high P_{O2} over 300 mTorr, which is not possible for obtaining high-quality BTO films.

	Values	Note
E_{Ba}^{bulk}	−1.87 eV	GGA-PBE
$E_{O_2}^{gas}/2$	−4.71 eV	Exp.
E_{BTO}^{bulk}	−11.81 eV	GGA-PBE
$\phi^{TiO_2} - \phi^{BaO}$	6.73 eV	GGA-PBE & Exp.

Table 4.1. Thermodynamic parameters for obtaining the relative surface Gibbs free energy of BTO. The values are obtained from the generalized gradient approximation (GGA) with the on-site *U* Perdew–Burke–Ernzerhof (PBE) scheme and from the published thermodynamic data [46] at room temperature.

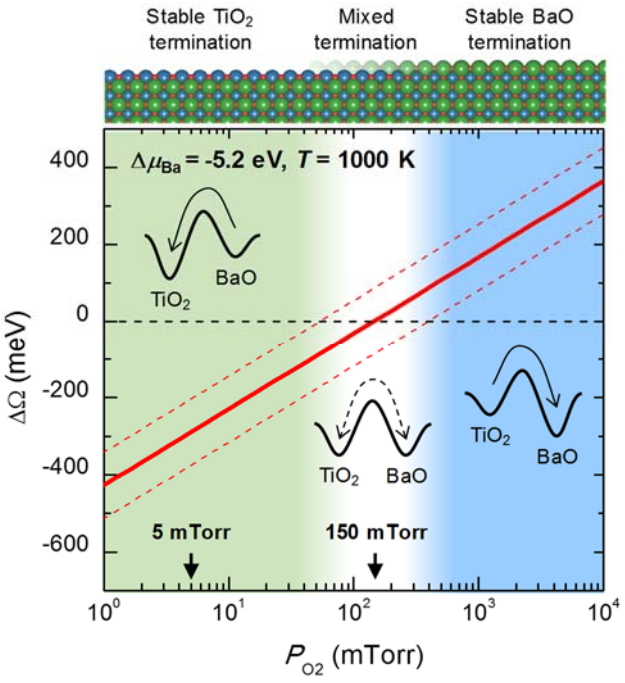

Figure 4.6. P_{O2}-dependent surface energy differences between TiO_2-terminated and BaO-terminated BTO ($\Delta\Omega = \Omega^{TiO2} - \Omega^{BaO}$). We set $\Delta\mu_{Ba} = -5.2$ eV and $T = 1000$ K. The dashed lines indicate the offset of $\Delta\Omega$ induced by the thermal energy at 1000 K (86 meV). The inset schematic diagram describes the possible energy landscapes of BTO surface structures (i.e., TiO_2 and BaO terminations), which evolve with P_{O2}. The arrows indicate the trend of stabilizing the specific surface structure.

4.5 Conclusions

In summary, we revealed the deterministic role of P_{O2} on the interfacial termination sequences in SRO/BTO/SRO heterostructures grown by PLD. Uniform SrO-TiO_2 interfacial termination

was achieved by lowering the P_{O2} to 5 mTorr. This effective termination control was driven by the different thermodynamic stabilities of TiO_2- and BaO-terminated surfaces, which evolve significantly with P_{O2}. Our work highlights the roles of the low-energy kinetics stage of PLD and thermodynamic parameters in the interface/surface structures of as-grown films, which has been largely overlooked. This scenario could be generalized to other oxide heterostructures for deliberately controlling the atomic structure of the interface, leading to the development and implementation of oxide-based electronic devices.

References

[1] J. Heber, *Nature* **459**, 28, (2009).

[2] J. Chakhalian, A. J. Millis, J. Rondinelli, *Nat. Mater.* **11**, 92, (2012).

[3] J. Mannhart, D. G. Schlom, *Science* **327**, 1607, (2010).

[4] H. Y. Hwang et al., *Nat. Mater.* **11**, 103, (2012).

[5] P. Zubko, S. Gariglio, M. Gabay, P. Ghosez, J.-M. Triscone, *Annu. Rev. Condens. Matter Phys.* **2**, 141, (2011).

[6] A. Ohtomo, H. Y. Hwang, *Nature* **427**, 423, (2004).

[7] N. Reyren et al., *Science* **317**, 1196, (2007).

[8] H. Yamada et al., *Science* **305**, 646, (2004).

[9] P. Yu et al., *Proc. Natl. Acad. Sci. U. S. A.* **109**, 9710, (2012).

[10] D. Mukherjee et al., *ACS Appl. Mater. Interfaces* **5**, 7450, (2013).

[11] Z. Xi et al., *Nat. Commun.* **8**, 15217, (2017).

[12] Y. J. Shin et al., *Adv. Mater.* **29**, 1602795, (2017).

[13] N. Nakagawa, H. Y. Hwang, D. A. Muller, *Nat. Mater.* **5**, 204, (2006).

[14] R. Guo et al., *Adv. Mater. Interfaces* **3**, 1, (2016).

[15] G. K. Hubler, D. B. Chrisey, (1994).

[16] Robert Eason, *Pulsed Laser Deposition of Thin Films* (John Wiley & Sons, Inc., Hoboken, NJ, USA, 2006).

[17] A. Ichimiya, P. I. Cohen, *Reflection High-Energy Electron Diffraction* (Cambridge University Press, Cambridge, 2004).

[18] S. Gerhold, M. Riva, B. Yildiz, M. Schmid, U. Diebold, *Surf. Sci.* **651**, 76, (2016).

[19] G. Rijnders, D. H. A. Blank, J. Choi, C.-B. Eom, *Appl. Phys. Lett.* **84**, 505, (2004).

[20] Y. J. Chang, S. Phark, *ACS Nano* **10**, 5383, (2016).

[21] H. Yamada et al., *Adv. Funct. Mater.* **25**, 2708, (2015).

[22] R. Takahashi et al., *J. Cryst. Growth* **234**, 505, (2002).

[23] T. Ohnishi, M. Yoshimoto, G. H. Lee, T. Maeda, H. Koinuma, *J. Vac. Sci. Technol., A* **15**, 2469, (1997).

[24] A. Tselev et al., *ACS Nano* **9**, 4316, (2015).

[25] S. A. Chambers, *Adv. Mater.* **22**, 219, (2010).

[26] H. N. Lee, S. S. Ambrose Seo, W. S. Choi, C. M. Rouleau, *Sci. Rep.* **6**, 19941, (2016).

[27] A. Bailini, P. M. Ossi, *Appl. Surf. Sci.* **252**, 4364, (2006).

[28] J. Gonzalo, C. N. Afonso, I. Madariaga, *J. Appl. Phys.* **81**, 951, (1997).

[29] A. P. Chen et al., *J. Appl. Phys.* **114**, 124101, (2013).

[30] J. Gonzalo, R. Gómez San Román, J. Perrière, C. N. Afonso, R. Pérez Casero, *Appl. Phys. A Mater. Sci. Process.* **66**, 487, (1998).

[31] Z. Zhu, X. J. Zheng, W. Li, *J. Appl. Phys.* **106**, 54105, (2009).

[32] H. Guo et al., *J. Appl. Phys.* **113**, 234301, (2013).

[33] H. Lu et al., *Adv. Mater.* **24**, 1209, (2012).

[34] X. Liu, Y. Wang, P. V. Lukashev, J. D. Burton, E. Y. Tsymbal, *Phys. Rev. B* **85**, 125407, (2012).

[35] A. M. Kolpak, D. Li, R. Shao, A. M. Rappe, D. A. Bonnell, *Phys. Rev. Lett.* **101**, 36102, (2008).

[36] W. A. Saidi, J. M. P. Martirez, A. M. Rappe, *Nano Lett.* **14**, 6711, (2014).

[37] J. P. Perdew, K. Burke, M. Ernzerhof, *Phys. Rev. Lett.* **77**, 3865, (1996).

[38] S. L. Dudarev, G. A. Botton, S. Y. Savrasov, C. J. Humphreys, A. P. Sutton, *Phys. Rev. B* **57**, 1505, (1998).

[39] J. M. Rondinelli, N. M. Caffrey, S. Sanvito, N. A. Spaldin, *Phys. Rev. B* **78**, 155107, (2008).

[40] P. E. Blöchl, *Phys. Rev. B* **50**, 17953, (1994).

[41] L. Wang et al., *Nano Lett.* **16**, 3911, (2016).

[42] J. L. Li, J. H. Hao, Z. Ying, Y. Li, *Appl. Phys. Lett.* **91**, 201919, (2007).

[43] G. Koster et al., *Rev. Mod. Phys.* **84**, 253, (2012).

[44] M. Yoon et al., *Phys. Rev. Lett.* **99**, 55503, (2007).

[45] D. A. Muller, N. Nakagawa, A. Ohtomo, J. L. Grazul, H. Y. Hwang, *Nature* **430**, 657, (2004).

[46] I. Barin, *Thermochemical Data of Pure Substances* (VCH, New York, 1989).

Chapter 5
Realization of theoretical limit of $BaTiO_3$ ferroelectric critical thickness by interface engineering

5.1 Introduction

Followed with the rapid advancements in heteroepitaxy growth techniques, ultrathin (a few unit-cells thick) ferroelectric (FE) films and heterostructures have attracted considerable research interests recently [1,2]. Reducing dimension of a ferroelectric epitaxial system not only provides exotic physical phenomena but also enables novel tunneling devices with superior data storage abilities [3–12]. Because FE properties strongly depend on local charge distributions [13,14], they are significantly affected by the detailed characteristics of the interface, including polarization screening [15], chemical bonding [16,17], and ferrodistortive cation off-centering [18,19]. As a result, in ultrathin FE systems, the atomic structures of heterointerfaces and surfaces plays a crucial role in determining the functionalities and device performances. For example, atomic stacking sequence at heterointerfaces (or interface termination sequence) significantly affect the electrostatic potential across the FE $BiFeO_3$ films [20]. Yamada *et al.* reported that the ON/OFF ratio of ferroelectric tunnel junction can be enhanced by more than one order of magnitude via proper surface termination engineering [21].

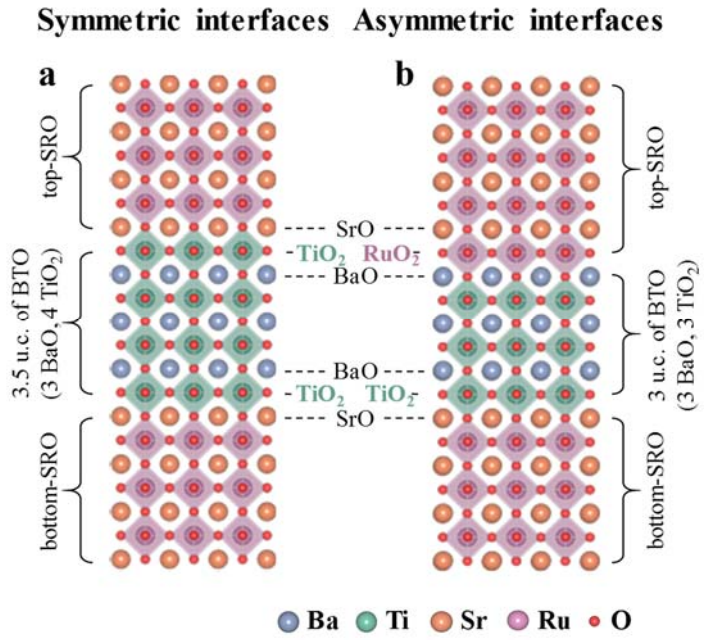

Figure 5.1. Schematic of the possible atomic stacking of the $SrRuO_3/BaTiO_3/SrRuO_3$ (SRO/BTO/SRO) heterostructure with a) symmetric SrO-TiO_2 interfaces, which result in a BTO layer thickness (t_{BTO}) of 3.5 unit cells (u.c.), and with b) BaO-RuO_2 and SrO-TiO_2 interfaces at the top and bottom of the BTO layer, respectively, which result in t_{BTO} = 3 u.c.. Note that the asymmetric case (b) occurs under the commonly assumed *unit-cell by unit-cell* growth mode.

Among such complicated issues, a simple but important issue is the critical thickness at which the ferroelectricity of a single FE layer becomes unstable. For a $PbTiO_3$ film, an X-ray scattering experiment confirmed that FE layers may be stable down to 3 unit cells (u.c.) [22]. However, such a small FE critical thickness value has not been conclusively confirmed in a

real FE capacitor capped between two metallic electrodes. Recent studies on $SrRuO_3/BaTiO_3/SrRuO_3$ (SRO/BTO/SRO) capacitors have shown that the interface termination sequence at metal/FE interface is the key parameter for reducing FE critical thickness. When the interfacial termination sequence is SrO-TiO_2, the ionic displacement inside SRO provides a very efficient mechanism of polarization screening, leading to a reduction of FE critical thickness down to 3.5 u.c. [15,23]. On the contrary, at the SRO/BTO interface with RuO_2-BaO termination sequence, a non-switchable interfacial dipole can pin the FE polarization and significantly increase the FE critical thickness [13,14]. However, the effect of interface termination sequence on FE stability is yet to be experimentally evidenced.

In this Chapter, we investigate strong effect of interface termination sequence on FE polarization switching of SRO/BTO/SRO heterostructures. The SRO/BTO/SRO is a prototypical all oxide heterostructure and has symmetric geometry in material point of view. Therefore it is a suitable system to prove the relationship between interface termination configuration and FE properties. Figure 5.1 shows the two possible interface termination configurations of SRO/BTO/SRO heterostructure. In both cases, bottom interfaces have TiO_2-SrO interface termination because volatile nature of Ru component make SrO-terminated surface be more preferred during SRO deposition [24]. At top interface, both SrO-TiO_2 (left side) and RuO_2-BaO (right side) interface termination can be formed, depending on the termination layer of BTO. As described in **Chapter 4**, the symmetric interface termination configuration can be stabilize only in low P_{O2} = 5 mTorr, while mixed interface termination configuration can be observed in high P_{O2} = 150 mTorr. We found that, with mixed termination

sequences at SRO/BTO interface, FE polarization switching is locally pinned along one direction. On the other hand, in the SRO/BTO/SRO heterostructure with symmetric termination configuration, we can realize the critical thickness of 3.5 unit cells (u.c.), which was theoretically proposed limit in this system.

5.2 Experiments

5.2.1 Sample preparations

Fully strained SRO/BTO/SRO heterostructures were fabricated using pulsed laser deposition (PLD) on atomically smooth TiO_2-terminated $SrTiO_3$(001) substrates. The thicknesses of the bottom and top SRO electrodes were fixed at 20 nm. During the BTO growth, P_{O2} was set to either 5 or 150 mTorr. The BTO film thickness (t_{BTO}) was controlled by monitoring the high pressure RHEED intensity oscillations. The detailed information on the samples can be found in **Chapter 4**.

5.2.2 Grid-PFM measurements

The ferroelectric polarization switching properties were measured using an atomic force microscopy (AFM) system (Cypher Asylum) at room temperature. A commercially available Cr/Pt-coated probe tip with a spring constant of ~ 40 N/m and a resonant frequency of ~ 400 kHz (Tap300E, Budget Sensors) was used. The contact resonance frequency was 1.2 – 1.3 MHz. The high spring constant and contact resonance frequency minimized possible effects

of non-piezoelectric response, such as electrostatic force.[25,26] To carefully investigate the spatial variation of the ferroelectric (FE) switching properties, we divided a single capacitor into a 10 × 10 grid and measured PFM hysteresis loops at each grid point (grid–PFM). The images of the SRO/BTO/SRO capacitor with P_{O2} = 150 mTorr and P_{O2} = 5 mTorr are shown in Figure 5.1a and 5.1b , respectively. The black dots indicate the positions at which grid-PFM is performed.

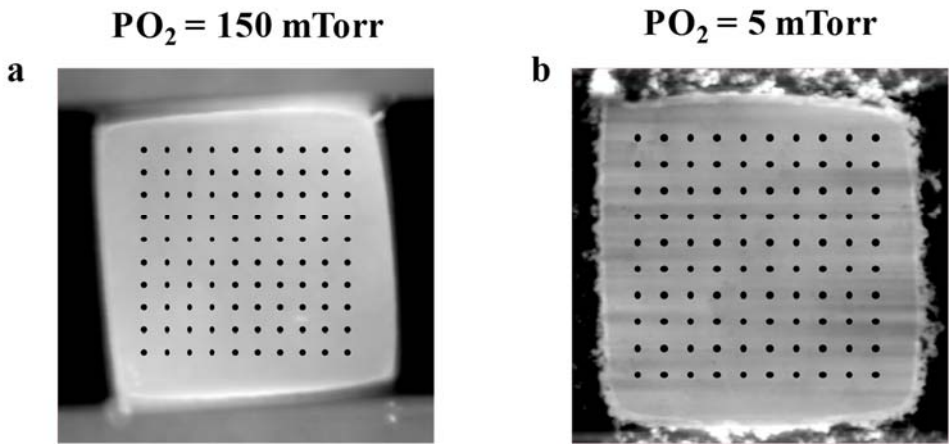

Figure 5.2. AFM topography images of 5 × 5 μm^2 square-shaped SRO/BTO/SRO ferroelectric capacitor with a) P_{O2} = 150 mTorr and b) P_{O2} = 5 mTorr. The black dots schematically show the locations at which the PFM hysteresis loops were measured.

5.3 Results and discussions

5.3.1 Locally-pinned FE polarization switching of SRO/BTO/SRO heterostructure with mixed interface termination sequences

As described in **Chapter 4.3.2,** for P_{O2} = 150 mTorr, we found that two types of termination sequence coexist at the top SRO/BTO interface. With these mixed interface termination sequences, the local FE response varies significantly. Using the electron-beam lithography technique, we fabricated a 5 × 5 μm^2 square-shaped capacitor (see Chapter 5.2.2.). We then chose 10×10 grid positions on the SRO top electrode layer and characterized the local FE responses at each grid point by piezoresponse force microscopy (PFM) (Figure 5.2) [27]. As shown in Figure 5.3, we can observe two typical piezoresponse signals. In region (i) (left panel), the PFM phase-voltage curve shows a fully saturated hysteresis and the PFM amplitude-voltage curve has a nearly symmetric butterfly shape, indicating robust and switchable ferroelectricity. In region (ii) (right panel), by contrast, the PFM amplitude and phase show FE polarization switching characteristics only for the downward polarization state (pointing towards the bottom SRO). This result implies that the FE polarization in the region (ii) is strongly pinned along one direction. The existence of pinned dipoles in the mixed terminated SRO/BTO/SRO capacitor was also proposed by earlier works [13,14,28].

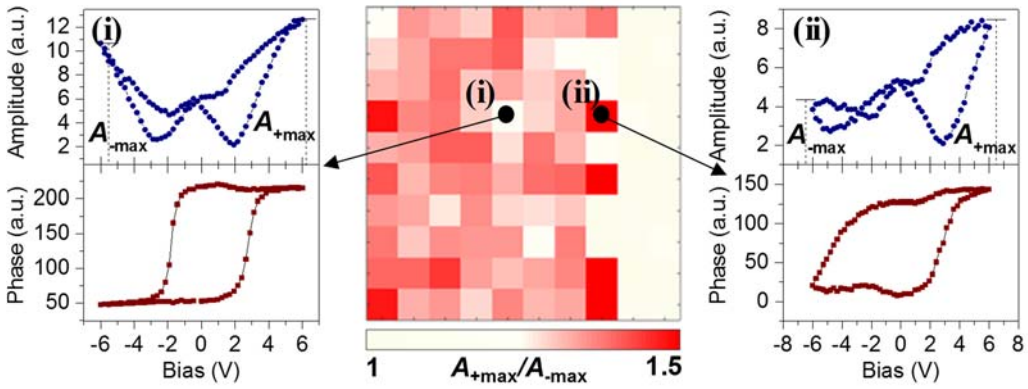

Figure 5.3. The amplitude and phase from piezoresponse force microscopy (PFM) hysteresis loops collected in different locations reveal piezoresponse in both polarization directions (left) and highly pinned piezoresponse along the downward polarization direction (right). The color map at the center of 1d displays the ratio of maximum PFM amplitude response (A_{+max}/A_{-max}) at positive bias (A_{+max}) to that at negative bias (A_{-max}). The black dots marked by (i) and (ii) indicate the points where the left and right plots were measured.

In order to map the spatial variation of the ferroelectricity, we calculated the ratio between the PFM amplitudes at ±6 V (A_{+max}/A_{-max}) at each sampling point. As shown in the central panel of Figure 5.2, for approximately 50% of points the A_{+max}/A_{-max} ratio is close to 1.0, signifying switchable FE response [region (i)]. For the remaining points, A_{+max}/A_{-max} is much higher than 1.0, signifying the response of pinned dipoles [region (ii)]. It is therefore difficult to test the FE critical thickness experimentally with the SRO/BTO/SRO capacitors grown at P_{O2} = 150 mTorr.

5.3.2 Uniform FE polarization switching of SRO/BTO/SRO heterostructure with symmetric SrO-TiO_2 interface termination sequences

5.3.2.1 Uniformity of FE polarization switching and FE critical thickness

In contrast, the heterostructure grown at P_{O2} = 5 mTorr has a uniform BTO top interface and a symmetric termination sequence (**Chapter 4.3.2.**). Using the BTO capacitors with symmetric interfaces, we investigated the FE critical thickness and experimentally confirmed a robust FE response down to t_{BTO} = 3.5 u.c.. We performed PFM hysteresis loop measurements at 10×10 grid points on a capacitor with 5 × 5 μm^2 sizes. Figure 5.4a displays the calculated A_{+max}/A_{-max} ratio of PFM loops measured at each grid point for a t_{BTO} = 3.5 u.c. capacitor. The local variation of the FE response is much smaller than in the sample with mixed BTO termination. For the majority of points, the A_{+max}/A_{-max} values are very close to 1.0, indicating symmetric and switchable FE polarization. The averaged PFM hysteresis loops (Figure 5.4b) also show symmetric butterfly-shaped amplitude-voltage curves and fully saturated phase-voltage curves that are uniform within the error bar. On the other hand, the FE signatures disappear for BTO capacitors with t_{BTO} = 2.5 u.c. (Figure 4c), meaning the FE critical thickness in our devices is 3.5 u.c.. This value is smaller than some theoretical values[29,30] but is consistent with the DFT calculations of G. Gera *et al*., who included charge distribution effects at the interface beyond the Thomas-Fermi capacitor [15].

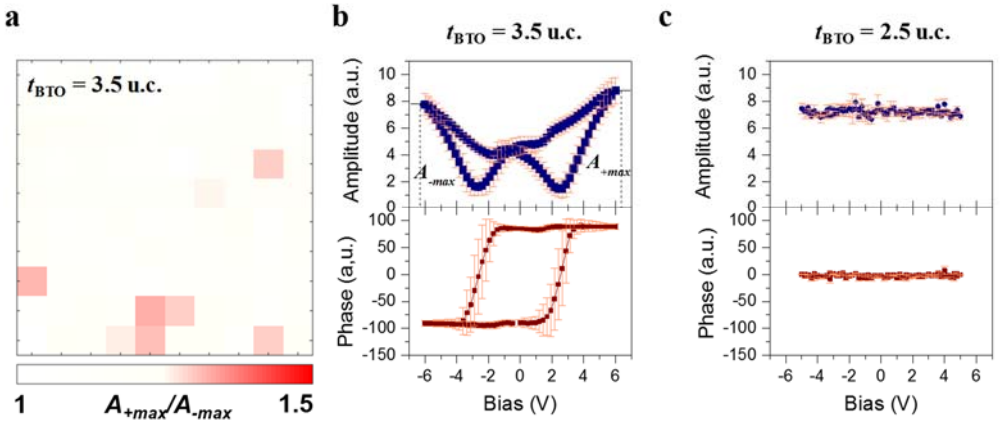

Figure 5.4. a) Color map of A_{+max}/A_{-max} for the SRO/BTO/SRO capacitor with t_{BTO} = 3.5 u.c. and with P_{O2} = 5 mTorr. b) Averaged PFM amplitude and phase hysteresis loops measured at 10×10 different positions in a single capacitor. The error bar indicates the standard deviation of the measured loops. c) Averaged PFM amplitude and phase hysteresis loops of the SRO/BTO/SRO capacitor with t_{BTO} = 2.5 u.c..

5.3.2.2 Further confirmation of FE polarization switching by PFM

Although piezoforce microscopy (PFM) is widely used for detecting ferroelectric (FE) polarization, only providing the PFM hysteresis loop is insufficient to demonstrate the ferroelectricity of the film. In the PFM measurement, the *ac* field (V_{ac})-driven volume change caused by the piezoresponse of the FE film is detected by the cantilever deflection (D_{ac}) of the laser spot on the photodetector. Combined with a step-up *dc* electric field (V_{dc}) (see **Chapter 2.2.1.**), PFM measures the FE polarization at each state. However, differentiating the D_{ac}

induced by FE from the D_{ac} caused by the electrostatic force or ionic motion under the tip is not a straight-forward process.

One method of verifying the FE piezoelectric response contribution to the D_{ac} is investigating the *ac* voltage (V_{ac})-dependence on the PFM hysteresis loops (see **Chapter 2.2.3.**). The amplitude (A) of non-ferroelectrically induced D_{ac} is proportional to the V_{ac}. The effective piezoresponse (PR), therefore, remains the same with varying V_{ac}, whereas the amplitude of the FE-induced D_{ac} abruptly decreases when V_{ac} reaches the coercive voltage (V_c) of the FE layer. The FE polarization flip during the application of V_{ac} disturbs the measurement of the polarization state. The PR loops of the FE film remain stationary when $V_{ac} < V_c$ and start to decrease at $V_{ac} = V_c$ [26,31,32].

The V_{ac}-dependent PFM hysteresis loop measurement confirmed that the PFM responses of our 3.5 u.c. BTO film originated from ferroelectricity and not from the electrostatic force or other effects. Figures 5.5a and 5.5b show the V_{ac}-dependent PFM hysteresis loop change of the sample with t_{BTO} = 3.5 u.c. Both the off-field (loops measured between *dc* pulses) and on-field (loops measured during the application of *dc* pulses) loops showed a sudden loop collapse after the application of the coercive voltage of the film (~ 4 V). The sudden loop collapse clearly indicated the ferroelectric origin of our PFM hysteresis loops. The relatively high coercive field (~ 28000 kV/cm) was caused by the high leakage current at such a thickness limit [33].

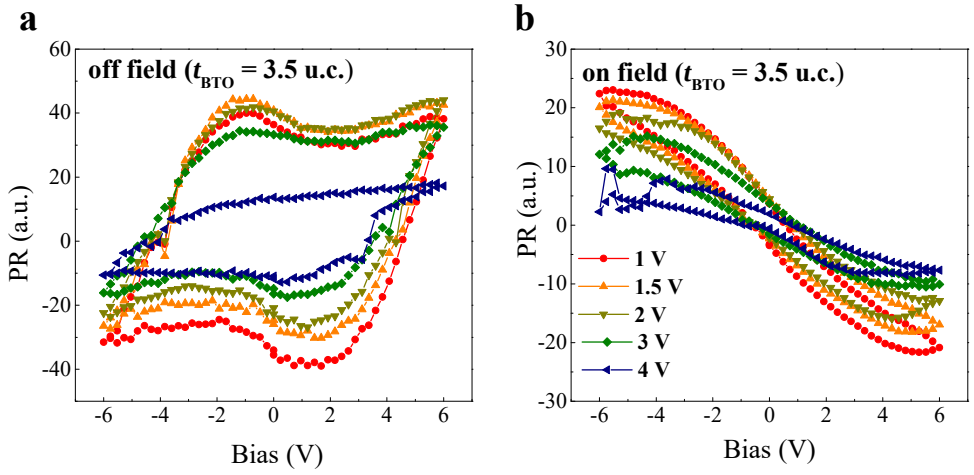

Figure 5.5. The *ac* voltage (V_{ac})-dependent change of a) the off-field hysteresis loop and b) on-field loop, which shows an abrupt loop collapse at a V_{ac} equal to the coercive voltage (e.g., ~ 4 V).

5.3.2.3 Atomic-scale observation of FE polarization

The existence of FE polarization in the t_{BTO} = 3.5 u.c. sample was further confirmed by atomic scale structural analysis. We utilized template matching analysis (TeMA) on the STEM HAADF image [34] to reduce the scan noise and scan distortion. A significant improvement of resolution is achieved when the STEM image (Figure 5.6a) is compared to TeMA image (Figure 5.6b). Each atomic position can be assigned by the peak positions in the TeMA image (red crosses in Figure 5.6b). Figure 5.7c shows the evaluated B-site cation (Ti and Ru) displacements ($\delta_{B\text{-site}}$) from the center position of the A-site cation (Ba and Sr) cages. Please note that $\delta_{B\text{-site}}$ for the Ti atoms shows a maximum displacement of ~ 10 pm, which indicate

BTO polarization. The Ti displacement can also be seen in the enlarged TeMA image (Figure 5.6d).

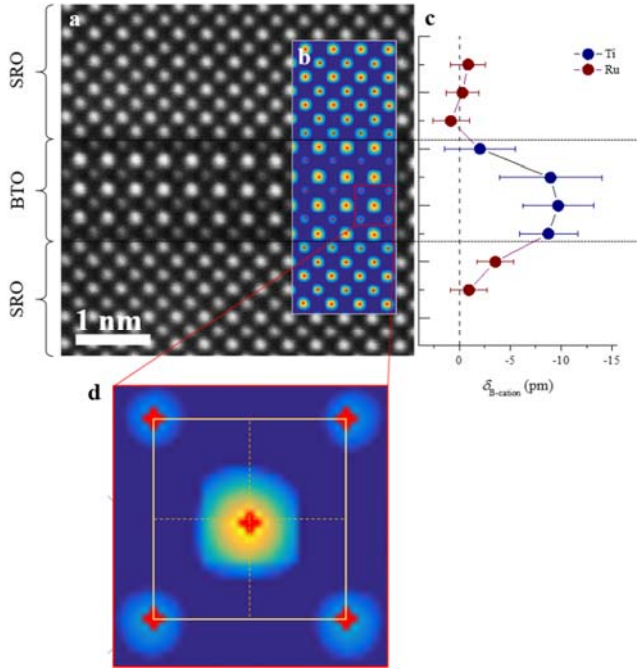

Figure 5.6. a) STEM image of a 3.5 u.c. BTO layer with P_{O2} = 5 mTorr, sandwiched by SRO electrodes. b) Spatially averaged section of 5.5a by template matching analysis (TeMA). The small red crosses indicate the peak positions of each atom. c) The closed circle indicates B-site cation displacement from the center position of the A-site cation cage ($\delta_{B\text{-cation}}$), obtained from the TeMA average peak positions of atoms for each row of 5.5a. Error bars indicate the standard deviation of different columns. d) Enlarged image of the highlighted red box in 5.5b. The yellow box indicates the Ba-cage and dashed lines indicate the cage center position. The difference between the Ti peak and the center position indicates a relative displacement of Ti in the downward direction.

5.4 Conclusion

In summary, we investigated the significant effect of SRO/BTO interface termination on FE properties of SRO/BTO/SRO heterostructures. We found that symmetric interfaces with uniform TiO_2-terminations are crucial for decreasing ferroelectric critical thickness in SRO/BTO/SRO heterostructures, and can only be obtained utilizing a lower oxygen condition (i.e. around P_{O2} = 5 mTorr). As a result, we succeeded in demonstrating the theoretically predicted critical thickness of 3.5 u.c. in a real FE capacitor [15]. Our results suggest that termination control at the atomic scale will serve as a useful tool for exploring the emergent properties of oxide heterostructures and functional devices.

References

[1] S. A. Chambers, *Adv. Mater.* **22**, 219, (2010).

[2] G. Koster et al., *Rev. Mod. Phys.* **84**, 253, (2012).

[3] D. Lee et al., *Science* **349**, 1314, (2015).

[4] T. H. Kim et al., *Nature* **533**, 68, (2016).

[5] A. K. Yadav et al., *Nature* **530**, 198, (2016).

[6] A. Gruverman et al., *Nano Lett.* **9**, 3539, (2009).

[7] A. Chanthbouala et al., *Nat Mater* **11**, 860, (2012).

[8] V. Garcia, M. Bibes, *Nat. Commun.* **5**, 4289, (2014).

[9] V. Garcia et al., *Nature* **460**, 81, (2009).

[10] V. Garcia et al., *Science* **327**, 1106, (2010).

[11] A. Chanthbouala et al., *Nat Nano* **7**, 101, (2012).

[12] L. Wang et al., *Nano Lett.* **16**, 3911, (2016).

[13] H. Lu et al., *Adv. Mater.* **24**, 1209, (2012).

[14] X. Liu, Y. Wang, P. V. Lukashev, J. D. Burton, E. Y. Tsymbal, *Phys. Rev. B* **85**, 125407, (2012).

[15] G. Gerra, A. K. Tagantsev, N. Setter, K. Parlinski, *Phys. Rev. Lett.* **96**, 107603, (2006).

[16] M. Stengel, D. Vanderbilt, N. A. Spaldin, *Nat. Mater.* **8**, 392, (2009).

[17] C. G. Duan, R. F. Sabirianov, W. N. Mei, S. S. Jaswal, E. Y. Tsymbal, *Nano Lett.* **6**, 483, (2006).

[18] J. M. Pruneda et al., *Phys. Rev. Lett.* **99**, 226101, (2007).

[19] W. Zhong, D. Vanderbilt, *Phys. Rev. Lett.* **74**, 2587, (1995).

[20] P. Yu et al., *Proc. Natl. Acad. Sci. U. S. A.* **109**, 9710, (2012).

[21] H. Yamada et al., *Adv. Funct. Mater.* **25**, 2708, (2015).

[22] D. D. Fong et al., *Science* **304**, 1650, (2004).

[23] Y. J. Shin et al., *Adv. Mater.* **29**, 1602795, (2017).

[24] G. Rijnders, D. H. A. Blank, J. Choi, C.-B. Eom, *Appl. Phys. Lett.* **84**, 505, (2004).

[25] S. Jesse, A. P. Baddorf, S. V Kalinin, *Nanotechnology* **17**, 1615, (2006).

[26] N. Balke et al., *ACS Nano* **9**, 6484, (2015).

[27] S. Jesse, A. P. Baddorf, S. V. Kalinin, *Appl. Phys. Lett.* **88**, 21, (2006).

[28] G. Gerra, A. K. Tagantsev, N. Setter, *Phys. Rev. Lett.* **98**, 207601, (2007).

[29] B. Meyer, D. Vanderbilt, *Phys. Rev. B* **63**, 205426, (2001).

[30] J. Junquera, P. Ghosez, *Nature* **422**, 506, (2003).

[31] M. Andrä et al., *Nanoscale* **7**, 14351, (2015).

[32] E. Strelcov et al., *Appl. Phys. Lett.* **101**, 192902, (2012).

[33] N. A. Pertsev et al., *Appl. Phys. Lett.* **83**, 3356, (2003).

[34] J. Zuo et al., *Ultramicroscopy* **136**, 50, (2014).

Chapter 6
Conclusions

In recent decades, atomic-scale heterointerfaces engineering has advanced significantly in oxide filed. And important developments have been achieved that include PLD with *in situ* reflection high-energy electron diffraction (RHEED) and the use of numerous calculation methods, such as first-principle calculations [1–5]. These advancements have enabled the design of new classes of oxide heterostructures and the exploration of novel emerging phenomena [6–10]. Illustrative examples of such phenomena include two-dimensional electron gas at the interface of insulators [11–13], interface superconductivity [14,15], topological effects [16], magneto-electric coupling [17,18], and ferroelectric polar vortices [19]. Such emerging properties stem from abrupt interfaces that present appropriate sequences of atomic layers [9,20].

The atomic-scale control of heterointerfaces also has become crucial for ferroelectric (FE) materials. With recent trends on miniaturizing oxide devices, the thickness of FE layer used in FE devices has decreased down to nanometer scale. In such small thickness, various interfacial effect can affect the functional properties of FE layer. Thus, for fine-tuning of FE device performance, realization of atomically controlled interface is necessary. However, the task of creating desirable interface structures through atomic control is challenging, even for simple perovskite oxides. To form an abrupt interface, a high-temperature growth step is usually required to obtain sufficient adatom mobility [21]. However, such a high temperature can

simultaneously induce entropy-driven disordered structures, such as anion/cation vacancies, inter-diffused interfaces, or other complex phases [22]. In most oxide fabrication techniques, such as PLD and sputtering, the amount of individual constituent elements cannot be controlled, which increases the difficulty of determining the exact termination. Even with reactive molecular beam epitaxy, where the individual constituents can be controlled, the intended atomic stacking sequence is often inconsistent with the actual layering sequence [23,24]. In addition, numerous surface reconstructions can occur on oxide surfaces in a wide region of thermodynamic condition, which hinder the formation of abrupt interfaces [25–29].

In FE $BiFeO_3$ (BFO) capacitor, we investigated effect of electrode/FE interface on *ac* dynamics of FE domain walls. By using $P-E$ hysteresis loop measurements and stroboscopic-PFM, we are able to characterize the FE domain wall nucleation and propagations. In particular, we found that BFO grown on different electrodes, $La_{0.67}Sr_{0.33}MnO_3$ (LSMO) and $SrRuO_3$ (SRO) shows very different non-linear 'creep' dynamics of FE domain walls; while BFO/LSMO exhibit typical creep dynamics regime, BFO/SRO shows nearly creep-free dynamics. The temperature dependent $P-E$ measurement and resulting *ac* hysteretic phase diagram shows that the creep-free dynamics of BFO/SRO comes from significantly reduced interface quenched defects. The atomically smooth surface/interface morphology is attributed to the origin of reduced defects of BFO/SRO.

For the atomic-scale control of interface termination sequence, we intentionally investigated the pulsed laser deposition (PLD) growth of FE heterostructures. By growing prototypical SRO/$BaTiO_3$ (BTO)/SRO FE capacitor as model system, we realized selective

fabrication of SrO-TiO_2 and BaO-RuO_2 termination sequences at SRO/BTO interface. We found that relatively high background oxygen partial pressure (P_{O2}) during growth induced heterogeneous interface termination sequences, while with low P_{O2}, uniform SrO-TiO_2 termination sequence was formed. With help of synergetic density functional theory (DFT) calculation and experiment, we revealed that the P_{O2}-dependent interface termination sequence originated from the variations in thermodynamic energy of BaO- and TiO_2-terminated BTO surface during growth.

Depending on the SRO/BTO termination sequence, the FE polarization switching properties differ significantly. By using switching spectroscopy-piezoelectric force microscopy (SS-PFM), we investigated different FE polarization switching of ultrathin BTO layer with SrO-TiO_2 or with heterogeneous interface termination sequences. We found that, with heterogeneous termination sequences, FE polarization is locally-pinned along one direction. On the other hand, uniform FE polarization switching was observed with SrO-TiO_2 termination sequence. In particular, SRO/BTO/SRO with SrO-TiO_2 termination sequence exhibited robust FE polarization switching with thickness down to 3.5 unit cells, the theoretically expected thickness limit of the system.

In conclusions, our studies described in this thesis provide the better understandings on atomic-scale control of metal/FE interface and their effects of FE properties, which is important for realizing FE-based nanoelectronics devices. In addition, we expect that our strategy used in our works can be generalized for other complex oxide heterostructures.

References

[1] J. M. Rondinelli, N. A. Spaldin, *Adv. Mater.* **23**, 3363, (2011).

[2] J. M. Rondinelli, N. A. Spaldin, *Phys. Rev. B* **82**, 113402, (2010).

[3] J. He, A. Borisevich, S. V. Kalinin, S. J. Pennycook, S. T. Pantelides, *Phys. Rev. Lett.* **105**, 227203, (2010).

[4] M. Stengel, N. A. Spaldin, *Nature* **443**, 679, (2006).

[5] M. Stengel, D. Vanderbilt, N. A. Spaldin, *Nat. Mater.* **8**, 392, (2009).

[6] J. Heber, *Nature* **459**, 28, (2009).

[7] J. Mannhart, D. G. Schlom, *Science* **327**, 1607, (2010).

[8] P. Zubko, S. Gariglio, M. Gabay, P. Ghosez, J.-M. Triscone, *Annu. Rev. Condens. Matter Phys.* **2**, 141, (2011).

[9] H. Y. Hwang et al., *Nat. Mater.* **11**, 103, (2012).

[10] J. Chakhalian, A. J. Millis, J. Rondinelli, *Nat. Mater.* **11**, 92, (2012).

[11] A. Ohtomo, H. Y. Hwang, *Nature* **427**, 423, (2004).

[12] M. Huijben et al., *Adv. Mater.* **21**, 1665, (2009).

[13] H. Chen, A. M. Kolpak, S. Ismail-Beigi, *Adv. Mater.* **22**, 2881, (2010).

[14] N. Reyren et al., *Science* **317**, 1196, (2007).

[15] Y. Kozuka et al., *Nature* **462**, 487, (2009).

[16] D. Doennig, W. E. Pickett, R. Pentcheva, *Phys. Rev. B* **89**, 121110, (2014).

[17] S. M. Wu et al., *Nat. Mater.* **9**, 756, (2010).

[18] V. Garcia et al., *Science* **327**, 1106, (2010).

[19] A. K. Yadav et al., *Nature* **530**, 198, (2016).

[20] N. Nakagawa, H. Y. Hwang, D. A. Muller, *Nat. Mater.* **5**, 204, (2006).

[21] C.-H. Lee et al., *Nature* **502**, 532, (2013).

[22] W. S. Choi et al., *Adv. Mater.* **24**, 6423, (2012).

[23] J. H. Lee et al., *Nat. Mater.* **13**, 879, (2014).

[24] Y. F. Nie et al., *Nat. Commun.* **5**, 4530, (2014).

[25] R. Richards, CRC/Taylor & Francis, Florida, USA, 2006.

[26] G. Somorjai, *Annu. Rev. Phys. Chem.* **45**, 721, (1994).

[27] N. Erdman et al., *Nature* **419**, 55, (2002).

[28] A. M. Kolpak, D. Li, R. Shao, A. M. Rappe, D. A. Bonnell, *Phys. Rev. Lett.* **101**, 36102, (2008).

[29] W. A. Saidi, J. M. P. Martirez, A. M. Rappe, *Nano Lett.* **14**, 6711, (2014).

Appendix: Foolproof manual for pulsed laser deposition, Compact-Laser MBE (PASCAL Co., Ltd.)

Appendix 에서는 실험실에 설치 된 Compact-Laser MBE (PASCAL Co., Ltd.) 장비에 관한 매뉴얼을 남긴다. 해당 장비는 본 논문에서 다룬 $BaTiO_3$, $SrRuO_3$ 등의 산화물 박막 증착에 사용되었으며, 해당 물질이 연구단에서 지속적으로 연구되고자 하는 바람으로 최대한 증착 과정을 자세히 묘사하고 주요 증착 조건들을 참고로 남긴다.

A.1 PLD system 의 구성

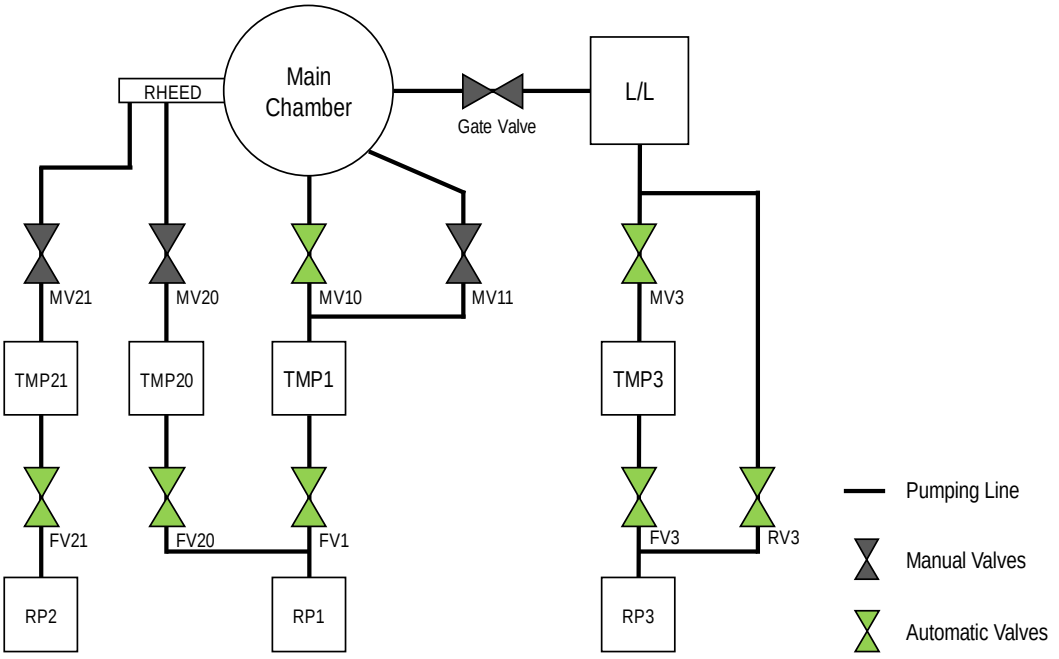

Figure A1. PLD system 의 진공 구조도

Compact-Laser MBE 모델은 2 개의 chamber, 4 개의 turbo pump, 3 개의 rotary pump, 그리고 RHEED system 으로 이뤄져 있다. 전체 진공 파트의 도식은 Figure A1 에 정리되어 있다. 본 단락에서는 진공파트를 이루고 있는 각 pump 와 gate valves 들의 위치와 모양을 소개하고자 한다.

1. Main turbo system

   A. Main chamber: 실제 증착이 이뤄지는 chamber

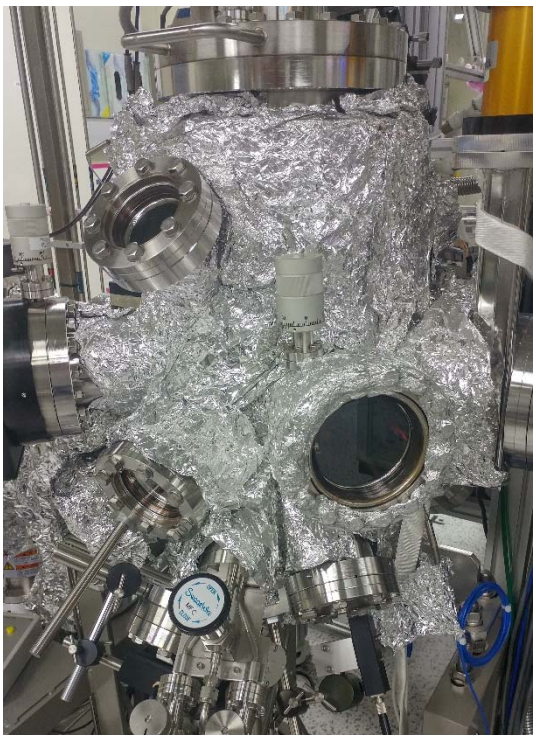

   B. TMP1: Main chamber 진공을 위한 turbo pump.

C. MV10: Main chamber 와 TMP1 을 잇는 공압 밸브.

D. MV11: Main chamber 의 고분압 background gas 주입 시 이용하는 bi-pass 밸브. MV10 보다 흡입량이 작아 분압 조절이 유리.

E. RP1: Main chamber 와 RHEED 의 rough vacuum 을 잡기 위한 rotary pump.

F. FV1: TMP1 과 RP1 을 잇는 공압 밸브.

2. RHEED differential pumping system

A. RHEED gun: high-energy electron beam 을 조사하는 gun. 고 산소분압에서 박막 증착 시, 산소에 의해 gun 의 filament 가 쉽게 산화되어 끊어지기 때문에 differential pumping system 을 통해 항상 고 진공을 유지하도록 설계되어 있다.

B. TMP20: RHEED differential pumping 을 위한 첫번째 turbo pump. TMP1 과 rotary pump (RP1)을 공유하며, 고분압에서 RHEED 사용시 가장 망가지기 쉬운 pump 이므로 주의.

C. TMP21: RHEED differential pumping 을 위한 두번째 turbo pump.

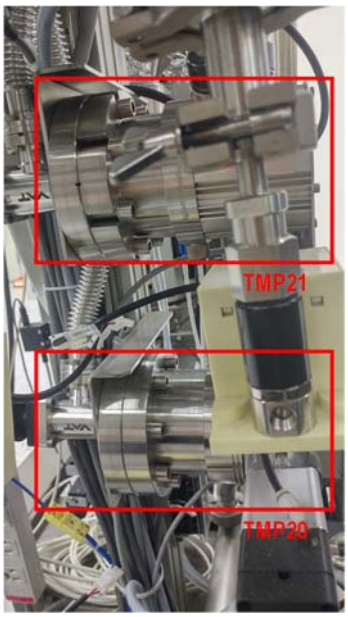

D. MV20: RHEED 와 TMP20 를 잇는 manual valve. (labeling 이 FV20 으로 잘못 되어 있으니 주의).

E. MV21: RHEED 와 TMP21 을 잇는 manual valve. (labeling 이 FV21 로 잘못 되어 있으니 주의).

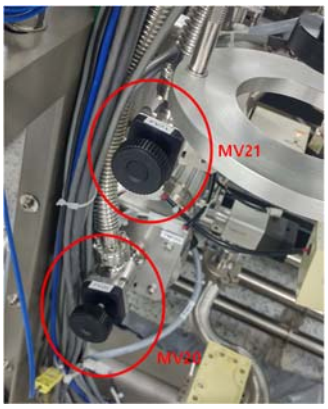

F. RP2: TMP21 을 위한 rough vacuum 을 잡기 위한 ratary pump.

G. FV20: TMP20 과 RP1 을 잇는 공압 밸브.

H. FV21: TMP21 과 RP2 를 잇는 공압 밸브

3. Load Lock system

A. Load lock (L/L) chamber: 기판의 pre-heating 과 loading 을 위한 chamber.

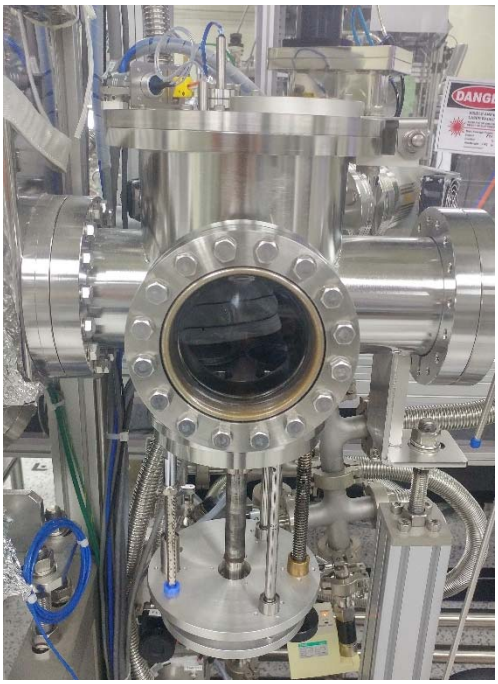

B. TMP3: L/L chamber 의 진공을 위한 turbo pump.

C. MV3: L/L chamber 와 TMP3 를 잇는 공압 밸브.

D. RP3: L/L chamber 의 rough vacuum 을 잡기 위한 rotary pump. 전체 PLD system 을 venting 한 후에는 전체 PLD 의 rough vacuum 을 잡기 위해서도 사용 된다.

E. RV3: 샘플 홀더 loading 을 위해 L/L chamber 를 venting 한 후에 TMP3 를 껐다 켜지 않고 L/L chamber 의 rough vacuum 을 잡게 하기 위한 bi-pass 공압 valve.

4. Main gate valve: Main chamber 와 L/L chamber 를 있는 manual valve. 샘플 홀더를 이동시키기 위해 밸브 자체가 크기 때문에 항상 완전히 닫혔는지 주의할 것.

5. PLD system control panel: Excimer laser, target selection & rotation, temperature control 등을 할 수 있는 Lab view software.

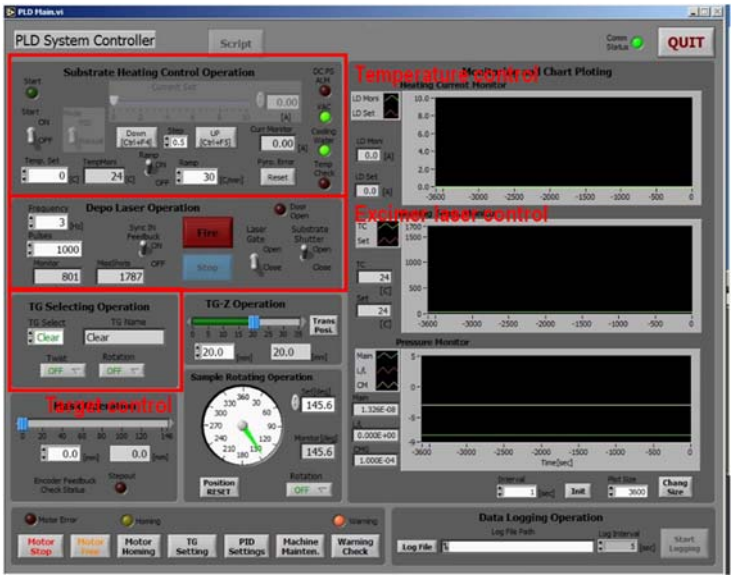

6. Motor control panel: 공압 밸브, turbo pump, rotary pump, gauge 들을 제어하는 panel. Panel 에 표시된 pump 들과 밸브들의 명칭은 본 단락의 설명에 나오는 것과 일치한다. Pump 의 경우 초록 불이 켜진 것이 작동 중, 회색 빛으로 꺼진 것이 전원을 끊은 상태를 의미. 밸브의 경우 초록 불이 들어온 것이 열려있는 상태, 회색 빛으로 꺼져 있는 것이 닫혀 있는 상태를 의미한다. On/off 는 해당 부분을 마우스 커서로 클릭해서 이뤄진다.

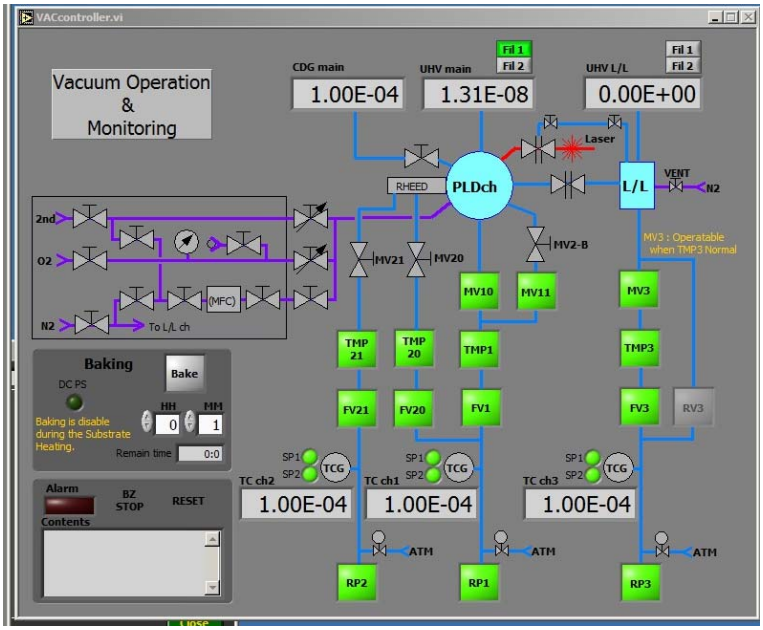

A.2 박막 증착 과정

A.2.1 기판 준비

Acetone 과 CF-909 와이퍼를 이용해 표면을 잘 닦은 기판을 준비한다. 기판 홀더와 클램프는 800 사포를 이용하여 갈아낸다. 이는 지난 증착 후 남아있는

target 물질을 없애기 위함이다. 사포 질 후에는 Acetone 혹은 IPA 용액이 담긴 비커에 넣고 5 분간 sonication 한 후에, 다시금 Acetone 으로 잘 세척한다. 증착 도중 박막과 홀더 사이의 열전도를 좋게 하기 위하여 냉장 보관되어 있는 Pt paste 를 이쑤시개를 이용하요 소량 홀더 중앙에 도포한다. 트위져를 이용하여 조심스럽게 기판을 도포된 Pt paste 위에 올린 뒤 기판 구석을 살며시 눌러 기판을 홀더 위에 부착시킨다. 이 때 Pt paste 안의 기포가 잘 제거 될 수 있도록 기판으로 홀더 표면을 문지르듯이 움직여 주면 좋다. 이 과정에서 Pt-past 의 양이 많아 기판 모서리 위로 올라오게 될 경우 후에 RHEED 패턴을 잡는 데 어려움이 있을 수 있으므로 이쑤시개를 이용해 제거한다. Pre-heating 과 증착 과정에서 홀더가 바닥을 바라보게 되기 때문에 클램프와 나사를 이용하여 기판 귀퉁이를 고정시킨다.

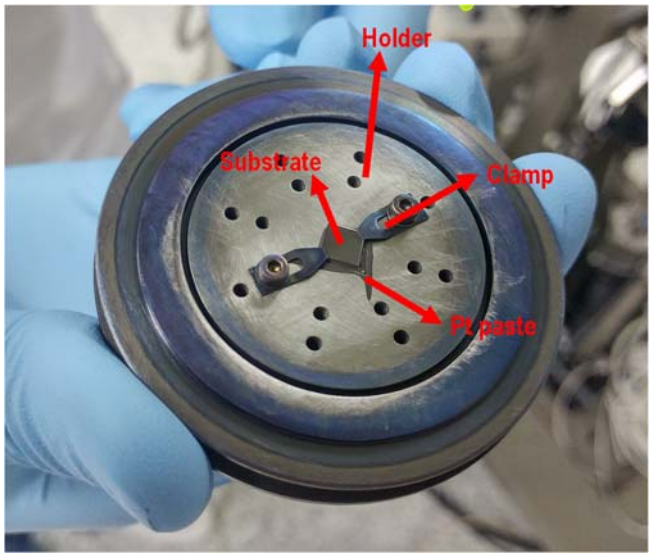

A.2.2 진공 장비 상태 확인

Screen 과 turbo controller 를 확인하여 현재 Main chamber 와 L/L chamber 의 진공 상태, turbo pump 들의 파워를 기록한다. 정상적인 상태에서 Main chamber 의 진공은 최대 5E-8 Torr 를 넘지 말아야 하며, L/L 의 경우는 1E-7 Torr (vent 직후는 1E-5 Torr)가 되어야 한다. TMP3, TMP20, TMP21 의 경우 9W 가 넘는 경우는 문제가 있는 것이다. 온도는 섭씨 30 도를 넘지 않아야 한다. TMP1 의 경우 0.5 A 를 보여야 한다.

A.2.3 L/L chamber 로 홀더 loading 하기

A.2.3.1 L/L 진공 깨기

- L/L ion gauge (screen 에서 L/L 위의 Fil1 으로 표시) 를 끈다.
- MV3 를 닫는다.

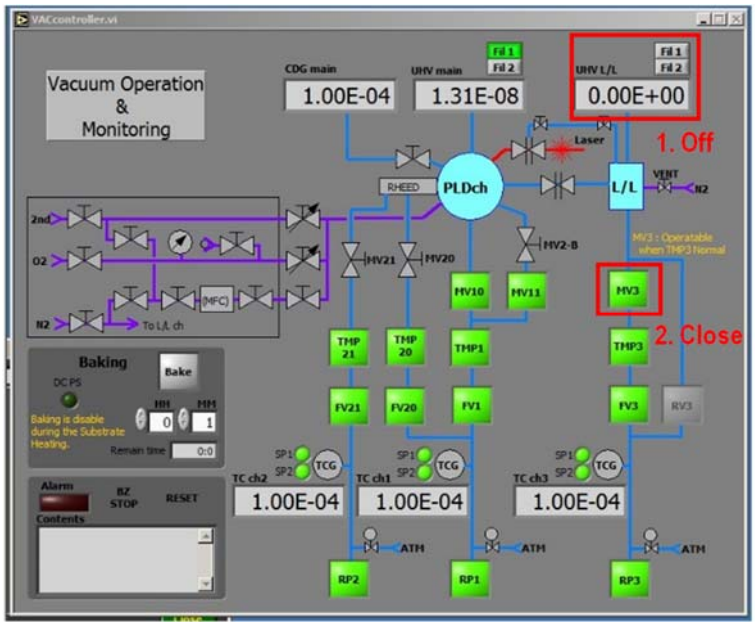

- Door clamp 나사를 열어둔다. 만약 나사가 닫힌 상태로 질소를 주입하다가 압력이 지나치게 높아질 경우, 나사가 힘을 받아서 팅겨 나올 수 있다.

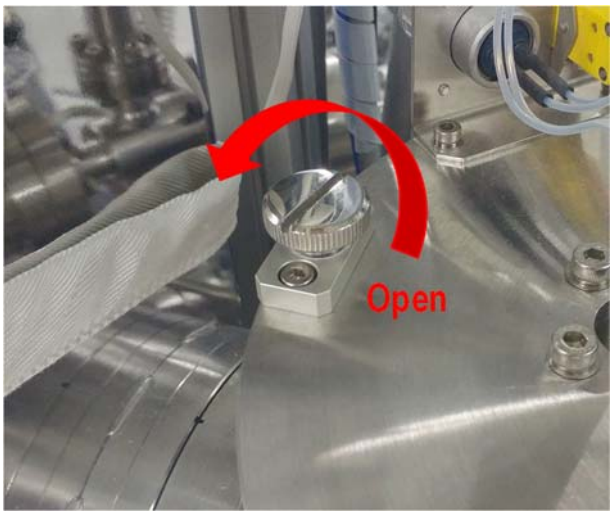

- Venting valve 를 아주 살짝 연 후에 TMP3 와 TMP1 의 파워가 올라가지 않는지 확인한다. MV3 나 Main gate valve 가 완전히 잠기지 않을 경우 파워가 올라갈 것이기 때문에, 이경우 다시 venting valve 를 닫고 밸브들을 확인한 뒤 venting valve 를 다시 연다.

- L/L door 가 완전히 열린 것을 확인 한 후 venting valve 를 잠근다.
- A.2.1.에서 준비한 홀더를 L/L 챔버에 넣는다.

- L/L door 를 닫고 클램프 나사를 잠근다.

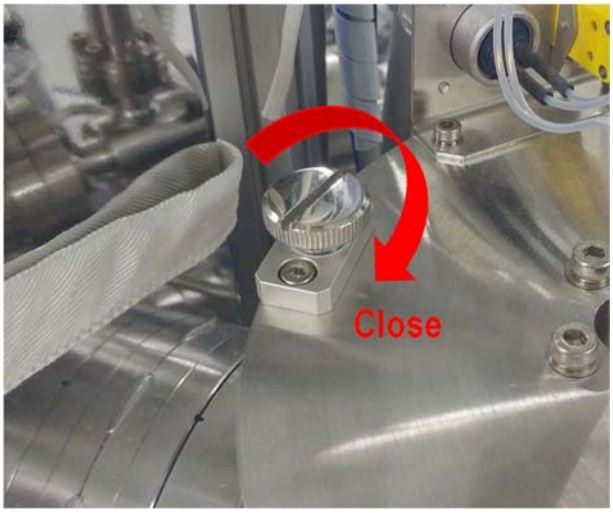

A.2.3.2 L/L 진공 잡기

- FV3 를 잠근 후 RV3 를 연다.

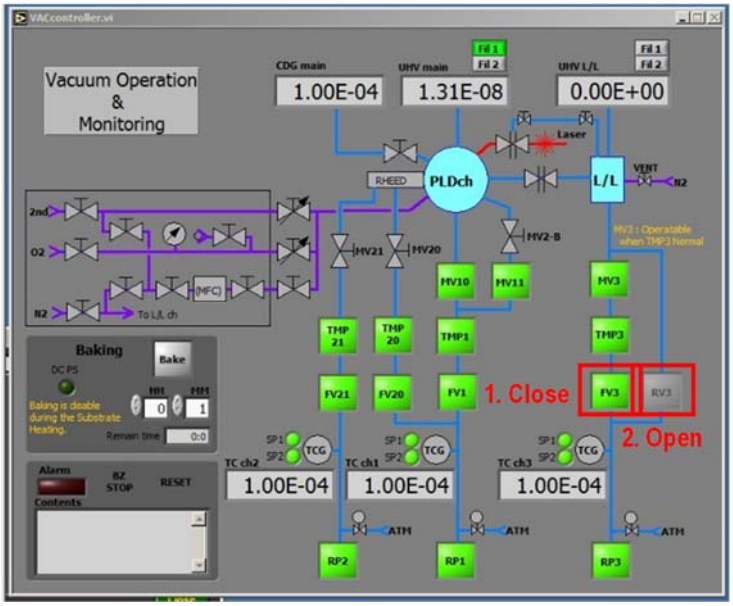

- L/L stage 를 끝까지 올린 후 방향을 조절하여 홀더를 Pre-heater 에 가깝게 붙인다.
- RP2 에 연결 된 cap. gauge 값이 1E-4 Torr 이하로 내려가면, RV3 를 잠근 후 FV3 와 MV3 를 연다. 마지막으로 L/L ion gauge (Fil1)를 켠다.

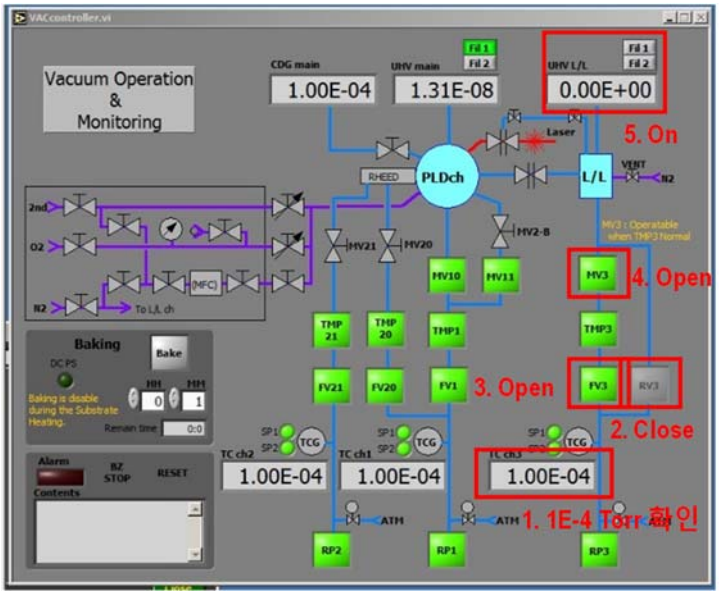

- Pre-heater 를 켜서 기판의 pre-heating 을 시작한다. Pre-heating 은 30 분 동안 진행된다.

A.2.4 Laser power 재기

Pre-heating 이 진행되는 동안 증착에 필요한 Excimer laser parameter 를 측정한다. Excimer laser 의 경우 laser 내부의 gas 양의 따라 파워가 크게 달라지므로, 발진 전압을 믿지 말고 실제 power meter 로 측정을 해가며 원하는 laser intensity 를 위한 발진 전압을 알아야 한다.

- Excimer laser controller 의 'Run/Stop' 버튼을 누른 뒤 'EXE' 버튼을 누른다. 수초 뒤 Excimer laser 의 등이 점화되는 것을 확인한다.

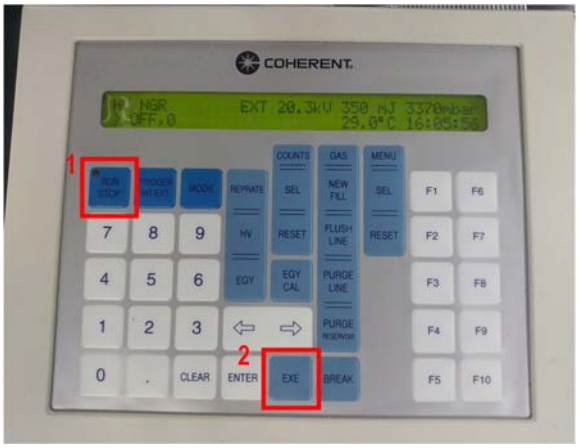

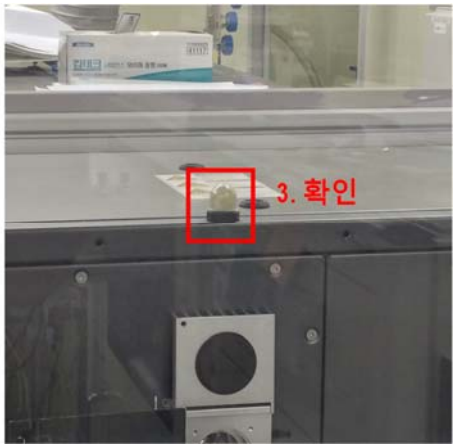

- Excimer laser 파워미터가 달려있는 뷰포트의 셔터를 열고 파워미터를 켠다.

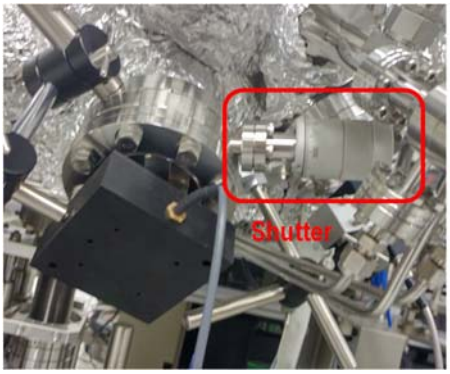

- Target holder 위치를 “Clear”로 맞춘다.
- PLD system control panel 에서 Excimer laser 의 repetition rate 을 10 Hz 로 맞춘 후에 “Fire” 버튼을 눌러 발진 시킨다.

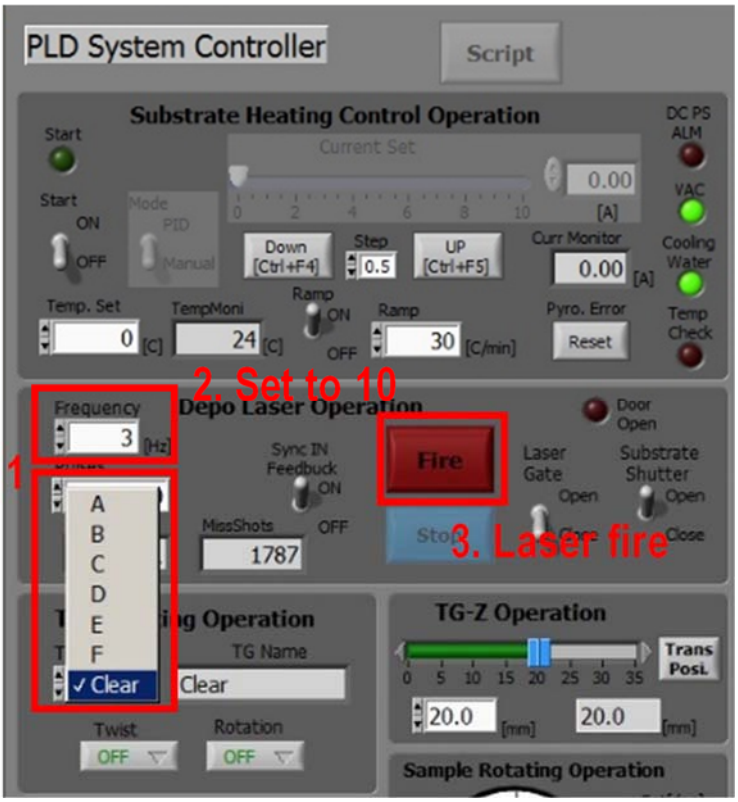

- Excimer laser controller 의 ‘HV’ 버튼을 누른 뒤 원하는 발진 전압을 입력하고 ‘ENTER’ 버튼을 눌러 적용시킨다. 원하는 laser power 가 나올 때까지 반복한다.

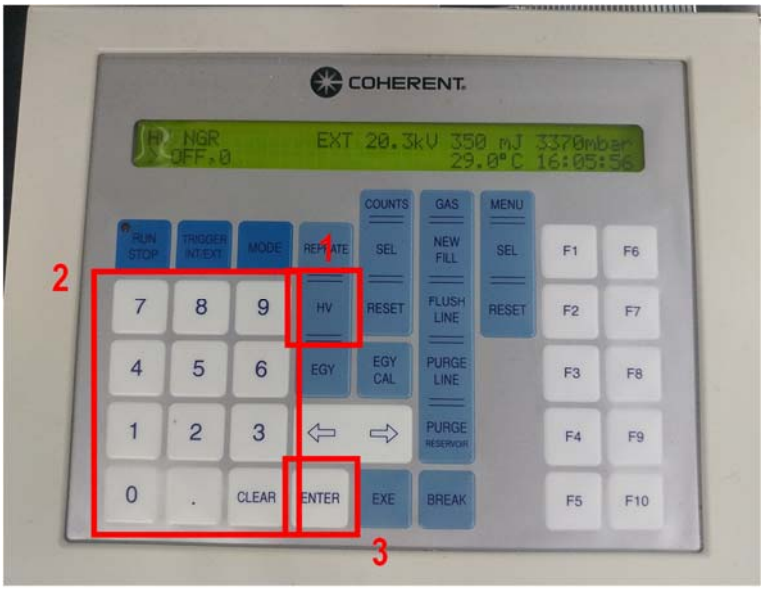

- 원하는 값들을 찾았으면 해당하는 발진 전압 값을 기록해둔다.

- PLD system control panel 에서 “Stop” 버튼을 눌러 레이저를 멈춘다.

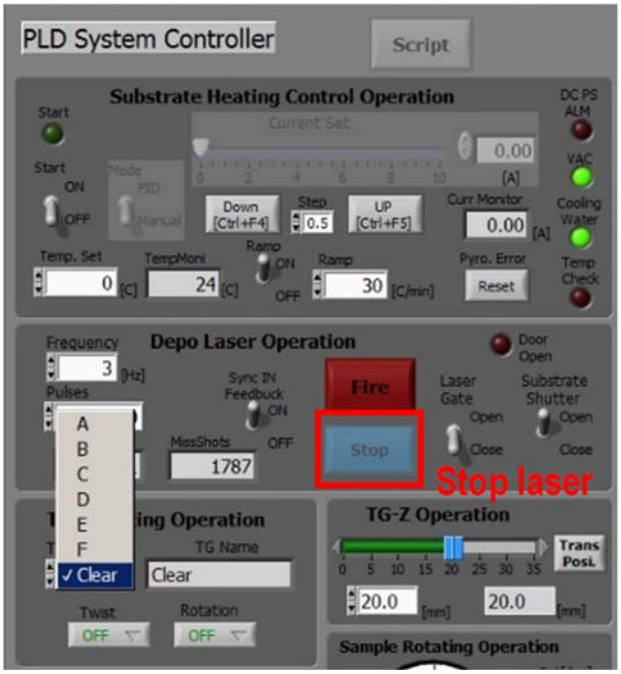

A.2.5 L/L 에서 Main chamber 로 홀더 transfer 하기

- Pre-heating 이 끝났으면, transfer fork 를 맨 뒤로 뺀 상태에서 L/L stage 높이를 fork 높이까지 올린다.
- Fork 를 홀더 홈에 끼운 뒤에 L/L stage 를 fork 가 움직일 수 있는 위치까지 내린다.
- Main gate valve 를 연다.

- Fork 를 Main chamber 로 밀어 넣은 후에 Main chamber 의 halogen lamp 와 홀더 stage 의 높이를 홀더가 들어갈 수 있도록 잘 조정한다. x 값을 10.5, y 값을 8 에 맞춘다. 만약 이전 증착을 마친 후에 특별한 조취를 취하지 않았다면 이 위치들은 자연스레 맞춰져 있을 것이다.

- Fork 를 끝까지 밀어넣은 후에 홀더 stage 높이를 조절하여 홀더가 fork 에서 살짝 뜨도록 만든 뒤 Fork 를 빼낸다.
- Main gate valve 를 닫는다.
- Lamp 와 홀더 stage 의 높이를 “deposition” 이라고 표시된 위치까지 조절한다.

- 홀더의 ‘x’, ‘y’ 위치를 원하는 위치로 옮긴다 (Plume 중앙은 x=11.8, y=2.4).
- JOG controller 로 state 를 회전시켜 기판의 한 쪽 모서리가 RHEED gun 을 바라보도록 맞춘다.

A.2.6 RHEED align 하기

- RHEED power 를 켠다.

- Fil, HV, FOC, X, Y 순으로 cotoller 를 켠다.

- Fil 값을 1800 mA 까지 천천히 올린 후, HV 를 18 kV 까지 천천히 올린다. 이 값은 현재 RHEED filament 값에 따라 다를 수 있으므로 만약 direct beam 이 안보인다면 Fil 값과 HV 값을 줄여보는 것을 추천한다.

(아래 붉은 색으로 표시된 내용은 RHEED 패턴이 잘 잡히지 않을 때 사용하는 방법으로 우선 빼고 패턴을 잡아본 다음 안 될 경우에만 시행한다.)

- RHEED gun 구멍을 'L'에 맞춘다.

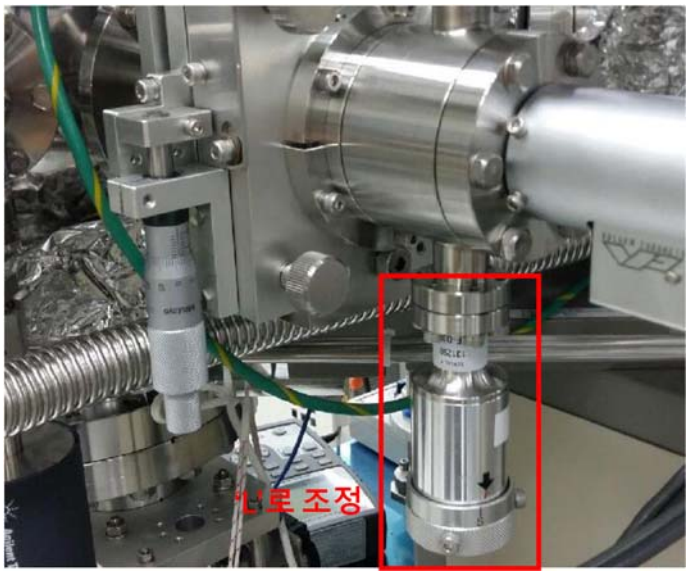

- Beam 위치를 아래로 끝까지 내려서 direct beam 이 잘 나오는지 확인한다. Beam 이 약할 경우 Fil 과 HV 값을 조정.

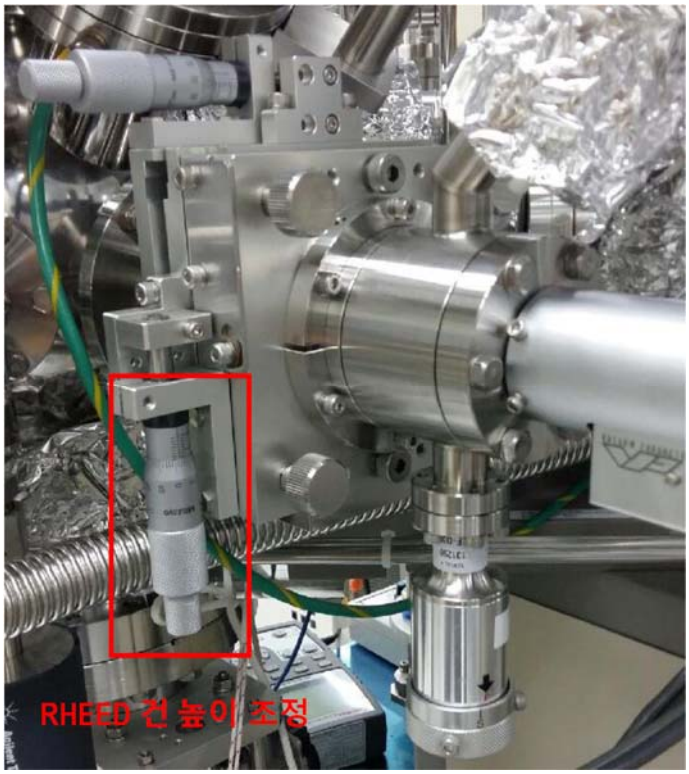

- 다시 beam 을 올려가면서 sample 위치 까지 올린다. 패턴이 보이기 시작하면 JOG controller 로 기판을 천천히 회전시켜서 원하는 방향의 패턴을 얻는다.

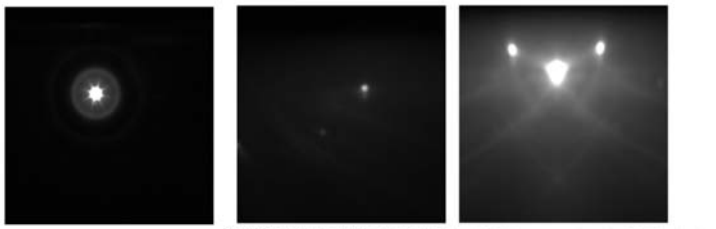

Direct spot

RHEED pattern along the non-principle crystallographic direction of a substrate.

RHEED pattern along the [100] azimuth.

- 기판 방향을 잡았으면, 다시 beam 을 끝까지 내린 후에 gun 구멍을 'S'로 맞춘다.
- Direct beam 이 보이면 RHEED controller 에서 X, Y 조절하여 intensity 를 최대로 맞춘다.
- RHEED gun 을 위로 올려서 electron beam 이 기판에 맞게 한다.
- 패턴이 나타나면 JOG controller 로 기판 방향을 세밀하게 조절하여 원하는 패턴 방향을 맞춘다.
- kSA software 에서 real-time monitoring 창을 켜고 pattern 위에 ellipse mark 표시.
- "Start" 버튼을 클릭하여 moniotoring 을 시작한 후에 beam 높이, X, Y, Fil, HV 를 바꿔가면서 intensity 를 최대화 한다.

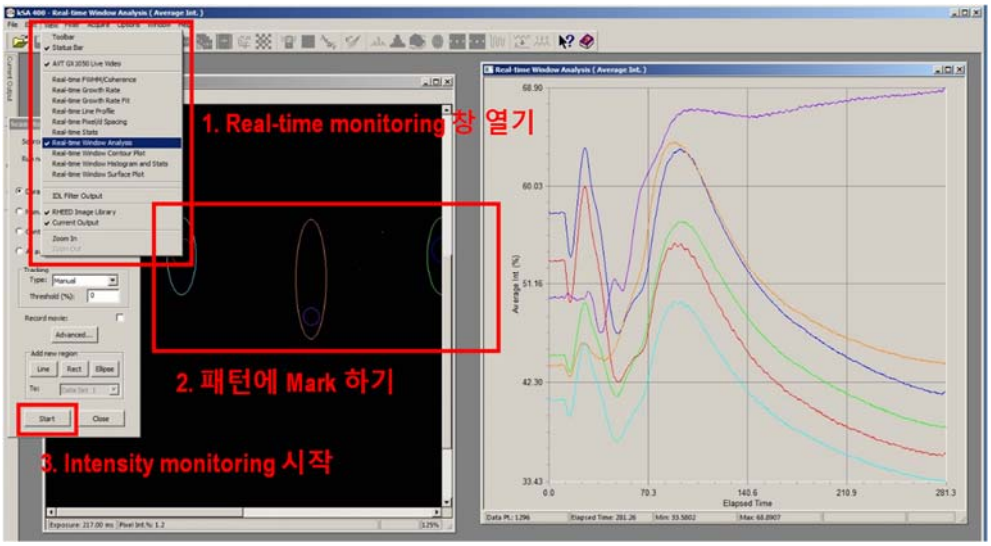

- RHEED 패턴 이미지를 저장한다.

A.2.7 온도 올리기 / 산소 넣기

- 기판 온도 측정을 위한 파이로미터 controller 를 align 한다. 파이로 미터 controller 에 ‘mode’버튼을 6 회 누른 후 ‘▼’버튼을 한 번 누른 뒤 ‘ent’버튼을 누르면 aligning laser 가 켜진다. 이후 파이로미터를 나사를 조절하여 aligning laser 가 기판 위로 올라오도록 한다. 이후 ‘mode’버튼을 한 번 더 눌러 aligning laser 를 끄도록 한다.

- MV11 (Main chamber 의 bi-pass valve)를 한 바퀴 열어둔다. 이는 이후 MV10 을 닫을 때 분압이 계속 올라가는 것을 막기 위해서 이다.

- 현재 시각, Main chamber 분압 등을 기록한 후에 Leak valve 를 열어 산소를 조금씩 넣는다. Main chamber 의 ion gauge 가 7-8E-05 Torr 가 될 때까지 한다.

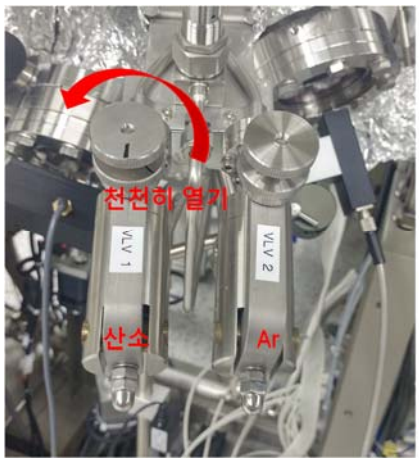

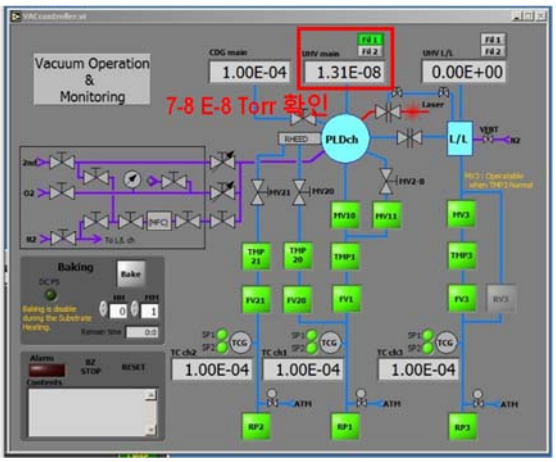

- 현재 시각, 산소 분압을 기록한 후에 Main chamber 의 ion gauge 를 끈다.
- MV1 을 닫는다.

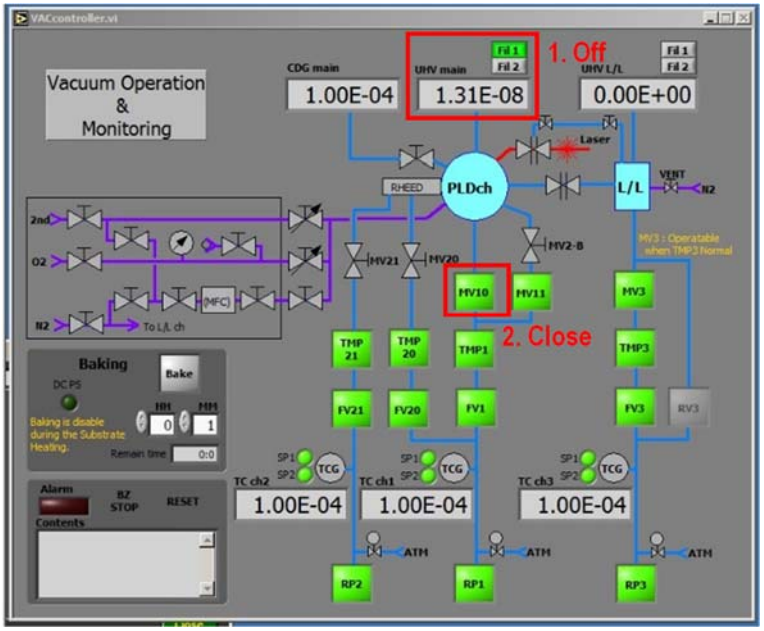

- 산소분압이 올라가다가 멈추면 MV11 를 조금씩 닫으면서 원하는 최종 산소 분압에 다다르도록 한다.

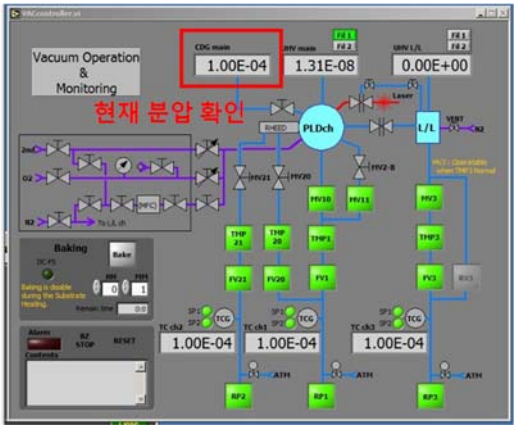

- 산소 분압이 맞춰지면, halogen lamp heater controller 의 “out put” 버튼을 눌러 전원을 켠 후에 현재시간을 필기한다.

- PLD system control panel 에서 ‘Start’ switch 를 켠 후에 3A 를 입력하고 5 분간 대기.

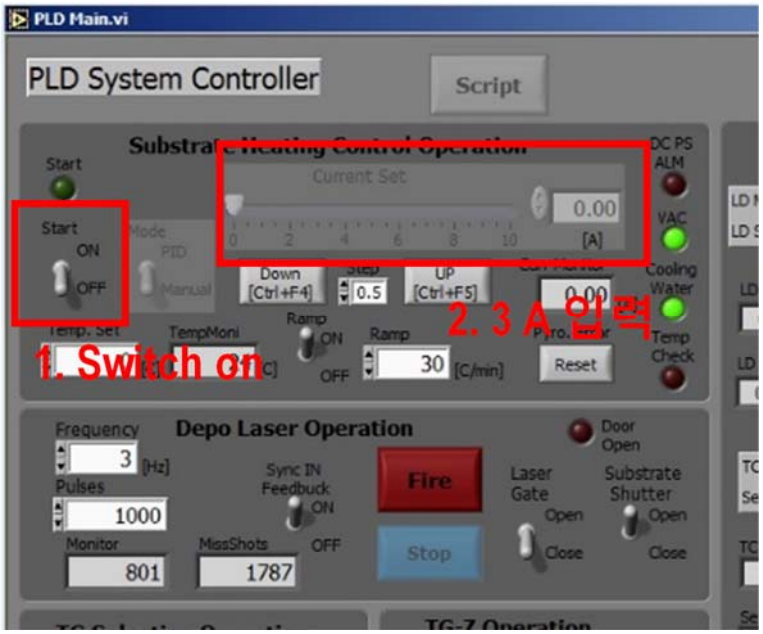

- 이후 0.5 A 씩 올리면서 각 단계에서 5 분간 대기한다 (4.5 A 까지). Lamp 상태를 기록하기 위해 각 단계에서 Heater 전압, 온도를 기록한다.
- 마지막 4.5 A 에서 5 분 대기가 끝났으면 기판 온도가 섭씨 278 도 이상이 되어 파이로미터로 기판온도를 측정할 수 있게 되었을 것이다. 이제 현재 시각을 기록한 후 PID 설정값을 입력하고 PLD system control panel 에서 'PID' switch 를 켠다. (PID 설정값은 기판의 온도가 아닌 heater 의 온도를 측정하기 때문에 경험적으로 PID 값을 알고 있어야 한다. 예를 들어 100 mTorr 산소 분압 조건에서 기판 온도를 섭씨 700 도로 하려고 한다면 PID 값을 510 으로 맞춰야 한다.)
- 온도가 다 올라갔으면 기판 shutter 를 닫는다.

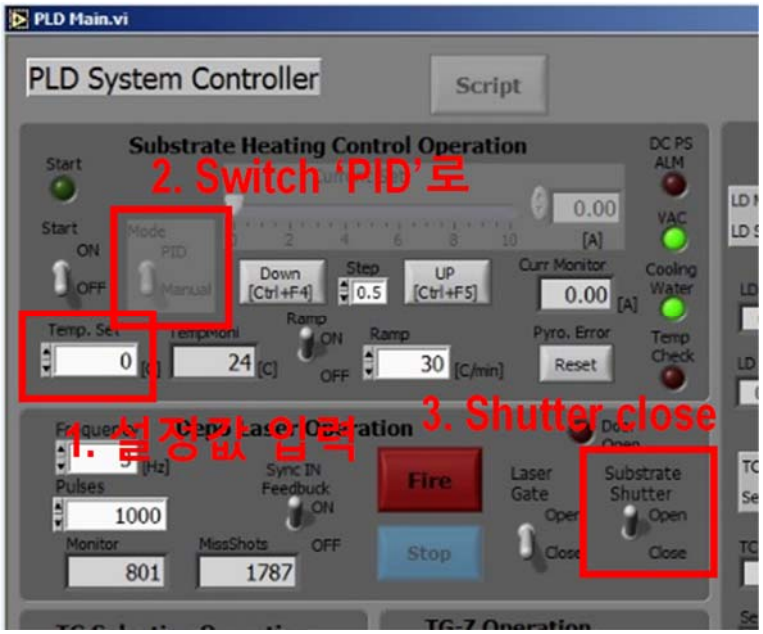

A.2.8 Target pre-ablation

- PLD system controller panel 에서 원하는 target 을 선택한다.
- Target rotation 을 켠다.
- Excimer laser 를 켠 후에 screen 에서 원하는 repeatition rate 과 pulse 숫자를 입력한 후 'Fire' 버튼을 눌러서 laser 를 발진 시킨다.
- Pre-ablation 이 진행되는 동안 산소 분압이 바뀌어서 흐트러진 RHEED 패턴을 다시 조절한다.
- Pre-ablation 이 끝나면 shutter 를 연다.

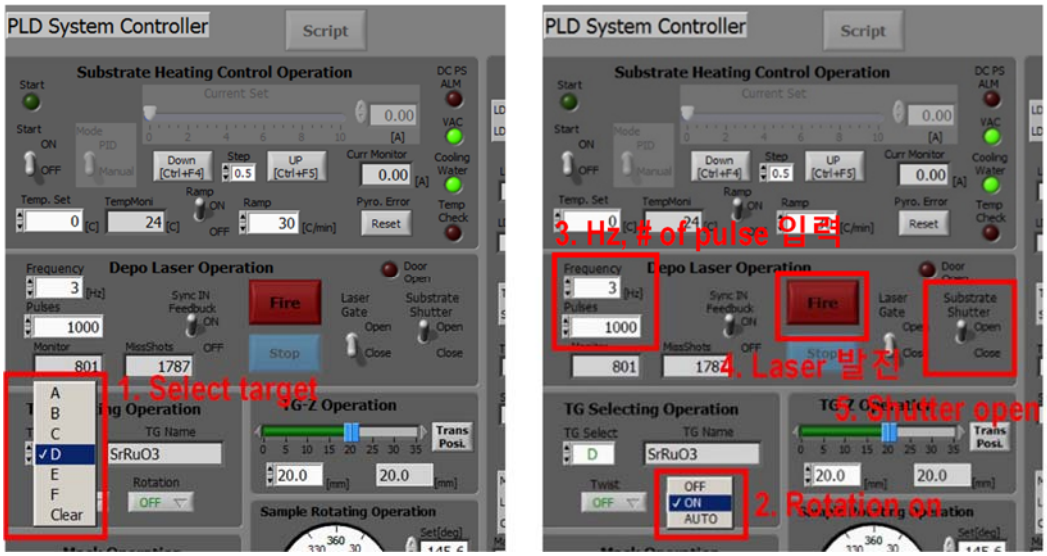

A.2.9 실제 박막 증착

- 온도, 분압 등을 확인 한 후에 다 맞춰져 있다면 현재 시각과 주요 parameter 들을 기록한다 (A.3. 로그북 예시 참조).
- kSA software 의 real-time monitoring 을 시작한 후 30 초간 대기하면서 intensity 가 일정하게 나오는지 확인한다.
- Excimer laser controller 에서 repetetition rate 을 맞춘 후 발진시킨다.
- RHEED oscillation 을 보면서 Growth rate 을 기록하고 원하는 박막 두께에 따라 pulse 횟수를 조절한다.
- Multi-layer 를 증착하고 싶다면 여러 target 에 대하여 A.2.7. - A.2.9.를 반복한다.

A.2.10 증착 끝내기

- RHEED 를 끈다. ‘HV’를 0 으로, 다음 ‘FIL’을 0 으로 내린 후, HV, FIL, FOC, X, Y, 순으로 끈다. 마지막으로 RHEED 파워를 끈다.

- 온도를 내린다. PLD system control panel 에서 ‘PID’ switch 를 끈 후 current 를 0 으로 낮춘다. Screen 의 ‘Start’ switch 를 끈 후 Lamp controller 의 파워를 끈다.

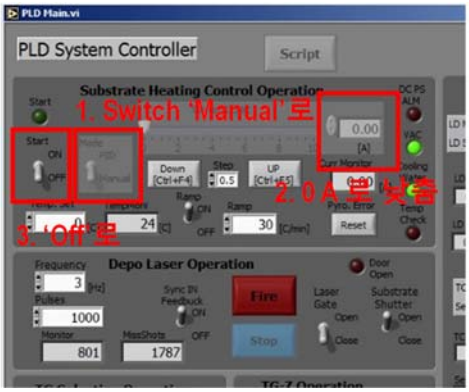

- 기판 온도가 섭씨 278 도 이하로 떨어지면 leak valve 를 완전히 잠근다. 이 때 너무 강한 힘을 가하면 leak valve 가 망가지므로 손가락 힘만을 이용해서 잠그도록 한다.
- MV11 를 열어서 Main chamber 의산소 분압을 1E-04 Torr 이하로 내린다.

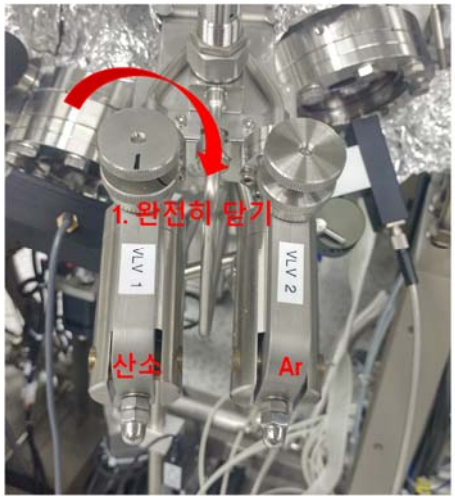

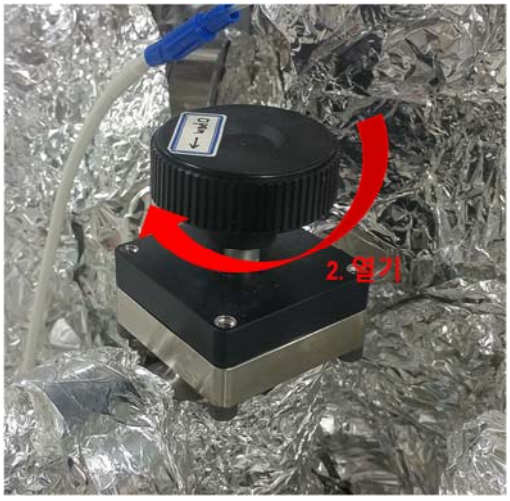

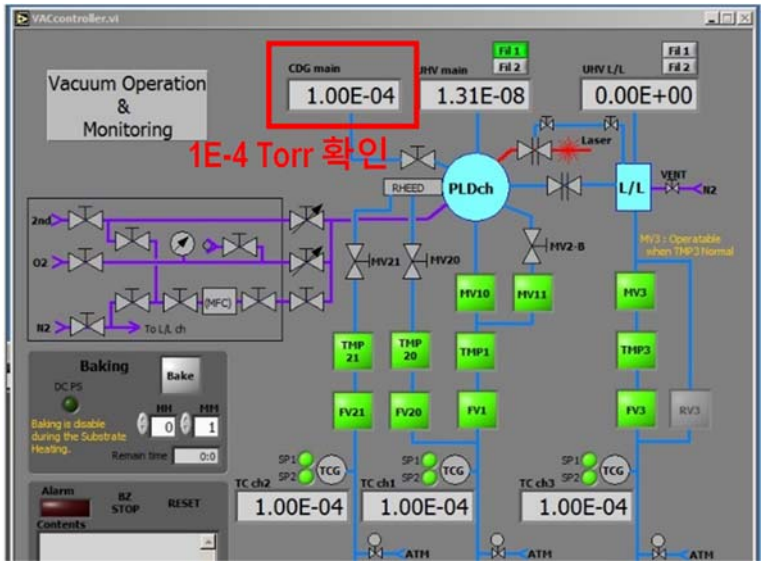

- MV10 을 열고 MV11 을 잠근다.
- Main chamber 의 ion gauge 를 켠다.

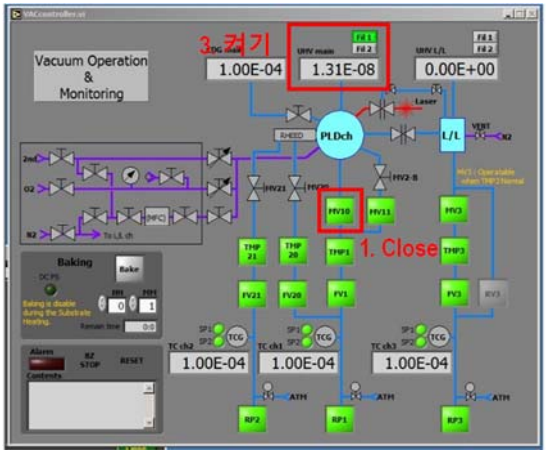

A.2.11 홀더를 L/L 으로 옮기기

- Lamp 위치를 'transfer'로 표시된 위치까지 내린 후 JOG controller 를 이용해 홀더를 빼내기 위한 위치로 옮긴다.
- 홀더의 'x', 'y'위치를 각각 10.5, 8 로 맞춘다.
- Main gate valve 를 연다.
- Transfer fork 를 홀더 앞까지 이동 시킨다.
- Halogen lamp 위치를 transfer 로 표시된 위치까지 이동
- 홀더 높이를 잘 조절하여 fork 를 홀더에 끼운 후에 높이를 더 내려서 Main chamber 의 홀더 stage 에서 홀더를 빼낸다.

- 홀더가 얹혀진 fork 를 L/L 까지 빼낸다.
- Gate valve 를 잠근다.
- A.2.3.1. 의 내용을 참조 L/L 을 venting 한 후에 샘플을 빼낸다.
- A.2.3.2. 의 내용을 참조하여 L/L 진공을 다시 잡는다.

A.3 로그북/연구노트 작성 예시

좋은 박막을 증착하는 것 만큼이나 증착 조건과 결과를 기록하는 것 또한 연구의 중요한 부분이다. 증착 과정과 증착 조건들을 세세하게 기록할 수 록, 예기치 않을 결과를 발견했을 때 그 원인을 밝히기 쉬워 지며, 증착 조건을 일정하게 유지하여 항상 좋은 품질의 박막을 만들 수 있게 된다. 아래에 $SrRuO_3/BaTiO_3/SrRuO_3$ heterostructure 를 증착하면서 기록한 연구노트 페이지를 예시로 남긴다.

날짜: 2017년 7월 20일

실험자: 신영재

실험장소/장비: Compact Laser-MBE (PASCAL Co., Ltd.)

실험 목적: SRO (20 nm)/BTO (3.5 u.c.)/SRO (20 nm) 박막을 제조하여 BTO 박막의 강유전 임계 두께를 시험한다.

(am 10:17) Start

Main chamber: 8.42E-09 Torr

L/L chamber: 1.58E-08 Torr

Main TMP: 0.5 A, TMP3: 7W, 29℃
TMP21: 8W, 30℃, TMP20: 8W, 30℃

Main chamber stage x, y :
for transferring holder → (10.5, 8)
for deposition → (11.8, 2.4)

(am 10:22) RHEED alignment
최대 intensity at x: 49, y: 19

(am 10:32) Oxygen injection at 8.56E-09 Torr

(am 10:43) Gate valve close at 8.28E-05 Torr

(am 10:47) Halogen heater on

3 A : 6.58 V, 34℃
3.5 A : 9.28 V, 62℃
4 A : 11.86 V, 103℃
4.5 A : 14.74V, 156/325℃

(am 11:08) PID on set 510

(pm 12:15) SRO pre-ablation

(pm 12:01) SRO start

(pm 01:21) SRO stop

산소 분압 조절 1) MV11을 이용 17 mTorr로, 2) Leak valve 를 이용하여 5 mTorr 까지 조절.

(pm 01:38) BTO pre-ablation

(pm 01:45) BTO start

(pm 01:49) BTO stop

산소 분압 조절 1) Leak valve 를 이용하여 17 mTorr 까지 조절. 2) MV11을 이용 100 mTorr로 조절

(pm 02:06) top SRO pre-ablation

(pm 02:13) top SRO start

(pm 02:52) top SRO stop

증착 마무리

실험 조건 상세:

Sample Code	COM17015	Purpose	BTO FE critical thickness	
Date	2017-02-28	Materials	SRO/BTO(3.5 u.c.)/SRO	
User(s)	신영재	Substrate	SrTiO3(001)-CrysTec	
Chamber	3号機(19-409)	Base Pressure (Torr)		1.20E-08
Pre-heating	Temperature(℃)	250	time	30'
	Note	w/ Pt paste ,in L/L		
Process 1	Target	**SRO**	Pre-ablation	10Hz, 5'
	Temperature(℃)	700	Time	1450''
	Heater Voltage	33.35 V	Heater Current	7.33 A
	Kind of gas	O_2	Gas Pressure	100 mTorr
Laser	Voltage	19.11 kV	Energy/Power	275 W
	Repetition Rate	3	Spot Size(mm^2)	1.5 × 2.5
RHEED	Voltage	18 kV	Current	2048 mA
	time/uc (s)	29''	# of UC	50
	Note	PID set 510		
Process 2	Target	**BTO**	Pre-ablation	10Hz, 5'
	Temperature(℃)	700	Time	76''
	Heater Voltage	31.58	Heater Current	7.03 A
	Kind of gas	O_2	Gas Pressure	5 mTorr
Laser	Voltage	17.3 kV	Energy/Power	260 W
	Repetition Rate	2	Spot Size(mm^2)	1.5 × 2.5
RHEED	Voltage	19.61 kV	Current	1950 mA
	time/uc (s)	19''	# of UC	4
	Note	PID set 530		
~~**Post-annealing**~~	~~Temperature(℃)~~	~~700~~	~~time~~	~~30'~~
	~~Kind of Gas~~	~~O_2~~	~~Gas Pressure~~	~~500 mTorr~~
	~~Note~~			
Process 3	Target	**SRO**	Pre-ablation	10Hz, 3'
	Temperature(℃)	700	Time	1465''
	Heater Voltage	33.01 V	Heater Current	7.28 A
	Kind of gas	O_2	Gas Pressure	100 mTorr
Laser	Voltage	18 kV	Energy/Power	275 W
	Repetition Rate	3	Spot Size	
RHEED	Voltage	19.94 kV	Current	2056 mA
	time/uc (s)	29.3''	# of UC	50
	Note	PID set 510		
Cooling	Start Temp.(℃)	700	Stop Temp.(℃)	RT (seting)
	Cooling time	20℃/min		
	Note			
Commnets	Attenuators for SRO (12), for STO (12)			

A.4 장비 진공 깨기/잡기

PLD 장비의 유지/보수에 관한 일이 있을 경우 많은 경우 장비 전체의 진공을 깨고 다시 잡는 과정을 거쳐야 한다. 이에 관한 매뉴얼을 간략하게 남긴다.

A.4.1 진공 깨기

- Pump 들로부터 Main chamber 와 L/L chamber 를 고립시켜야 한다. 이를 위해 Main chamber 와 L/L 의 ion gauge 들을 끄고 MV10, MV11, MV20, MV21, MV3, Capacitor gauge valve 를 잠근다.
- TMP1, TMP20, TMP21, TMP3 을 끈다. (진공을 깬 상태로 오래 PLD 를 나둬야 할 경우 Turbo pump 들이 모두 꺼진 후에 FV1, FV20, FV21, FV3 을 잠그고 RP1, RP2, RP3 을 모두 끈다.)
- Turbo pump 들이 꺼지는 동안, L/L chamber 의 door 클램프 나사를 열고 Main gate valve 를 연다.
- L/L 의 venting valve 를 열어서 Main chamber 와 L/L 의 진공을 깬다.
- Venting valve 를 잠근다.

A.4.2 진공 잡기

- RP3 를 켠 후, RV3 를 연다.
- RP1, RP2 를 켜고 FV1, FV20, FV21 을 연 후에 RP1 과 RP2 에 부착된 gauge 가 1E-4 Torr 를 가리킬 때까지 기다린다.
- TMP1, TMP20, TMP21 을 켠다.

- RP3 에 연결된 gauge 가 1E-04 Torr 가 될 때까지 기다린다.
- Main gate valve 를 잠근다.
- MV10, MV20, MV21 을 연다.
- Main chamber 의 ion gauge 를 켠다.
- RV3 를 닫고 FV3 를 연후 RP3 의 gauge 가 1E-04 Torr 가 될 때까지 기다린다.
- MV3 를 연다.

Publication list

(1) "Oxygen Partial Pressure during Pulsed Laser Deposition: Deterministic Role on Thermodynamic Stability of Atomic Termination Sequence at $SrRuO_3/BaTiO_3$ Interface"

Y. J. Shin, L. Wang, Y. Kim, H. –H. Nahm, D. Lee, J. R. Kim, S. M. Yang, J.-G. Yoon, J.-S. Chung, M. Kim, S. H. Chang, and T. W. Noh

ACS Applied Materials & Interfaces (2017, accepted)

(2) "Controlled manipulation of oxygen vacancy distribution with nanoscale flexoelectricity"

S. Das, B. Wang, Y. Cao, M. R. Cho, **Y. J. Shin,** S. M. Yang, L. Wang, M. Kim, S. V. Kalinin, L.-Q. Chen, and T. W. Noh

Nature Communications (2017, accepted)

(3) "Induced ferromagnetic moment at the interface between epitaxial $SrRuO_3$ film and Sr_2RuO_4 single crystal"

S. R. Lee, M. S. Anwar, **Y. J. Shin,** Min-Cheol Lee, Y. Sugimoto, M. Kunieda, S. Yonezawa, Y. Maeno, and T. W. Noh

Scientific reports (2017, under peer review)

(4) "Effect of internal field on the high resistance state retention of unipolar resistance switching in ferroelectric vanadium doped ZnO"

C. Wu, Y. Jia, **Y. J. Shin,** T. W. Noh, S. C. Chae, and C. Liu

Applied Physics Letters **110,** 143502 (2017)

(5) "Interface control of ferroelectricity in a $SrRuO_3/BaTiO_3/SrRuO_3$ capacitor and its critical thickness"

Y. J. Shin, Y. Kim, S.-J. Kang, H.-H. Nahm, P. Murugavel, J. R. Kim, M. R. Cho, L. Wang, S. M. Yang, J.-G. Yoon, J.-S. Chung, M. Kim, H. Zhou, S. H. Chang, and T. W. Noh

Advanced Materials **29,** 1602795 (2017)

(6) "Direct penetration of spin-triplet superconductivity into a ferromagnet in $Au/SrRuO_3/Sr_2RuO_4$ junctions"

M.S. Anwar, S.R. Lee, R. Ishiguro, Y. Sugimoto1, Y. Tano, S.J. Kang, **Y.J. Shin,** S. Yonezawa, D. Manske, H. Takayanagi, T.W. Noh, and Y. Maeno.

Nature Communications **7,** 13220 (2016)

(7) "Study of ferroelectric characteristics of diisopropylammonium bromide films"

C. Thirmal, P. P. Biswas, **Y. J. Shin,** T. W. Noh, N. V. Giridharan, A. Venimadhav, and P. Murugavel.

Journal of Applied Physics **120,** 124107 (2016)

(8) "Overcoming the Fundamental Barrier Thickness Limits of Ferroelectric Tunnel Junctions through $BaTiO_3/SrTiO_3$ Composite Barrier"

L. Wang, M. R. Cho, **Y. J. Shin,** J. R. Kim, S. Das, J.-G. Yoon, J.-S. Chung, and T. W. Noh.

Nano Letters **16,** 3911 (2016)

(9) "Suppression of creep-regime dynamics in epitaxial ferroelectric $BiFeO_3$ films"

Y. J. Shin, B. C. Jeon, S. M. Yang, I. Hwang, M. R. Cho, D. Sando, S. R. Lee, J. -G. Yoon, and T. W. Noh.

Scientific reports **5,** 10485 (2015)

(10) "Ferromagnetic $SrRuO_3$ thin-film deposition on a spin-triplet superconductor Sr2RuO4 with highly conducting interface"

M. S. Anwar, **Y. J. Shin,** S. R. Lee, S. J. Kang, Y. Sugimoto, S. Yonezawa, T. W. Noh, and Y. Maeno

Appl. Phys. Express **8,** 019202 (2015)

(11) "Flexoelectric Control of Defect Formation in Ferroelectric Epitaxial Thin Films"

D. Lee, B. C. Jeon, A. Yoon, Y. J. Shin, M. H. Lee, T. K. Song, S. D. Bu, M. Kim, J.-S. Chung, J.-G. Yoon, and T. W. Noh.

Advanced Materials **26,** 5005 (2014)

(12) "Active Control of Ferroelectric Switching Using Defect-Dipole Engineering"

D. Lee, B. C. Jeon, S.-H. Baek, S. M. Yang, Y. J. Shin, T. H. Kim, Y. S. Kim, J.-G. Yoon, C.-B. Eom, and T. W. Noh.

Advanced Materials **24,** 6490 (2012)

국문 초록

강유전체 물질이란 전기장 없이도 상시적 유전 분극을 가지는 물질 중에서도 외부 전기장에 의해 그 상시적 유전 분극의 방향을 바꿀 수 있는 물질을 일컫는 말이다. 이러한 전기적으로 조절 가능한 상시적 유전분극의 존재로 인해 강유전체 물질은 기능성 소자로서 주목 받아왔으며, 비휘발성 메모리 소자, 트랜지스터, 강유전체 터널 접합 등의 다양한 분야에서 응용되었다. 뿐만 아니라 강유전체 물질을 포함한 이종구조체에서는 강유전체의 상시적 유전 분극으로 인한 구조적, 전기적인 변화가 강유전체 물질의 인접 층에서 일어나게 된다. 이러한 효과로 인하여 근래에는 강유전체 물질을 이용하여 강자성, 초전도성 등의 물성을 전기적으로 조절하려는 연구가 진행되었으며, 차세대 다기능성 다기능성 소자로 가는 가능성을 제시하고 있다. 이러한 연유로 강유전체 물질은 비단 응집 물질 물리 분야뿐 아니라 재료 과학 분야에서도 다양하게 연구되고 있다.

최근 급속도로 진행되고 있는 산화물 기반 소자의 소형화로 인하여 계면 효과가 강유전체 물질에 미치는 영향을 이해하는 것이 중요해지고 있다. 강유전체 박막의 두께가 수 원자 층 수준으로 얇아지게 되면, 덩치 시료나 두꺼운 박막 시료에서는 크게 나타나지 않았던 계면 효과가 강유전체 이종구조체의 다양한 물성에 영향을 끼치게 된다. 예를 들어 금속/강유전체 계면의 화학적 결합의 종류나 세기에 따라 강유전체 유전 분극의 안전성이 크게 달라질 수 있다는 보고가 강유전체 $BaTiO_3$, $PbTiO_3$ 박막에 대한 연구에서 보고되었다. 또한 상유전체/강유전체 계면에서의 강한 극성 불연속성 (polar

dicontinity)으로 말미암아 flux-type 구역 구조나 vortex 구역 구조와 같은 일반적으로 강유전체 박막에서 발현되지 않는 구역 구조가 나타나기도 한다. 특히, 계면 형태학이나 원자구조와 같은 계면의 구조적인 영향들은 강유전체 유전 분극 성질에 크게 영향을 끼친다. 본 논문에서는 이러한 계면 구조가 강유전체 에피 박막의 물성에 미치는 영향에 대한 새로운 실험 연구 결과들을 발표한다.

유전 분극 – 외부 전기장 이력 곡선은 (*P-E* hysteresis loops) 다른 물질과 강유전체 물질을 구분하는 가장 큰 특징 중 하나이다. 강유전체 에피 박막에서 이력 곡선은 외부 전기장 하의 미시적인 구역 구조의 움직임에 의해서 결정되는데, 이 때 통계학 적으로 구역 구조의 움직임은 불균일한 매질 속에서 외력에 크기에 대해 비선형적인 전파 속도를 갖는 탄성체의 움직으로 묘사될 수 있다. 이러한 비선형성에 의해 강유전체 에피 박막을 이용한 소자들은 외부 교류 전기장의 주파수 (*f*)에 대하여 강한 의존성을 보이게 된다. 본 논문에서는 강유전체 $BiFeO_3$를 이용한 축전 소자를 만듦에 있어서 전극 층을 이루는 물질이 강유전체 구역구조가 느끼는 불균일성에 크게 영향을 준다는 것을 밝혔다. 특히, 특정 물질을 전극 물질로 선택한 경우 강유전체/전극 계면의 불균질 성이 크게 줄어들면서 주파수 의존성이 없는 이상적인 강유전체 소자를 구현할 수 있었다.

본 논문에서는 펄스 레이저 증착법 (PLD)을 이용하여 강유전체 이종 구조체인 $SrRuO_3/BaTiO_3/SrRuO_3$ (SRO/BTO/SRO)를 제조할 때, 산소 분압이 계면 원자 구조에 미치는 강한 영향에 대하여 연구하였다. 두께 수 나노미터에서도 강유전성을 잃지 않는 강유전체 초박막 소자를 구현하기

위해서는 원자 수준으로 강유전체 층의 표면/계면 구조를 조절하는 것이 필수적이다. 그러나 펄스 레이저 증착법으로 길러진 박막에서 표면 원자 구조를 결정하는 기작에 대해서는 연구가 부족하였다. 이러한 연유로 펄스 레이져 증착법을 이용한 원자 층 수준의 표면/계면 구조 조절은 기초적인 수준에 머물러 왔다. 본 논문에서는 산소 분압 조절을 통하여 SRO/BTO 계면의 원자 구조를 $SrO\text{-}TiO_2$ 혹은 $BaO\text{-}RuO_2$로 선택적으로 증착하는 방법을 제시하였다. 상대적으로 고 산소 분압 (150 mTorr)에서 길러진 BTO 박막에 대하여 SRO/BTO 계면이 불균일하게 분포한 $SrO\text{-}TiO_2$ 계면 구조와 $BaO\text{-}RuO_2$ 계면 구조를 모두 갖는 반면에, 저 산소 분압 (5 mTorr)에서 길러진 BTO에 대해서는 SRO/BTO 계면이 균일한 $SrO\text{-}TiO_2$ 구조만을 갖는 것을 확인하였다. 추가적인 실험에서는 이러한 계면 구조의 변화가 전체 기체 분압, 혹은 증착 속도 등의 관계없이 산소 분압에 의해서만 결정된다는 것을 확인하였다. 이것은 관측된 계면 구조 변화가 펄스 레이저 증착법에서 중요시 되던 플라즈마 동역학에 의해서가 아니라 다소 주목 받지 못했던 열역학적인 표면/계면 에너지 차이에 의해서 유도된다는 것을 말해준다.

마지막으로, 본 논문에서는 산소 분압 조절에 의해서 유도된 계면 원자 구조의 변화가 BTO 초박막의 강유전성에 미치는 강한 영향에 대하여 밝혔다. 변전힘 현미경 (PFM)을 이용하여 SRO/BTO/SRO 축전 소자의 유전 분극 반전을 연구한 결과 두께 수 원자 층의 BTO 박막에 대하여 불균일한 계면 구조를 갖는 SRO/BTO/SRO 축전 소자는 국소적으로 단안정한 유전 분극 보여 강유전성이 크게 훼손 되어 있음을 발견하였다. 반면에 균일한 $SrO\text{-}TiO_2$ 계면 구조를 갖는 SRO/BTO/SRO 축전 소자의 경우 모든 측정 영역에서 안정한

유전 분극 반전이 관측 되었다. 이러한 안정한 강유전성은 두께 3.5 원자 층 (1.2 나노미터)의 BTO 박막에서 까지 발견되었다.

우리는 본 논문에서 이뤄진 계면 구조와 강유전성의 연관성에 대한 집중적인 연구가 강유전체 초박막 응용에 있어서 계면 효과가 갖는 결정적인 역할에 대한 이해의 폭을 넓히는데 공헌하리라 생각한다.

주요어: 강유전체 박막, 계면 공학, 산화물 이종구조체, 펄스 레이저 증착법

학번: 2011-20407